



Aeroacoustic wind tunnel tests

Lylloff, Oliver Ackermann

Link to article, DOI:

<https://doi.org/10.11581/dtu:00000102>

Publication date:

2020

Document Version

Publisher's PDF, also known as Version of record

[Link back to DTU Orbit](#)

Citation (APA):

Lylloff, O. A. (2020). *Aeroacoustic wind tunnel tests*. DTU Wind Energy. DTU Wind Energy PhD
<https://doi.org/10.11581/dtu:00000102>

General rights

Copyright and moral rights for the publications made accessible in the public portal are retained by the authors and/or other copyright owners and it is a condition of accessing publications that users recognise and abide by the legal requirements associated with these rights.

- Users may download and print one copy of any publication from the public portal for the purpose of private study or research.
- You may not further distribute the material or use it for any profit-making activity or commercial gain
- You may freely distribute the URL identifying the publication in the public portal

If you believe that this document breaches copyright please contact us providing details, and we will remove access to the work immediately and investigate your claim.

Aeroacoustic wind tunnel tests

Oliver Ackermann Lylloff

Roskilde, 2020



Technical University of Denmark

DTU Wind Energy

Frederiksborgvej 399

4000 Roskilde, Denmark

www.vindenergi.dtu.dk

This thesis was prepared at the department of Wind Energy and submitted to the Technical University of Denmark (DTU) in partial fulfillment of the requirements for the degree of Doctor of Philosophy (Ph.D.) in Wind Energy. The work was conducted between February 2017 and November 2020.

Title: Aeroacoustic wind tunnel tests

Supervisors:

Senior Scientist **Andreas Fischer** (asfi@dtu.dk)

Senior Scientist **Christian Bak** (chba@dtu.dk)

DTU Wind Energy,

Technical University of Denmark (DTU),

Frederiksborgvej 399,

4000 Roskilde, Denmark.

Associate Professor **Efren Fernandez-Grande** (efg@elektro.dtu.dk)

DTU Electrical Engineering,

Technical University of Denmark (DTU),

Ørstedes Plads,

2800 Kongens Lyngby, Denmark.

Roskilde, November 18, 2020

Oliver Ackermann Lylloff

Abstract

The global demand for renewable energy sources has led to an increase in development and installation of wind turbines. However, noise regulations on wind turbines near populated areas can restrict the installation of new wind turbines and limit the potential energy production. The main noise from wind turbines is aerodynamic and arises from turbulence caused by the air flow around the wind turbine blades in motion. The aerodynamic noise increases with the size of the wind turbine, and with a demand for more productive, and thus larger wind turbines, there is an increased interest in quantifying the aerodynamic noise from wind turbine blades. This thesis investigates experimental methods for estimating the noise of wind turbine blades in a newly-established wind tunnel – the Poul la Cour Tunnel (PLCT).

This study has three focus areas; the acoustic design of the wind tunnel airline, the measurement conditions and sound propagation properties in the anechoic, Kevlar-walled test section, and the quantification of trailing edge noise of wind turbine blade sections.

The attenuation of background noise (from the wind tunnel airline) is a crucial part of successful acoustic measurements. To investigate this, the wind tunnel design was described and an experimental in-situ method proposed for determining transmission losses of the acoustically treated wind tunnel airline components. The results were compared to a numerical study that was conducted prior to construction, showing good agreement and thereby validating the general acoustic design. In the test section, acoustic measurements are made with a microphone array situated behind a tensioned Kevlar wall inside an anechoic room. The acoustic losses due to sound propagation through the Kevlar fabric was examined both with and without flow in several measurement setups. A comparison of methods and results was discussed and found to agree with the existing literature on the topic. Additionally, methods for quantifying absolute noise levels of an airfoil was examined. Several of these were applied to measurements of a NACA63018 airfoil at flow speeds ranging from about 30 m/s to 70 m/s (Reynolds numbers 2 mio. to 4 mio.) and corrections due to Kevlar losses were applied. The results were compared to a trailing edge noise model, finding good agreement. This dissertation describes the relevant contributions of the PhD study and places it in the context of current aeroacoustic wind tunnel research.

Resumé

Den globale efterspørgsel på vedvarende energikilder har ført til øget udvikling og rejsning af vindmøller. Den potentielle energiproduktion kan dog være begrænset på grund af støjkrav nær beboede områder. Den dominerende støj fra vindmøller er aerodynamisk og skyldes turbulens fra vindens strømning omkring vindmøllevingerne i bevægelse. Den aerodynamiske støj øges med størrelsen af vindmøllen og med en efterspørgsel på større produktion, og dermed større vindmøller, er der en øget interesse i at kvantificere the aerodynamiske støj fra vindmøllevinger. Denne afhandling undersøger eksperimentelle metoder til bestemmelse af støj fra vindmøllevinger i en nyligt indviet vindtunnel - Poul la Cour Tunnel (PLCT).

Dette studie har tre fokusområder; det akustiske design af vindtunnelens kanal, måle- og lydudbredelsesegenskaberne i det lyddøde, Kevlar-væggede test område, og kvantificering af bagkantsstøj fra sektioner af vindmøllevinger.

Dæmpningen af baggrundsstøjen (fra blæseren i vindtunnelen) er en afgørende del af succesfulde akustiske målinger. For at undersøge dette blev designet af vindtunnelen beskrevet og en eksperimentel in-situ metode foreslået til bestemmelse af transmissionstab af de akustisk dæmpede elementer i vindtunnelens kanal. Resultaterne var i overensstemmelse med et numerisk studie, der blev udført før opførelsen, og dermed blev det akustiske design valideret. Testområdet er placeret i et lyddødt rum og her udføres akustiske målinger med et mikrofon-array placeret bag en opspændt væg af Kevlar. Lydudbredelsen gennem Kevlar-væggen giver et transmissionstab som blev undersøgt både med og uden strømning i adskillige forsøg. Metoder og resultater blev diskuteret og der blev fundet overensstemmelse med eksisterende litteratur på området. Metoder til kvantificering af absolutte støjniveauer fra et vingeprofil blev også undersøgt. Adskillige af disse metoder blev benyttet på målinger af et NACA63018 vingeprofil ved strømningshastigheder fra 30 m/s til 70 m/s (Reynoldstal 2 mio. til 4 mio.) og korrektioner for Kevlar-tab blev anvendt. Resultaterne blev sammenlignet med en model for bagkantsstøj og der blev fundet god overensstemmelse. Denne afhandling beskriver de relevante bidrag af Ph.d studiet og placerer dem i konteksten af den nuværende aeroakustiske vindtunnelforskning.

Acknowledgements

When I first sat foot in the Poul la Cour Tunnel it was a construction site, an empty concrete duct. Now, three years later, there is a test section in an anechoic room, a microphone array, a fan, two kevlar walls, and much more. And for the past year, we have successfully conducted multiple measurement campaigns on airfoils. This thesis is a product of that process, but also a product of the invaluable contributions and support from colleagues and friends.

First, I would like to thank my supervisors Andreas Fischer, Christian Bak, and Efren Fernandez-Grande. Their guidance and collective knowledge has been outstanding and an invaluable part of this PhD study.

I would like to thank the dedicated group of people working in the Poul la Cour Tunnel: Jimmie Beckerlee, Sigurd Ildvedsen, Anders Smærup Olsen and Robert Mikkelsen, for their help setting up experiments and for always keeping a positive attitude.

To to my research group (AER), Naja Møller for taking care of the administrative hassles, and my office friends: Sinem Özçakmak, Mads Holst Aagaard Madsen, and Christian Grinderslev for fun chats and keeping the spirit high.

From the technical staff at DTU Wind Energy (TEM): Per Hansen, Karen Enevoldsen, and Steen Arne Sørensen for help and support with measurement equipment and IT.

Thanks to the "House of Acoustics" at DTU Elektro, with special thanks to Henrik Hvidberg, Andrew King, Cheol-Ho Jeong, Franz Heuchel, and Diego Caviedes Nozal for help setting up experiments and good discussions.

From Virginia Tech, William Devenport, Aurelien Borgoltz, and Matt Kuester for their hospitality and work on cross-validation of facilities.

I would also like to thank Jørgen Hald and Finn Jacobsen, for inspiring me to pursue a career in acoustics.

And to my family, for their unconditional support. To my mother, for nurturing my curiosity growing up, to my daughters Norma and Helga, for reminding me about the joys in life, and most importantly Stella, for encouraging me to pursue a PhD degree, for supporting me along the way, and for being my best friend and life partner.

Contents

Abstract	iii
Resumé	v
Acknowledgements	vii
Contents	viii
1 Introduction	1
2 Wind tunnel design	5
2.1 Prior work	5
2.2 The Poul la Cour Tunnel	7
2.3 Summary of Paper A	7
2.4 Background noise	8
2.5 Conclusion	10
3 Beamforming	13
3.1 Notation and theory	13
3.2 Source power integration	15
3.3 Beamforming in flow	15
3.4 Deconvolution and inverse methods	16
3.5 Summary of Paper B	19
4 Test section design	21
4.1 Open jet and closed test section	21
4.2 Hybrid test section	22
4.3 PLCT test section	24
4.4 Kevlar losses	32
4.5 Summary of Paper C	34
4.6 Conclusion	37
5 Noise quantification of a NACA63018 airfoil	39
5.1 Benchmark validation	39

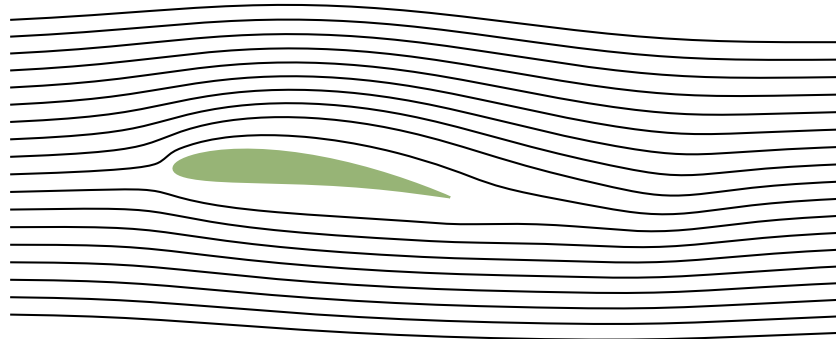
5.2	NACA 63018 validation	41
5.3	Results	54
5.4	Conclusion	65
6	Concluding remarks	67
	Paper A	71
	Paper B	95
	Paper C	115
	Bibliography	135

Chapter 1

Introduction

Wind is a natural energy source. It has been an integral part of the Earth's atmosphere for billions of years and has been used by living creatures for eons. And our own species are known to have used wind energy for thousands of years. And why not? It is an inexhaustible source of energy, right there above our heads. In many countries, windmills are a historic symbol of a time before electricity, where the hard labour of grinding corn was "outsourced" to the wind. From the very first human flight, at the very beginning of the previous century, and through an industrial (aerospace) revolution, to now, our ability to harvest energy from the wind, has become one of the most promising solutions to a global environmental crisis. The idea is simple: Convert kinetic energy from wind into mechanical energy. This has been done by windmills for hundreds (arguably even thousands) of years, but modern day wind turbines convert the mechanical energy into electricity. Despite the similarity with windmills, a lot of effort has gone into the development of modern wind turbines from its onset in the 1970s. The blades, for instance, have undergone a large change since the traditional windmills and is inspired by the shape airplane wings, therefore often called airfoils. The physical principle behind the airfoil's ability to fly can be described by Bernoulli's principle, which dates back to 1700s. Consider a uniform flow moving from left to right, illustrated by streamlines in the picture below. When the flow meets the airfoil, streamlines must pass either over or under the airfoil. The airfoil shape increases the flow velocity above the airfoil and decreases it below. Bernoulli's principle states that this results in a pressure difference with low pressure above and high pressure below, giving a net lift, illustrated by a compression of streamlines above the airfoil. This 300 year old principle is used to design modern day blades for wind turbines.

In the design stage, wind turbine blades undergo a wealth of tests and simulations to ensure that the specific design is efficient. A wind tunnel is used to test and validate the aerodynamic properties of the design by applying a controlled airflow to a scale model of the blade. This can be done through



the principle of Reynolds number scaling, where the Reynolds number is the ratio of inertial (convective) and viscous forces, referenced to a characteristic length scale, typically the chord length of the blade. If the Reynolds number, referenced to the scale model chord length, match the Reynolds number of the full-scale blade, the flow properties are roughly similar, and the blade design can be validated in realistic flow conditions. The current trend in wind turbine development is towards larger wind turbines, with larger rotor diameters, longer blades, and thus higher tip speeds (from 2006 to 2015, the average rotor diameter of newly installed wind turbines in Europe increased from about 70 m to 100 m [1]). The tip speed of a wind turbine with a rotor diameter of 100 m, rotating at, e.g., 15 min^{-1} , has a tip speed of approximately 80 m/s. At this speed, a turbulent boundary layer develops on the airfoil and a dominant noise source arises as flow passes over the trailing edge. This is the most important of several airfoil self-noise mechanisms, described by Brooks et al. [2], in the far-field noise spectrum of wind turbines. It is also the main cause of noise regulations on onshore wind turbines.

The overall objective of this thesis is to estimate experimentally, the trailing edge noise of an airfoil in a wind tunnel. This is done towards the end of this thesis. However, to achieve this goal, an acoustic wind tunnel must be used. The Poul la Cour Tunnel at DTU Wind Energy was built to facilitate accurate noise measurements. The design includes several acoustic absorbers in the wind tunnel airline and a test section with Kevlar walls inside a large anechoic room. The wind tunnel design is the topic of Chapter 2, where the acoustic design is also validated. Outside the test section, a large number of microphones are placed to measure noise from the airfoil while filtering out background noise, using a technique called beamforming. This is the topic of Chapter 3. The test section walls are made of Kevlar, which is known for having a high tensile strength and low acoustic impedance, effectively making it permeable to sound. In Chapter 4, the test section design is discussed, and the acoustic properties of Kevlar are investigated. Finally, methods for quan-

tification of trailing edge noise are described in Chapter 5 and experimental results from the Poul la Cour Tunnel on a NACA63018 airfoil are presented and compared to a trailing edge noise model. A summary of contributions are given in Chapter 6 with suggestions for future work.

The aim of this PhD study is to investigate the acoustic measurement conditions in a wind tunnel and examine techniques to quantify noise from wind turbine blade sections. The research has been centered around the Poul la Cour Tunnel with the following objectives:

- Validate the acoustic design of the Poul la Cour Tunnel through simulations and measurements.
- Implement and develop signal processing techniques for microphone array measurements specific to the conditions in the Poul la Cour Tunnel. Taking into account the background noise, losses introduced by the Kevlar walls and corrections related to the aerodynamic properties of the flow.
- Setup and validate aeroacoustic measurements.
- Implement and develop methods for quantification of trailing edge noise.

This PhD thesis is comprised of a synopsis and three contributed papers following the DTU guidelines for a paper-based format. The contributed papers are included as appendices and summaries are given in the text where each paper fits in the main storyline.

Paper A O. Lylloff, A. Fischer, E. Fernandez-Grande, C. Bak, "Acoustic Design Validation of an Anechoic Wind Tunnel". Submitted for publication.

Paper B O. Lylloff, E. Fernandez-Grande, "Noise Quantification with Beamforming Deconvolution: Effects of Regularization and Boundary Conditions". 7th. Berlin Beamforming Conference 2018 (BeBeC), Berlin, Germany, 05/03/2018.

Paper C O. Lylloff, A. Fischer, E. Fernandez-Grande, C. Bak, "Acoustic Level Corrections for a Kevlar-walled Wind Tunnel". Submitted for publication.

Chapter 2

Wind tunnel design

When solid objects are subject to high flow speeds, such as cars, airplanes, high-speed trains, or rotating wind turbines blades, audible noise arises and can cause annoyance for people in its vicinity. A wind tunnel can be used to understand how that noise is generated. By producing a well-defined and controllable air flow, that the object is placed in, the flow-related noise can be measured with acoustic equipment. While some objects are tested in full-scale (typical in the automotive industry), scale models are often used for wind tunnel tests. The wind tunnel design should ideally reflect the type of research that is expected to be carried out. This is of course not always possible as research is constantly evolving or older wind tunnels are re-purposed for different kinds of research. However, some considerations are needed to make the initial design. Some crucial aspects are the type(s) of flow that is wanted in the test section. This means that design criteria such as range of flow speeds, turbulence intensities and physical dimensions of the objects to be studied, must be determined prior to the design process can begin. A wide range of wind tunnels exist from the large wind tunnels used by the automotive and aerospace industries to the smaller, typically university-owned, wind tunnels used for research. One clear distinction between different wind tunnel designs is whether acoustic research is expected to be conducted or not. This is seen in the interest in attenuating background noise. In the following, focus will be on wind tunnels used for acoustic research.

2.1 Prior work

For a historical context, an overview of acoustic wind tunnel research is found by a search query on Web of Science:

wind tunnel* AND (noise* OR sound* OR acoustic*),

and plotting the number of publications per year in Fig. 2.1. The earliest mentions on acoustics and wind tunnels occur in the early and mid 1950s with Beranek et al. [3]. Incidentally, their focus was not on acoustic wind tunnel

testing but noise reduction due to complaints by neighbors. Several meeting abstracts in the late 1960s and early 1970s have mentions on acoustics, but the first publications that shows up in the search query is McCanless and Boone in 1974 and Schutzenhofer and Howard in 1975 [4, 5], that studied noise reductions in transonic flow wind tunnels. Later in the 1970s, measurement techniques for background noise suppression were improved with the acoustic mirror [6]. Amiet made groundbreaking work on trailing edge noise [7] and derived a correction for sound refraction by an open jet shear layer [8] and at the same time, Howe published seminal work on the theory of trailing edge noise [9]. Soderman and Hoglund gave a comprehensive overview of background noise attenuation mechanisms in a wind tunnel [10]. In late 1980s Brooks et al. studied trailing edge noise and began to use microphone arrays for their research, which led to the so-called BPM model [2].

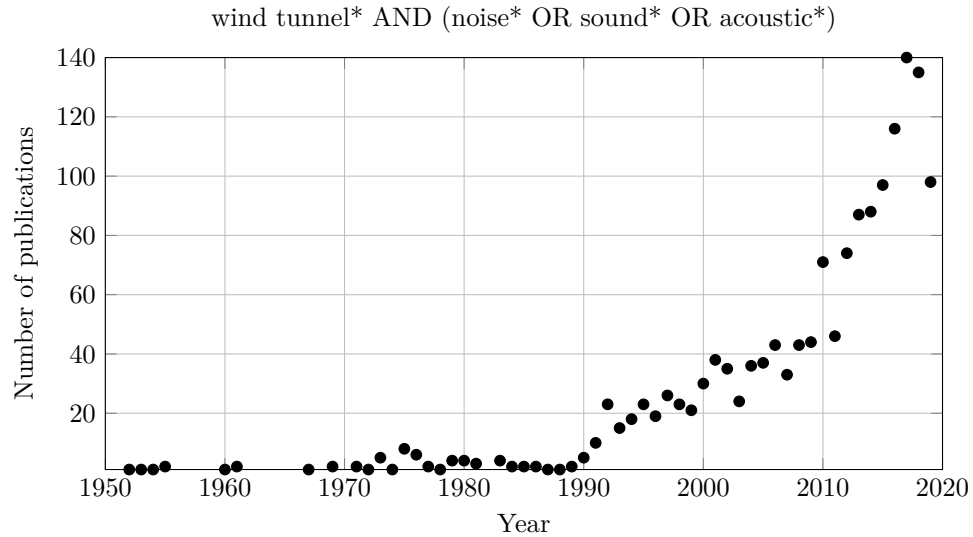


Figure 2.1: Number of publications (incl. meeting abstracts) per year matching search query (retrieved October 12, 2020 from Web of Science).

Many aeroacoustic wind tunnels are solely for commercial testing, e.g., in the aerospace and automotive industry. While some of these tunnels are described in the literature, the amount of research that is shared publicly is scarce. Brouwer gave an introduction to anechoic wind tunnels and design considerations in [11], and later, Duell et al. gave a review of the state of aeroacoustic wind tunnels [12] with updates in [13]. The PhD thesis by Mathew is notable by its thorough review of the design of an anechoic wind tunnel [14]. More recently, Gomes et al. gave an extensive review of the design considerations for an aeroacoustic wind tunnel with examples from the DNW-NWB low speed wind tunnel [15]. A newly-constructed wind tunnel, dedicated to wind energy research, is the Poul la Cour Tunnel. In the following sections,

the focus will be on the design and properties of this tunnel.

2.2 The Poul la Cour Tunnel

This thesis is largely based on the Poul la Cour Tunnel¹. In the following, a description of the tunnel and the elements that comprises it is given. Further descriptions can be found in [16]. An overview of PLCT is shown in Figure 2.5 (on page 12). It was designed for aerodynamic and acoustic tests of wind turbine blade sections. The initial specifications are given in Table 2.1. These

Maximum Reynolds number per meter	$7 \cdot 10^6$
Maximum flow speed	105 m/s
Design flow speed for acoustic measurements	60 m/s
Test section: Width	3 m
Test section: Height	2 m
Test section: Length	9 m
Maximum turbulence intensity	0.1 %
Background noise at 60m/s with Kevlar walls 2m from airfoil	$\leq 70\text{dB}$

Table 2.1: PLCT design specifications. From [16].

specifications were found through dialogue with stakeholders and centered around the need for higher flow speeds due to the increase in wind turbine rotor size. The specifications for flow speed combined with the test section size and maximum turbulence intensity led to a design where the air flow is driven by a 2.4 MW fan and a contraction with an area ratio of 9 : 1.

In Paper A, the acoustic design of PLCT is presented and an experimental methods for its validation is proposed. The reader is invited to read Paper A at this point, or continue with a summary of it below.

2.3 Summary of Paper A

Acoustic Design Validation of an Anechoic Wind Tunnel.

Paper A is concerned with attenuation of background noise in the Poul la Cour Tunnel. The design of the tunnel was conducted using numerical tools to estimate the required amount of acoustic absorption to meet the design objectives. Absorbing material was placed in guide vanes, around the fan and in the diffuser downstream of the test section. In Ref. [16], a finite element simulation of the wind tunnel was presented, and the transmission losses of the acoustically treated elements was estimated. Paper A proposes an experimental in-situ method for estimating the transmission loss and compare that to the numerical study in [16]. The method is based on measuring impulse

¹Named after the Danish wind entrepreneur Poul la Cour (1846 – 1908).

responses with microphones placed at the inlet and outlet of an acoustic absorber. The results show, that the methodology can validate the numerical results within 3 dB in the frequency range of 1000 Hz to 5000 Hz. The method was particularly useful at the guide vanes and diffuser, however, at the fan, the method of impulse responses did not hold and an alternative method was used, based on a sound power reference source. The results for the fan silencer indicate, that the sound power reference method is applicable, but the signal-to-noise ratio should be improved and measurements redone, before drawing further conclusions.

2.4 Background noise

The main goal of the acoustic design, described above, is to have a low background noise level to facilitate precise acoustic measurements. The autospectrum of the background noise in PLCT is shown for 9 different flow speeds in Fig. 2.2. The measurements were taken at a distance of 2.8 m from the test

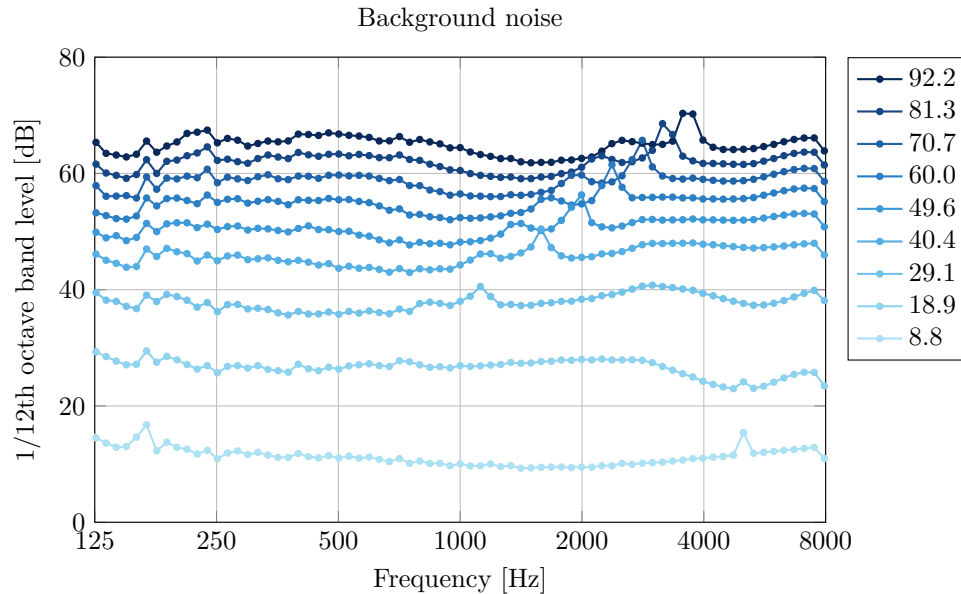


Figure 2.2: Background noise spectrum for 9 flow speeds [m/s]. Measured at a distance of 2.8 m from the test section center line behind a Kevlar wall.

section center line, behind a Kevlar wall. The background noise spectrum is comprised of background noise from the wind tunnel airline and turbulent boundary layer (TBL) noise from floor, ceiling and Kevlar walls. In the background noise spectrum, there are several noticeable features. First, the spectrum is quite constant in level as function of frequency. The fan noise is known to be significant at low frequencies, and a level increase could be ex-

pected at frequencies below 1000 Hz. However, the lack of such an increase is a testament to the effectiveness of the acoustic absorbers in the tunnel, that was specifically tuned to attenuate noise below 1000 Hz. Second, a noticeable peak is seen in the spectrum from 1000 Hz to 4000 Hz as function of flow speed. This peak is an aeolean tone due to a pitot tube situated at the contraction. The physical generation of the tone is due to vortex shedding in the wake of a cylinder, and the frequency of the tone can be calculated from [17]

$$St = 0.198 \cdot (1 - (19.7/Re)) \quad (2.1)$$

$$f_{\text{aeolean}} = St \cdot U_0/L, \quad (2.2)$$

where $St = fL/U_0$ is the Strouhal number, $Re = U_0L/\nu$ the Reynolds number, U_0 the free stream velocity, L the characteristic length, and ν the kinematic viscosity. Setting $L = 5$ mm, the diameter of the pitot tube, the Strouhal number is $St = 0.198$, and the aeolean tone is expected at frequencies shown in Table 2.2.

f [Hz]	348	750	1153	1601	1965	2377	2799	3219	3650
U_0 [m/s]	8.8	18.9	29.1	40.5	49.6	60.0	70.7	81.3	92.2

Table 2.2: Aeolean tones in the background noise spectrum due to a pitot tube in the contraction.

In Fig. 2.3 the Strouhal number spectrum is shown. The peak from the aeolean tube aligns perfectly at $St = 0.198$. In the figure below, a Mach number scaling is applied to the Strouhal number spectrum, with the correction $SPL_{1/12} + 55 \cdot \log_{10}(0.1/Ma)$ to frequencies in the range 500 Hz–6 kHz, where $Ma = U_0/c$, and c is the speed of sound. It is seen, that the curves collapse, therefore, the background noise level is found to scale with $Ma^{5.5}$, which agrees well with literature (an exponent between 5 and 7 is found in [12]). Additionally, the vortex shedding from a cylinder has dipole-like source characteristics, that scales with Ma^6 [18, 19], which is also observed in Fig. 2.3.

The overall sound pressure level (OASPL) can be used to characterize acoustic wind tunnels [12, 20]. In fact, a general performance metric (for open jet wind tunnels) is to evaluate the A-weighted OASPL as function of flow speed, corrected for measurement distance and nozzle exit area [21]. Using this metric to compare open-jet facilities with a Kevlar-walled wind tunnel, however, is difficult, since the measured background noise in the Kevlar-walled wind tunnel is comprised of background noise from the airline and TBL noise, while the background noise in an open jet facility comes from the jet nozzle. In Fig. 2.4 the OASPL of the PLCT background noise is shown. The design criteria related to background noise was ≤ 70 dB at $U_0 = 60$ m/s (indicated with a star in Fig. 2.4). It is seen, that the background noise is about 5 dB higher than that of the design specification.

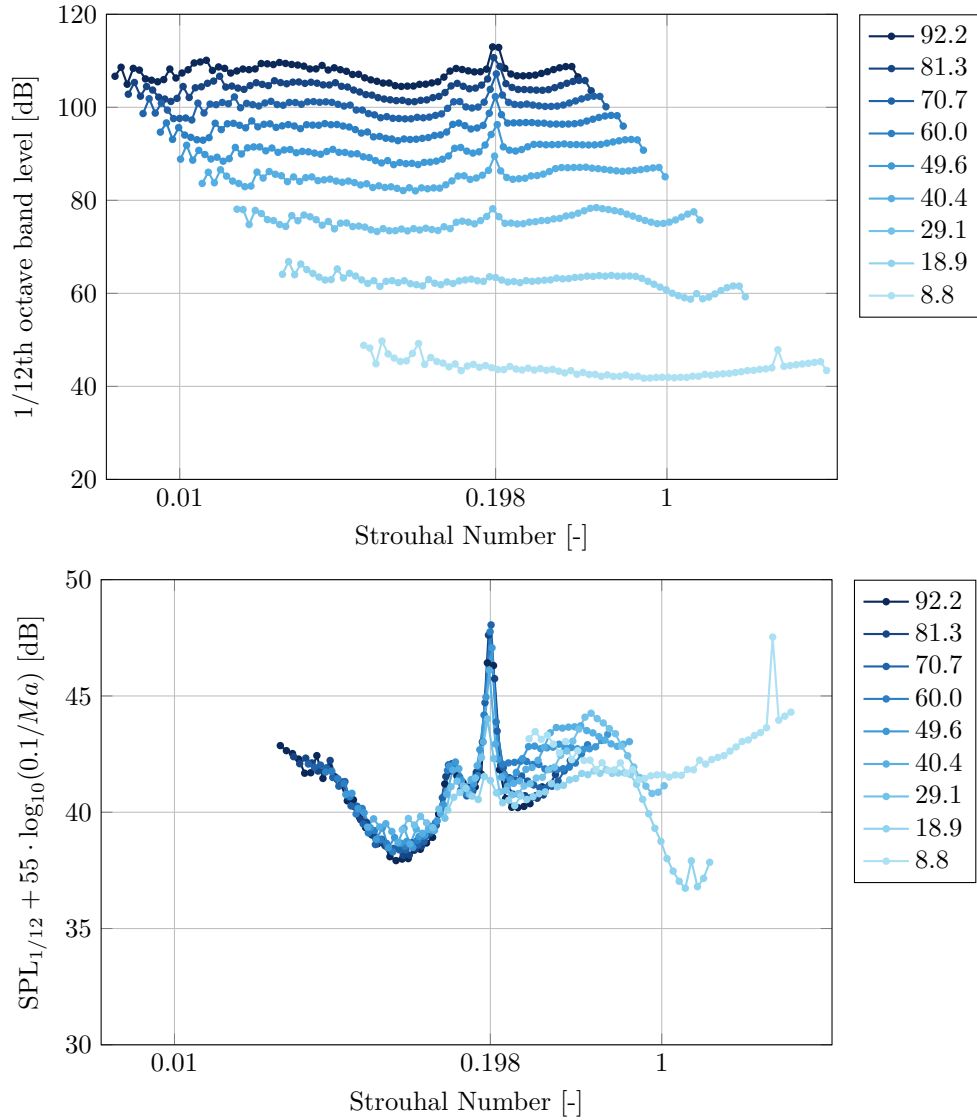


Figure 2.3: Strouhal number spectrum (top figure) and to that added Mach number scaling $Ma^{5.5}$ (bottom figure) for 9 flow speeds [m/s].

2.5 Conclusion

The first objective of this thesis was about acoustic validation of PLCT. In this chapter, an overview of (acoustic) wind tunnel design was given, and the Poul la Cour Tunnel was introduced. The acoustic design objectives of PLCT was validated in Paper A, using a methodology based on impulse responses. The transmission loss of the acoustically treated guide vanes and diffuser, was shown to be comparable to a numerical study conducted prior to construction

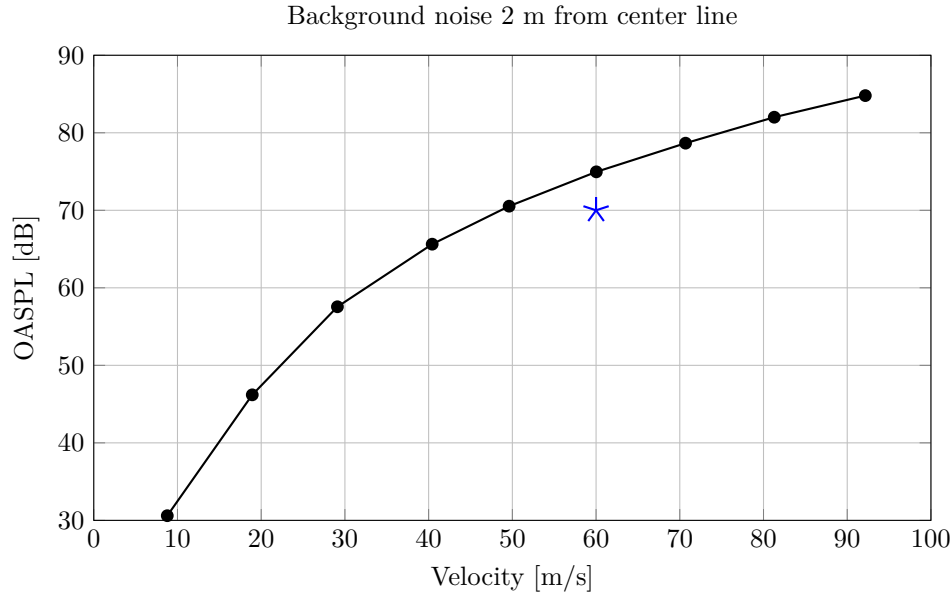


Figure 2.4: Overall background noise (200 Hz–7 kHz) measured behind a Kevlar wall as function of flow speed. The background noise is comprised of wind tunnel noise (from the wind tunnel airline) and turbulent boundary layer noise on the Kevlar wall. Star indicates the acoustic design criteria of PLCT.

of the wind tunnel. The proposed method was not applicable to estimation of the transmission loss of the fan silencer, and an alternative approach was suggested. The results were not conclusive due to lack of signal-to-noise ratio. Follow-up studies should consider a more powerful loudspeaker. The background noise in PLCT was shown to scale with $Ma^{5.5}$, which is within the typically reported range of powers 5-7.

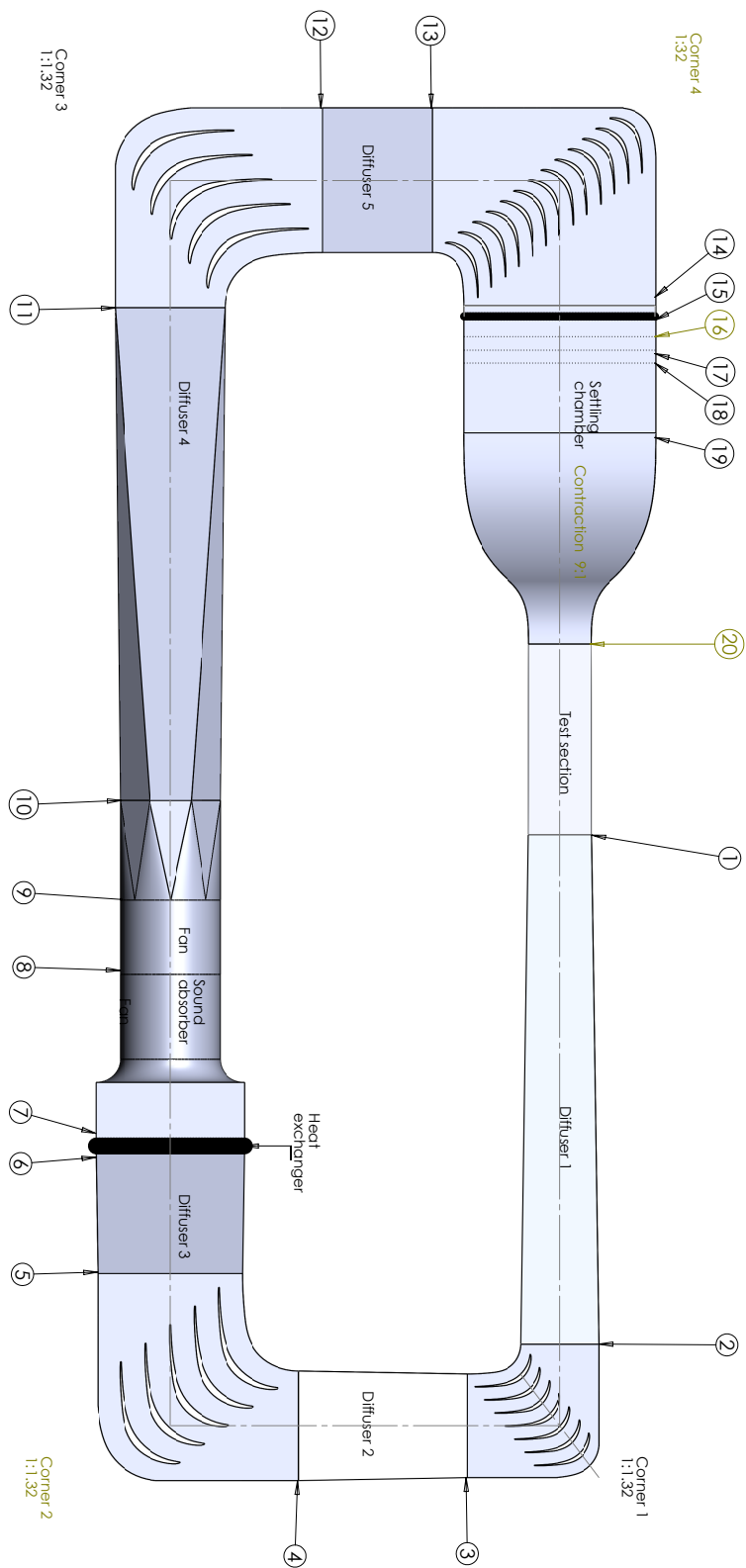


Figure 2.5: PLCT. Flow direction is clock-wise. Image credit: Jens Österlund.

Chapter 3

Beamforming

This chapter addresses the general theory and background of acoustic beamforming, source power integration (SPI), deconvolution, and inverse methods for estimation of aeroacoustic sources from microphone array measurements. The literature in acoustic beamforming for source localization and identification is vast. The reader is referred to [22, 23] for a historical context, [24] for recent review of applications of beamforming, as well as to classical textbooks, such as [25, 26].

3.1 Notation and theory

Consider the sound pressure measured at a microphone array with M microphones due to a single point source at \mathbf{r}_s producing stationary noise. The notation and orientation is shown in Figure 3.1. The sound pressure in the frequency domain at the m 'th microphone, \mathbf{r}_m , is modelled as

$$p(\mathbf{r}_m) = \frac{q(\mathbf{r}_s)}{|\mathbf{r}_s - \mathbf{r}_m|} e^{-jk|\mathbf{r}_s - \mathbf{r}_m|}, \quad (3.1)$$

where $q(\mathbf{r}_s) = j\omega\rho Q_s$ is the source strength, $j = \sqrt{-1}$, Q_s is the volume velocity, $\omega = 2\pi f$ is the angular frequency, f is the frequency, and k is the wavenumber [27]. The Green's function in free-field between the source point and the m 'th microphone is [27]

$$G(\mathbf{r}_s, \mathbf{r}_m) = \frac{e^{-jk|\mathbf{r}_s - \mathbf{r}_m|}}{|\mathbf{r}_s - \mathbf{r}_m|}. \quad (3.2)$$

Arranging contributions from each microphone in a vector \mathbf{p} , and defining a vector, \mathbf{g} , of Green's functions for each microphone to \mathbf{r}_s ,

$$\mathbf{p} = \begin{bmatrix} p(\mathbf{r}_1) \\ p(\mathbf{r}_2) \\ \vdots \\ p(\mathbf{r}_M) \end{bmatrix}, \quad \mathbf{g} = \begin{bmatrix} G(\mathbf{r}_s, \mathbf{r}_1) \\ G(\mathbf{r}_s, \mathbf{r}_2) \\ \vdots \\ G(\mathbf{r}_s, \mathbf{r}_M) \end{bmatrix} \quad (3.3)$$

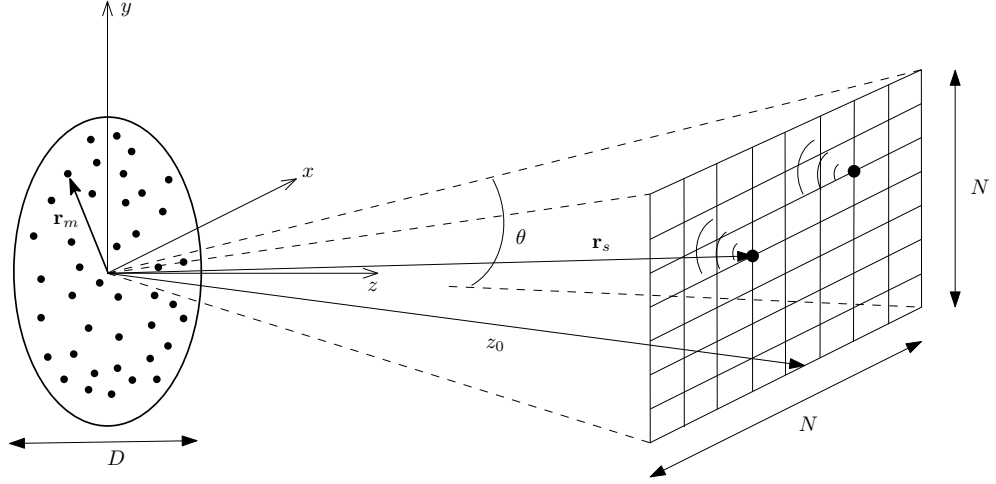


Figure 3.1: Microphone array notation. Microphones are at positions \mathbf{r}_m , unknown source positions \mathbf{r}_s in an $N \times N$ source grid, placed at a distance of z_0 from the microphone array.

the model (3.1) can be written $\mathbf{p} = q(\mathbf{r}_s) \cdot \mathbf{g}$ for all M microphones. Rearranging to get $q(\mathbf{r}_s) = \mathbf{g}^H \mathbf{p} / M$, where the strength is normalized by dividing by M . Using this model, the source strength can be estimated from a measurement \mathbf{p} that is propagated to the source position via \mathbf{g} . In quadratic form, the mean-squared source strength $|q(\mathbf{r}_s)|^2 = \mathbf{g} \mathbf{p} \mathbf{p}^H \mathbf{g}^H / M^2$, where $\mathbf{p} \mathbf{p}^H$ is the cross-spectral matrix, \mathbf{C} , which is typically obtained as an ensemble average because the noise is stationary. This gives the central result,

$$|q(\mathbf{r}_s)|^2 = \frac{1}{M^2} \mathbf{g} \mathbf{C} \mathbf{g}^H, \quad (3.4)$$

which is the single point frequency-domain delay-and-sum (DAS) beamforming result [28]. However, in practise, the position of the source is unknown, and the mean-squared beamforming output (denoted b from now) is then due to an assumed point source at focus point \mathbf{r}_d ,

$$b(\mathbf{r}_d) = \mathbf{v}(\mathbf{r}_d)^H \mathbf{C} \mathbf{v}(\mathbf{r}_d), \quad (3.5)$$

where $\mathbf{v}(\mathbf{r}_d)$ is a steering vector (a normalized Green's function) between microphone m and focus point \mathbf{r}_d , typically with elements [28],

$$v_m(\mathbf{r}_d) = \frac{1}{M} \frac{|\mathbf{r}_d - \mathbf{r}_m|}{|\mathbf{r}_d - \mathbf{r}_0|} e^{-jk|\mathbf{r}_d - \mathbf{r}_m|}, \quad (3.6)$$

where \mathbf{r}_0 is the center of the microphone array to normalize the response of the beamforming output. Alternative formulations of the steering vectors can be found in [29].

While beamforming is a simple and effective method for localizing sources, its resolution is frequency-dependent. This means that the ability to distinguish sources in the beamforming map becomes more difficult at lower frequencies, where the size of the array aperture becomes comparable or smaller than the acoustic wavelength. The Rayleigh-criterion can be used to estimate the spatial resolution, [30, 28],

$$R = 1.22 \frac{Lc}{Df}, \quad (3.7)$$

assuming that source and microphone array is on-axis, L is the measurement distance, c the speed of sound, and f the frequency.

The beamforming response to a single, unit strength point source at \mathbf{r}_s is often referred to as the point spread function (PSF),

$$\text{PSF}(\mathbf{r}_d, \mathbf{r}_s) = \mathbf{v}(\mathbf{r}_d)^H \left(\mathbf{v}(\mathbf{r}_s) \mathbf{v}(\mathbf{r}_s)^H \right) \mathbf{v}(\mathbf{r}_d), \quad (3.8)$$

and is used for characterising the fidelity of the microphone array, to acquire absolute noise levels from beamforming and in deconvolution algorithms.

3.2 Source power integration

In special cases, the DAS beamforming output leads to correct source powers. That is, if sources are well separated, have uniform directivity, are monopoles, and the coherence is unity between microphones, then, the peak value in the beamforming output represents the true source power [31]. However, in most practical circumstances, this is not the case. The Source Power Integration technique was introduced in [32], and further developed in [33] and [31]. To obtain a power estimate, P , the idea is to sum the beamforming output within a defined region and normalize it to the sum of the same region in the point spread function,

$$P = \frac{\sum_{d \in S} b(\mathbf{r}_d)}{\sum_{d \in S} \text{PSF}(\mathbf{r}_d, \mathbf{r}_s)}, \quad (3.9)$$

where S is the set of indices in the source grid that is within the region of integration.

3.3 Beamforming in flow

The free-field Green's function defined above does not hold in a wind tunnel, since the sound propagation from source to receiver is affected by a flow field. In the simplest case, the convected Green's function can incorporate a uniform flow field, but more complicated situations can also be encountered. For instance, in the case where the microphone array is placed outside the flow, a

velocity discontinuity (or steep gradient) is located at an unknown position between the source and measurement plane, and refraction of sound occurs. A well-known correction for this is due to Amiet [8], that modeled the sound field as if the microphone array was also in the uniform flow and moves with the source. Additionally, Amiet provided an amplitude correction that accounts for the transmission loss at the boundary.

Diagonal removal and denoising

Aeroacoustic measurements can easily be contaminated by turbulent boundary layer (TBL) noise, which will produce incoherent noise signals in a microphone array. The DAS beamforming method typically uses an ensemble-averaged CSM, where incoherent noise signals will be concentrated along the matrix diagonal, if enough averages are used. The off-diagonal terms of the CSM contain cross-spectra, and phase-information, between microphones, which is used to localise sources with DAS beamforming. Therefore, the diagonal of the CSM can essentially be removed without harming the beamforming output – a method known as Diagonal Removal (DR). However, in some cases, DR can cause overestimated power levels [34]. This can introduce issues, namely if the CSM is no longer positive semidefinite, meaning that negative eigenvalues can be present, causing non-physical, negative power estimates. A common solution is to only sum positive power estimates or use a threshold to determine which power estimates can be included in the source integration [31].

Recently, several new denoising approaches have emerged, all with the same objective of keeping the CSM positive semidefinite while removing the contributions in the diagonal. A review of methods were given in [35, 36].

Yet another approach is to make a background noise measurement (without the test object) and subtract it from the actual measurement of the test object. Assuming that the flow conditions and noise has not changed, only the noise from the test object remains. A more advanced approach is the subspace-based background noise subtraction [37].

3.4 Deconvolution and inverse methods

Continuing from the notation above, the linear system of equations to be solved is due to M microphones and $N \times N$ source strengths,

$$\mathbf{p} = \mathbf{G}\mathbf{q}, \quad (3.10)$$

Here, the model matrix \mathbf{G} can be either the Green's function, mapping source pressures \mathbf{p} to source strengths \mathbf{q} , or it can be a matrix collected of point-spread functions (PSF), where \mathbf{p} is the beamforming map described as a blurring of \mathbf{q} . In the former case, $\mathbf{p} \in \mathbb{C}^M$, $\mathbf{q} \in \mathbb{C}^{N^2}$, and $\mathbf{G} \in \mathbb{C}^{M \times N^2}$, and \mathbb{C} is the set of

complex numbers. In the latter case, $\mathbf{p} \in \mathbb{R}^{N^2}$, $\mathbf{q} \in \mathbb{R}^{N^2}$, and $\mathbf{G} \in \mathbb{R}^{N^2 \times N^2}$, and \mathbb{R} is the set of real numbers. This is a fundamental difference in the choice of model that is reflected in the solution strategy. If the beamforming map is used as input, \mathbf{G} is assembled column-wise by point-spread functions for each grid point. In certain cases, the PSF can be assumed to be shift-invariant, that is, represented by a single PSF at the center of the source plane, instead of a full matrix, and the problem in Eq. (3.10) can then be written as a convolution product. Therefore the solution for \mathbf{q} is known as deconvolution. This is illustrated in Fig. 3.2. In some cases, the quadratic form of Eq. (3.10) is more

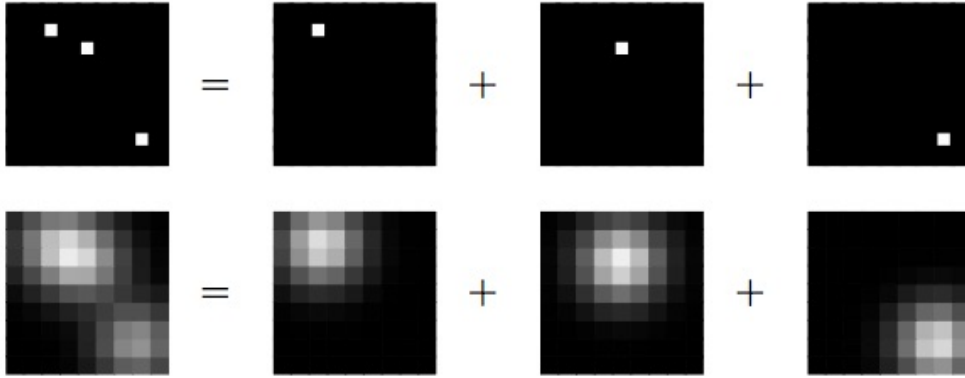


Figure 3.2: Deconvolution illustration. Top left is the true source distribution \mathbf{q} , and bottom left is the blurred measurement \mathbf{p} . If the maps can be assumed to be a superposition of uncorrelated point sources and the PSF is the same for all grid points (shift-invariant), the solution strategy is called deconvolution.

convenient to work with,

$$\mathbf{S}_p = \mathbf{G}\mathbf{S}_q\mathbf{G}^H, \quad (3.11)$$

where $\mathbf{S}_p = \mathbf{p}\mathbf{p}^H$ (the CSM) and $\mathbf{S}_q = \mathbf{q}\mathbf{q}^H$. This model is typically used in "inverse methods", as opposed to deconvolution methods. This classification term is quite broad since it holds a wide range of different solution strategies.

These two models form the basis of the majority of efforts to solve the inverse problem, that is, find \mathbf{q} or \mathbf{S}_q given \mathbf{p} or \mathbf{S}_p and \mathbf{G} . It is not straightforward to estimate the true source distribution, as the problem is ill-posed. This means, that a solution might not exist and sensitivity to measurement noise can corrupt the solution [38]. A unified formalism for acoustic reconstruction problems is presented by Leclère et al. [39]. In the following, an overview of methods found in the aeroacoustic literature will be covered. The overview is not meant to be exhaustive, but it focuses on established methods that can be used for estimating trailing edge noise in a wind tunnel.

Before the introduction of deconvolution in aeroacoustic, directional microphone arrays have been in use since the mid 1970s, with correlation techniques and traditional beamforming [40, 41, 42]. Techniques were developed

through the mid 1990s, such as array geometry optimization [43] and adaptive methods for sidelobe suppression [44, 45]. The first deconvolution method was adapted from Astrophysics and introduced by Dougherty: CLEAN [46, 45], extended by Sijtsma with CLEAN-PSF and CLEAN-SC [47]. CLEAN-SC is based on the beamforming map (typically classified as a deconvolution method, although it is strictly not) and works by iteratively locating the strongest source and storing that in a clean map. Then the source and its coherent sources, i.e., sidelobes or mirror sources are removed (or parts thereof through the loop-gain parameter ϕ) and the process is repeated until no significant sources are present. The loop-gain parameter $0 \leq \phi \leq 1$ control how much is removed from the dirty map at each iterations. A low value removes a small amount, and can require more iterations to converge. A stopping criterion can be made by storing values of the strongest source at each iteration. Since these are expected to decrease for each iteration, a stopping criterion is set when the value of the strongest source is larger than a previous one.

Another commonly used method is DAMAS, which is a Gauss-Seidel type algorithm [48, chap. 11] with a non-negativity constraint [49, 50]. The PSF at each grid point in the source plane is used in the algorithm, and therefore neither strictly a deconvolution algorithm. The extensions in [51], however, use a shift-invariant assumption, to reduce the computational load. DAMAS is not guaranteed to converge [52], which makes it difficult to determine a stopping criterion, and an arbitrary high number of iterations (e.g. 100,500,1000,5000) is typically reported in the literature.

In general, the solution to the inverse problem is typically formulated as an optimization problem, from Eq. (3.10),

$$\begin{aligned} & \underset{\mathbf{q}}{\text{minimize}} \quad \|\mathbf{G}\mathbf{q} - \mathbf{p}\|_2^2 \\ & \text{subject to} \quad \mathbf{q} \geq 0 \end{aligned} \tag{3.12}$$

This is the Non-negative least squares (NNLS) solution and it is used in both deconvolution and inverse methods. In [52] this formulation, originally from [53], is used as a deconvolution method which was extended in [54]. The quadratic form of Eq. (3.12) is,

$$\begin{aligned} & \underset{\mathbf{S}_q}{\text{minimize}} \quad \|\mathbf{G}\mathbf{S}_q\mathbf{G}^H - \mathbf{S}_p\|_n^2 \\ & \text{subject to} \quad \mathbf{S}_q \succcurlyeq 0, \end{aligned} \tag{3.13}$$

where $\mathbf{S}_q \succcurlyeq 0$ means \mathbf{S}_q must be positive semidefinite. Equation (3.13) is also called Covariance Matrix Fitting (CMF) [55] or spectral estimation method (SEM) [56].

The methods described above, CLEAN-SC, DAMAS, CMF, and NNLS, are commonly applied in aeroacoustic research. Benefits and drawback are very case dependent. A recent, and more extensive, review of methods and applications were given in [24]. Experimental and simulated benchmark test

cases have been developed by the aeroacoustic community and comparisons of implementations from different research institutions were given in [57, 58]. In the simulated test case [58], a similar performance of methods was reported, with some variations in the CLEAN-SC results. The variation was attributed to individual implementations and different stopping criteria. A similar conclusion was given for DAMAS in the experimental test case [57] and NNLS showed similar results as DAMAS. In [59], reconstruction of incoherent and coherent monopole sources was investigated experimentally with DAS, CLEAN-SC, DAMAS, and CMF. It was found that DAMAS and CMF yield the most reliable results. The same conclusion was found in [60], where a Monte-Carlo method is applied to a wide range of simulated cases. However, it is noted that DAMAS and CMF underestimate secondary sources [60]. In all of the above-mentioned studies, it is highlighted, that DAMAS and CMF is very time-consuming relative to DAS and CLEAN-SC.

One of the benchmark test cases was used in Paper B to investigate a deconvolution algorithm for the solution of Eq. (3.12). The paper was written early in the PhD study, where experimental results were not yet available. The reader is invited to read Paper B at this point, or continue with a summary of it below.

3.5 Summary of Paper B

Noise Quantification With Beamforming Deconvolution: Effects Of Regularization And Boundary Conditions.

Paper B investigates the effects of boundary conditions and regularization of a deconvolution method. A simulated benchmark test case of four monopoles is used, which was also described in [58]. It is hypothesized, that the boundary conditions of the beamforming map has an effect on the reconstructed solution. Several boundary conditions are applied, and a deconvolution algorithm (NNLS) is used to estimate the individual spectra of the four monopole via source integration. The results show, that only one of the boundary conditions has an effect on the reconstruction, and that it is possible, with that, to reduce the frequency limit below Rayleigh's criterion. In the second part of the paper, two types of regularization are compared, and the results show that both can reconstruct the correct levels if the right regularization parameter can be estimated. In a parametric study, it is found that the regularization parameter depends on the frequency and signal-to-noise ratio. From this it can be concluded, that one optimal regularization parameter cannot be found, and a compromise must be made on a subjective basis.

Chapter 4

Test section design

The test section accounts for only a small fraction of the overall volume of the wind tunnel but houses most of the necessary equipment for conducting aeroacoustic research. In fact, the preparations and efforts that have gone into the design of the wind tunnel airline is done in order to enable the best possible measurement conditions in the test section. This chapter addresses the measurement conditions in an acoustic test section, it describes the two common test section designs: the open jet and closed test sections, and relates them to the newer hybrid test section with Kevlar walls. A description of the PLCT (hybrid) test section follows, and finally an examination of the Kevlar wall properties is given along with a summary of Paper C, that is concerned with acoustic level corrections due to the Kevlar walls.

4.1 Open jet and closed test section

Two test section designs are used extensively: the open jet and closed test section [34]. In the closed test section, microphones are typically mounted in the tunnel walls, exposed to strong pressure fluctuations due to boundary layer turbulence, which can degrade the quality of measurements. The open jet test section allows for microphones to be placed outside the flow in a quiescent medium, but this can potentially reduce the resolution, due to the increased measurement distance. Additionally, the open jet exhibit a different aerodynamic behavior. In both cases, the sound propagation path must pass either a free shear layer (open jet) or turbulent boundary layer (closed test section), that can cause attenuation and phase-change of sound waves. An extensive review of the comparability of acoustic measurements in open jet and closed test section designs is given in the PhD thesis by Kröber [61] and also by Oerlemans [62].

The closed test section is basically an aerodynamic wind tunnel that has been fitted with acoustic equipment. It can be either in-flow microphones or flush-mounted microphone (arrays) [34]. The benefit of this type of test sec-

tion is mainly aerodynamic; the flow is kept undisturbed and uniform, and from a practical point of view, simultaneous measurements of aerodynamics and acoustics are possible. The main drawback is, from an acoustic perspective, the placement of microphones close to the flow, causing high background noise levels, and microphone self-noise due large pressure fluctuations in the turbulent boundary layer on the wall, with a low signal to noise ratio to follow (for airfoil noise at least). Efforts to reduce the microphone self-noise includes recessing microphones [63], and covering microphones with fabrics [64]. Other drawbacks are duct modes, and reflections from walls, both which can interfere with acoustic measurements, as either an increase in background noise level at specific frequencies (proportional to the standing waves) or as coherent mirror sources [34].

The open jet test section, is generally believed to be more suitable for acoustic measurements, as microphones are placed out-of-flow, typically surrounded by an anechoic room. The main issue for acoustic measurements in the open jet test section is the sound propagation through a mean velocity gradient layer (shear layer), that increases in thickness with distance to the nozzle. A reflection and transmission will occur at the interface, typically modelled with infinitely thin thickness, and also a refraction. These effects can be corrected for and a widely used model is due to Amiet [8]. Additionally, if the thickness of the shear layer approaches the acoustic wave length, turbulent scattering occurs and cause decorrelation between microphones in a microphone array. The scattering of sound waves obscure the phase information it carries, which lead to problems for methods that rely on phase-matching, e.g., beamforming, and manifests in a spectral broadening in the measured spectra. Implementing a flow model can help relieve the issue [65, 66, 67, 68].

This short comparison of the benefits and drawbacks of traditional acoustic test section designs, leads to the introduction of the hybrid test section. The idea introduced by Jaeger et al. [64], where flush-mounted microphones were covered with Kevlar, a strong fabric with low acoustic impedance, was taken to full-scale test section walls in [69, 70], as a hybrid between the open jet and closed test sections. In the following chapter, an overview of hybrid test sections is given, and the test section of the Poul la Cour tunnel introduced.

4.2 Hybrid test section

The hybrid test section is contrived from the idea of combining the benefits of the open jet and closed test sections. Several acoustic wind tunnel facilities around the world have either adopted the hybrid design by retrofitted existing tunnels or constructed new tunnels with the hybrid design in mind. At least seven¹ different wind tunnels have published studies on their design

¹Eight if counting Paper A included in this thesis

or described the use of a hybrid test section. These are summarized in Table 4.1. Even more wind tunnels have begun work on hybrid test sections, but descriptions have not been published in the scientific literature yet. The facil-

Facility	Reference
Virginia Tech (Stability Wind Tunnel)	[70]
JAXA	[71]
Florida State	[72]
Beihang University (D5)	[73]
NASA Langly (QFF)	[74]
University of Bristol	[75]
Brandenburg University of Technology	[76]

Table 4.1: Wind tunnels described in the literature with Kevlar test sections.

ities stated in Table 4.1 have either a closed test section design with side walls replaced by tensioned Kevlar or an open jet test section with Kevlar panels situated between test section and acoustic equipment. The Kevlar walls experience a deflection despite it being tensioned. Therefore, to achieve comparable aerodynamic properties as a closed test section, corrections for the deflection must be applied. The PhD Thesis by Brown investigates aerodynamic corrections for Kevlar walls [77].

Since the first studies on Kevlar by Jaeger et al., a topic of investigation has been quantifying the acoustic losses in the propagation path from the test object to acoustic measurement equipment. The impedance of Kevlar, although low, cause a transmission loss. Additionally, as a turbulent boundary layer is developed over the tensioned Kevlar wall, acoustic flow losses have also been investigated. Jaeger et al. measured insertion loss of three different Kevlar fabrics in an anechoic room [64], and Remillieux et al. determined the loss of Kevlar in the Virginia Tech wind tunnel [78] with updated results in [70], that also accounted for losses due to the turbulent boundary layer. Both studies [78, 70] found that the Kevlar loss is generally an increasing function of frequency but exhibits a fluctuating or resonant behavior. A quadratic fit over flow speed and frequency was determined [70]. With the same methodology similar findings were reported in [73, 75]. These studies used a standard loudspeaker in combination with one or several microphones, e.g., a microphone array. However, since the development of an acoustic laser-based source [79, 80, 81], an alternative method has gained traction in the hybrid wind tunnel community [82, 74, 83]. A comparison and discussion of their results is given in Paper C.

The work done in the above-mentioned studies, has given insight into the losses due to Kevlar and TBL in the hybrid test section, but the general question about the nature of Kevlar and TBL loss still persist. In the following section, the characteristics of the PLCT test section, and related Kevlar and

TBL losses are investigated.

4.3 PLCT test section

The test section in PLCT can operate in two configurations, hard walls for aerodynamic tests, and Kevlar walls for acoustic test. Some aerodynamic tests can be conducted simultaneously with acoustic tests in the Kevlar wall configuration. An overview of the test section is shown in Fig. 4.1 and Fig. 4.2. Images of the test section with and without Kevlar walls are shown in Fig. 4.3. The dimensions are $2\text{ m} \times 3\text{ m} \times 9\text{ m}$ ($H \times W \times L$), with Kevlar walls covering 6 m. Surrounding the test section is an anechoic room with dimensions $11.5\text{ m} \times 11\text{ m} \times 13\text{ m}$ ($H \times W \times L$) (anechoic dimensions are given by subtracting, from each dimension, twice the wedge length of 0.9 m), that was validated according to EN/DS ISO 3745 [84] and is anechoic at frequencies above 100 Hz. Typically, a measurement session will consist of tests in both hard wall

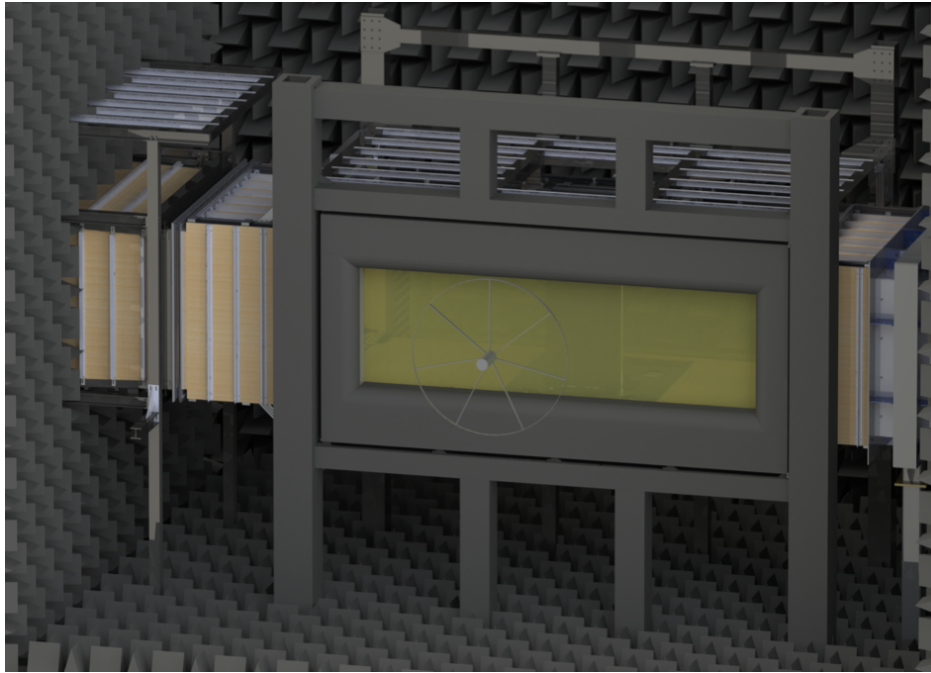


Figure 4.1: PLCT test section. Flow direction is right to left. The microphone array is shown in the front of a Kevlar wall. Image credit: Sigurd Ildvedsen.

and Kevlar wall configuration. Aerodynamic results are used in conjunction with the acoustic results to give a complete picture of the test object. In order to combine results from different measurement setups, aerodynamic data from the hard wall configuration must match the Kevlar configuration. Aero-

dynamic corrections due to the Kevlar wall was a topic of the PhD thesis by Brown [77]. The corrections applied in PLCT are developed from that work.

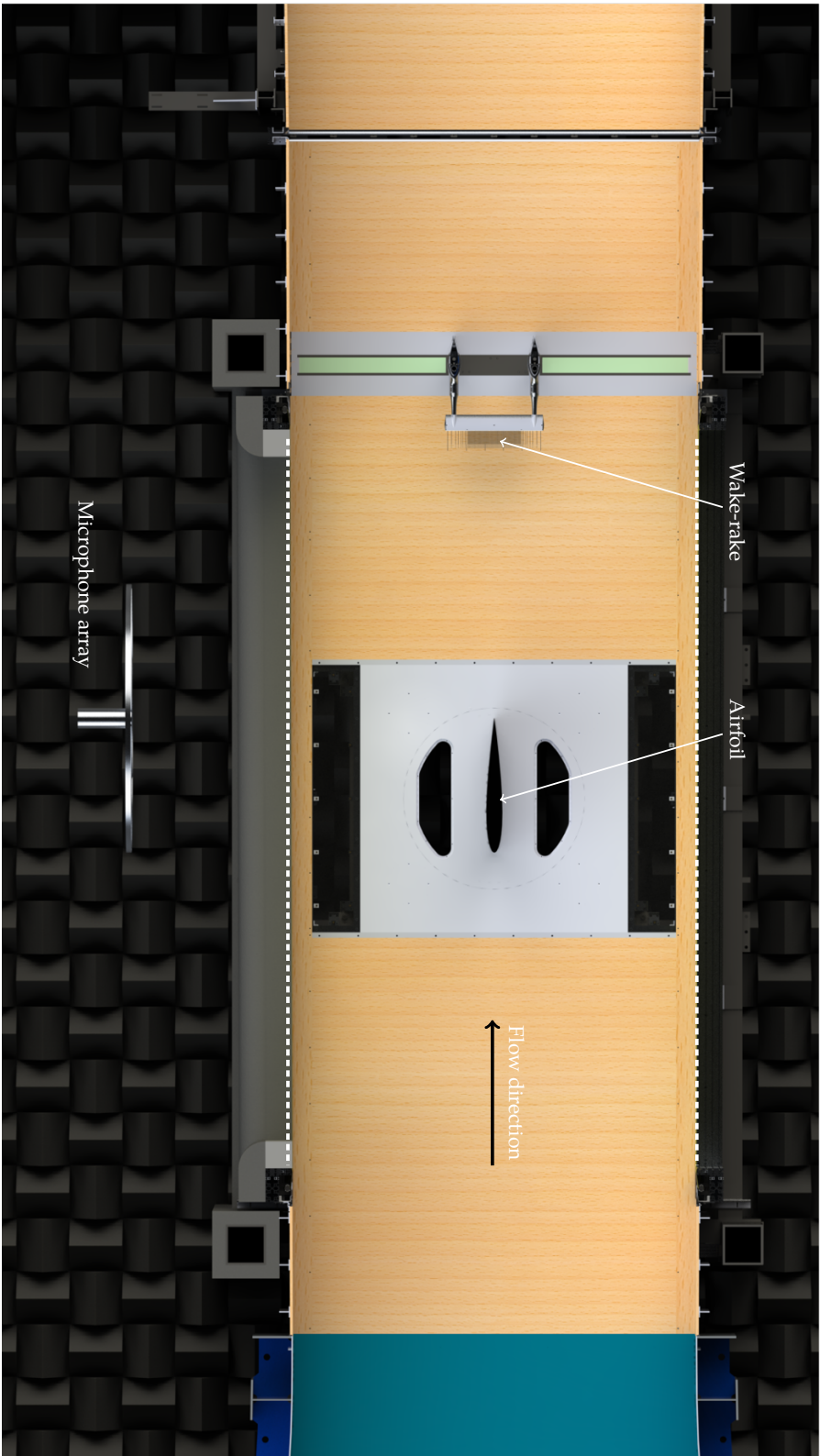


Figure 4.2: PLCT test section. Kevlar walls shown in dashed. Image credit: Sigurd Ilvedsen.



Figure 4.3: PLCT test section. Top image shows a loudspeaker inside the test section without Kevlar walls and the microphone array outside in the anechoic room. Bottom image shows a loudspeaker and a microphone in test section with Kevlar walls mounted.

PLCT microphone array

The microphone array consists of 84 microphones (B&K Type 4958) arranged in a 'sliced wheel' configuration (sometimes referred to as the "pizza array") with a diameter of 2 m. The pattern consist of 7 "slices" of an irregular geometry, which yields a pseudo-random pattern (shown in Figure 4.4). To evaluate

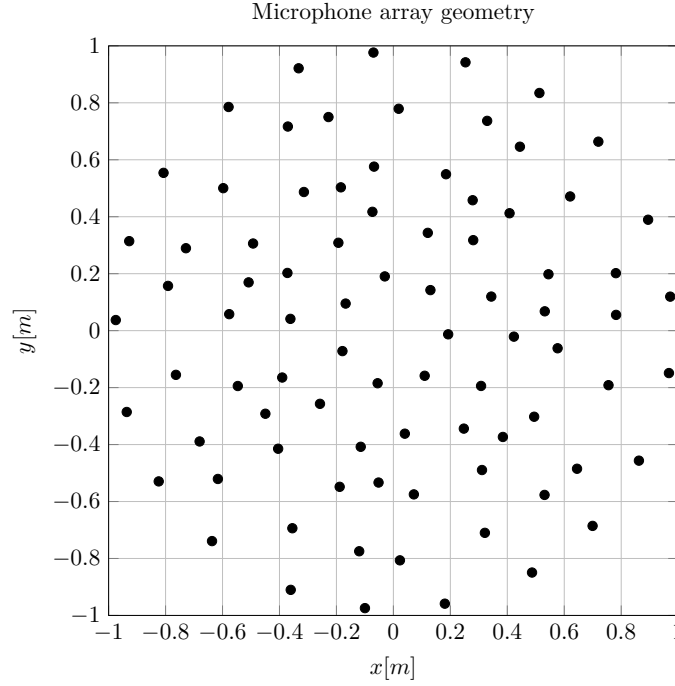


Figure 4.4: PLCT microphone geometry in a pseudo-random pattern.

the performance of the microphone array, the array pattern is calculated,

$$W(\mathbf{K}) = \sum_{m=1}^M e^{j\mathbf{K}\mathbf{r}_m}, \quad (4.1)$$

where $\mathbf{K} = \mathbf{k} - \mathbf{k}_0$, \mathbf{k} and \mathbf{k}_0 is the wave vector of the steering direction and direction of incoming plane wave, respectively, \mathbf{r}_m is the position of the m th microphone (assuming that the array center is placed in Origo of the coordinate system) [28]. Calculating the array pattern $W(\mathbf{K})$ for all possible \mathbf{K} within an opening angle of 90° and fixing the maximum level at each frequency, yields the Maximum Sidelobe Level (MSL), shown in Figure 4.5. This figure corresponds to a worst-case, since an opening angle of 90° rarely will be used. The MSL can be used to evaluate the upper frequency limit of the array. Setting a requirement on the maximum MSL, e.g., -15 dB, the upper frequency limit is just below 3kHz. In practise a MSL of -10 dB is often sufficient, which gives a

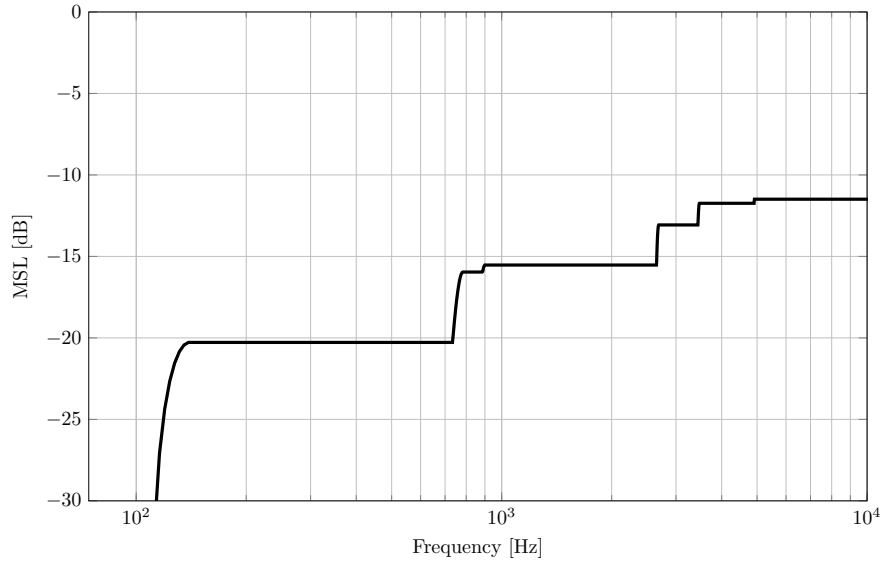


Figure 4.5: Maximum Sidelobe Level at opening angle of 90° .

upper frequency limit above 10 kHz. The lower frequency limit is estimated by the size of the array, $f_{\min} \approx c/D = 171\text{Hz}$, where c is the speed of sound and D is the diameter of the microphone array (2 m) [28]. The point spread function (PSF), defined in Eq. (3.8), is shown Fig. 4.6 at measurement distance of 2.7 m. The width of the main lobe is clearly decreasing with frequency as predicted by the Rayleigh criterion, Eq. (3.7). At 4000 Hz, side lobe contamination are seen near the boundaries of the plot and agrees with the MSL plot in Fig. 4.5.

PLCT dimensions and valid frequency range

Examples of beamforming maps with diagonal removal of an airfoil measured in PLCT is shown in Fig. 4.7. This is a NACA63018 airfoil that is analyzed thoroughly in the next chapter, but as precursor to that, Fig. 4.7 serves as an example for the discussion on the frequency range of measurements. The trailing edge noise is seen as a line source in the beamforming plots. Vertical lines indicate position of the airfoil, and the square indicates a typical integration region. A clear trend in the width of the line source is observed. This is in line with the observed width of the point spread function in Fig. 3.8 and Rayleigh criterion in Eq. (3.7). At the highest frequency shown, 5000 Hz, the background noise and MSL of the microphone array start to deteriorate the result. At 3150 Hz, strong sources are seen in the junction between floor and ceiling. This is a common issue, that can arise if small gaps are present between airfoil and floor and ceiling. The issue can be relieved with aluminium tape, but in this particular case, there is still some junction noise. And it ex-

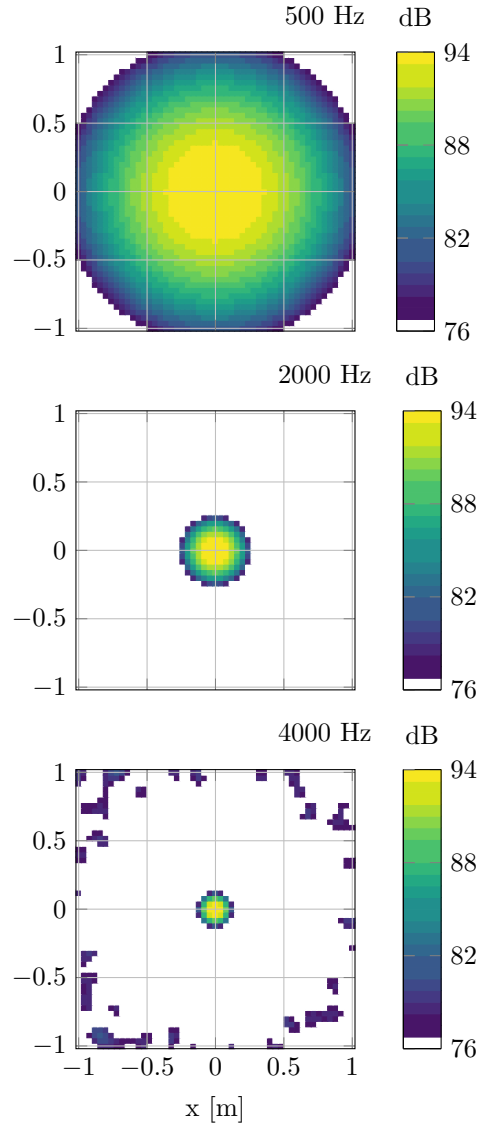


Figure 4.6: Point spread function (PSF). Dynamic range 18 dB, distance 2.7 m.

emphasizes the need for a frequency limit of measurements. Due to the increase in width of the PSF with decreasing frequency, at a particular frequency, this potential source would overlap with the integration region, causing an over-estimation of the source power. In this example, the integration region is positioned from -0.4 m 0.4 m in the y -axis, and the ceiling and floor is at ± 1 m, respectively. Hence, if the distance from the boundary of the integration region to a source at one of the junctions is larger than 0.6 m, the source power

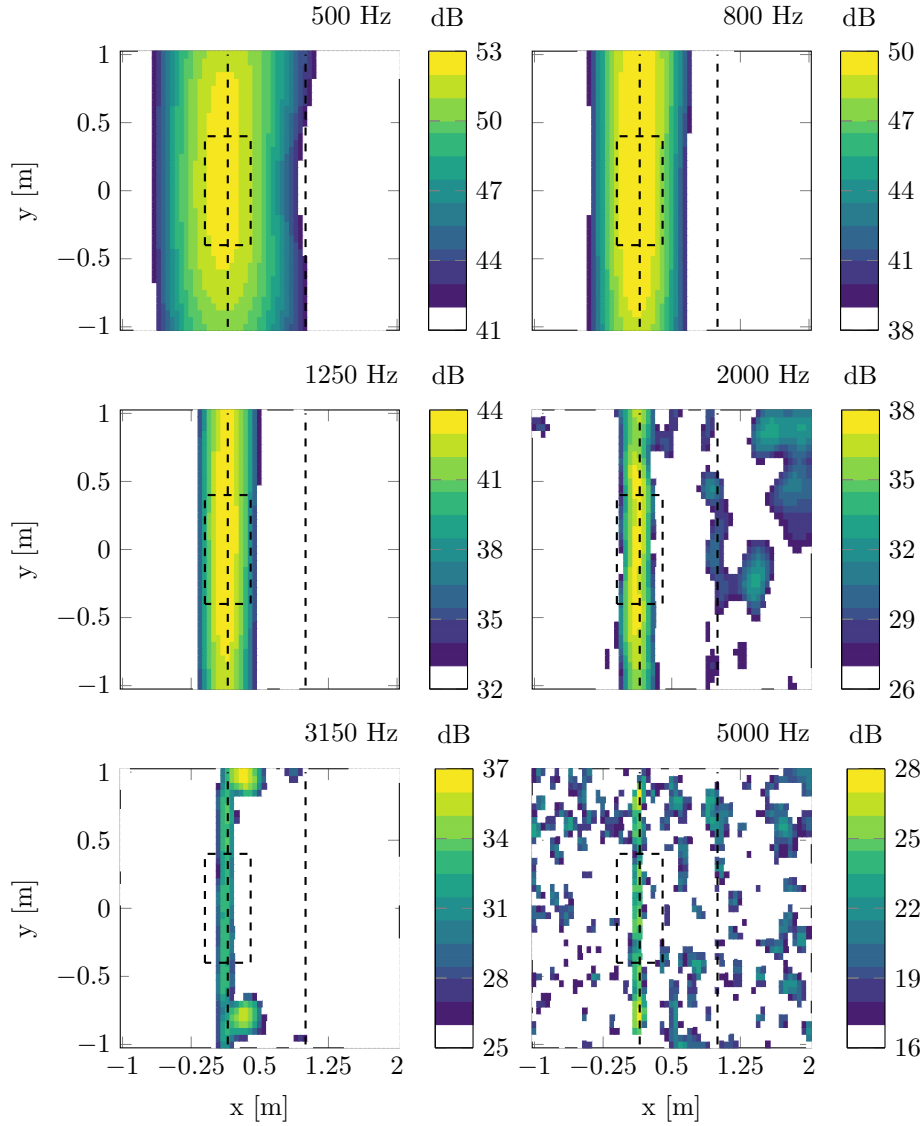


Figure 4.7: Beamforming maps with diagonal removal of a NACA63018 airfoil measured in PLCT.

could be overestimated. Using Rayleigh's criterion Eq. (3.7)

$$R_{min} = 1.22 \frac{z_0 c}{D f_{min}} = 0.6 \text{ m} \Leftrightarrow \quad (4.2)$$

$$f_{min} = 1.22 \frac{z_0 c}{D \cdot 0.6} = 970 \text{ Hz}, \quad (4.3)$$

using $z_0 = 2.785 \text{ m}$, $c = 343 \text{ m/s}$, $D = 2 \text{ m}$. This is a slightly conservative estimate, but gives an indication of possible overestimation when consider-

ing measurement results. The high frequency limit is due to the MSL, but more importantly, the signal-to-noise ratio of the measurement, which is case dependent and therefore not possible to predefine.

4.4 Kevlar losses

Continuing the discussion from previous sections, and with an overview of the PLCT hybrid test section in place, it is now possible to initiate the investigation of Kevlar losses. In the following, the Kevlar fabric will be introduced and a summary of Paper C, which is concerned with the insertion loss of Kevlar and TBL loss, is given. Further experimental results of Kevlar IL measurements are shown and compared to the results in Paper C. Finally, a comparison of all methods are presented and discussed.

Kevlar is a synthetic fibre that can be spun into threads with high tensile strength and weaved to a fabric. It is also very light and has a low acoustic impedance. A pre-investigation of Kevlar weave samples was conducted prior to ordering. Two different weaves were tested with properties defined in Tables 4.2, and 4.3. The two weaves are based on the same Kevlar fibre, with

Table 4.2: Standard Style 120 (Kevlar 13/13)

Setting warp	13.5 Thr/cm
Setting weft	13.5 Thr/cm
Fabric	Kevlar 49 T965 (215 dtex)
Weight	ca. 63 g/m ²
OAR	0.05

Table 4.3: Custom Style 120 (Kevlar 15/15)

Setting warp	15.0 Thr/cm
Setting weft	15.0 Thr/cm
Fabric	Kevlar 49 T965 (215 dtex)
Weight	ca. 68 g/m ²
OAR	ca. 0.02

the Standard Style 120 (Kevlar 13/13) being similar to the ones used in [70, 82, 75] that reports densities of 58 g/m²-61 g/m², Ref. [73] reports a slightly higher density of 79 g/m².

Impedance tube method

The insertion loss of Kevlar was estimated in an impedance tube measurement conducted at the Acoustic Technology group at DTU Elektro (Lyngby, Denmark). The setup consisted of two square aluminium tubes, with one end

backed by a loudspeaker and the other end closed with absorbing mineral wool. In the intersection between the tubes, a sample of Kevlar was fixed and the tubes were collected with screws. It was not possible to tension the Kevlar sample. The normal incident insertion loss was measured with microphones mounted in the top of the impedance tube. In two series of measurements, the transfer function between two flush-mounted microphones was computed, with and without a Kevlar sample in place. The transfer functions were summed into 1/3 octave bands and the insertion loss estimated as the difference between the two. The results are shown in Fig. 4.8 for the two different Kevlar samples mentioned in Tables 4.2 and 4.3. The Kevlar insertion loss is

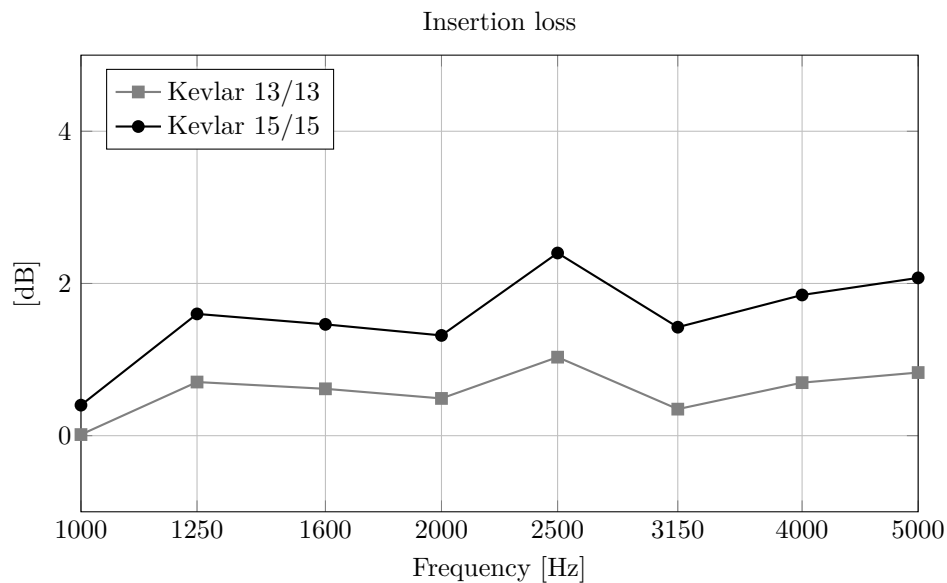


Figure 4.8: Insertion loss of Kevlar 13/13 and Kevlar 15/15 measured in an impedance tube.

seen to increase slowly from 1000 Hz to 5000 Hz. Below 1000 Hz, duct modes were dominating and causing non-physical results. Above 5000 Hz, higher order modes in the duct resulted in a mismatch between measurement, causing unrealistic results. The difference between the two fabrics is clear, with the Standard Style 120 (Kevlar 13/13) being approximately 1 dB lower in most bands, and increasing more slowly than the Custom Style 120 (Kevlar 15/15).

Impulse response method

The impulse response is by definition a (linear) system's response to an very short time signal [85], and its determination is a fundamental task in experimental room acoustics. It can be studied in the time-domain or in the frequency-domain (called transfer functions) and many characteristics of the

system can be derived from it. The insertion loss of Kevlar was also measured in the PLCT test section with and without tensioned Kevlar (images in Fig. 4.3). A loudspeaker was placed in the center of the test section and a swept-sine signal was used. The impulse response was captured for all microphones in the microphone array. A low-pass filter and a window function was applied, shown in Fig. 4.9. A CSM was computed from the impulse responses, and beamforming and source integration was conducted. The insertion loss is the ratio of the source integration results with a free-field correction to account for different measurement distances. The narrowband results are shown in Fig. 4.9. Due to higher-order modes in the loudspeaker, a large resonance peak is seen between 3000 Hz and 4000 Hz. This is due to directivity effects, since the microphone array and loudspeaker was not placed in the same position between measurements. Overall, the insertion loss of Kevlar is seen to increase with frequency in a similar manner as the impedance tube results, shown above. Above the resonance peak, around 4000 Hz, the insertion loss is about 3 dB and slightly higher than the impedance tube results.

A third method for estimation of Kevlar IL and a method for estimation of turbulent boundary layer loss, based on beamforming, is described in Paper C. The reader is invited to read Paper C at this point, or continue with a summary of it below.

4.5 Summary of Paper C

Acoustic level corrections for a Kevlar-walled wind tunnel.

Paper C is about the level loss that occurs when a sound wave propagates from a medium with uniform flow, through a Kevlar wall, and to a microphone array in a quiescent medium. The focus is on estimating the insertion loss of Kevlar and turbulent boundary layer (TBL) loss. The method consists of placing a loudspeaker on one side of the test section, and measuring the level on the opposite side of the test section, through two Kevlar walls. The reference level of the loudspeaker is measured with a volume velocity tube. The Kevlar loss was found, at zero-flow, by the difference between the reference level from the volume velocity tube, and Source Power Integration (SPI) of beamforming maps. The results showed a frequency dependent increase in Kevlar insertion loss. Interference from test section floor and ceiling made the results below 1000 Hz unreliable, and higher-order modes in the volume velocity tube caused the Kevlar IL to become negative above 4000 Hz. The TBL loss was estimated at 7 flow velocities by first deriving a refraction correction for two shear layers, and then applying it to beamforming maps. SPI was used to obtain noise spectra that was compared to the reference level from the volume velocity tube. A TBL loss that scaled linearly with Mach number

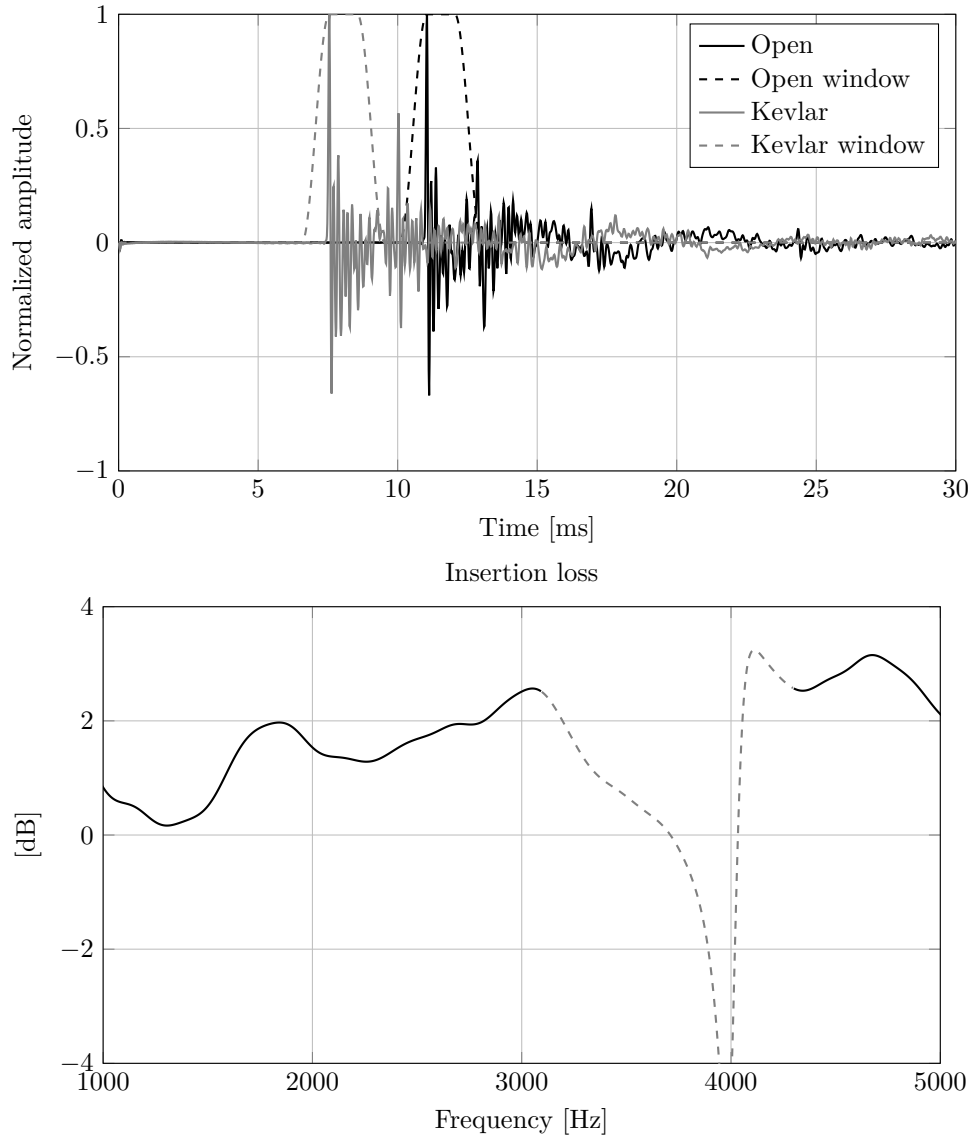


Figure 4.9: Kevlar impulse responses (top) and insertion loss (bottom).

was found, and a simple curve fit was determined,

$$\alpha_1 \cdot \left(1 - e^{-(\beta \cdot f)^2}\right) \cdot Ma, \quad (4.4)$$

where $\beta = 0.00125$ and $\alpha_1 = 10$.

Comparison of Kevlar insertion loss

Three different methods have been used for estimating the Kevlar insertion loss; the impedance tube method with an un-tensioned Kevlar sample, the impulse response method, that compared two impulse response measurements in the test section, with and without Kevlar. Finally, in Paper C, a method was proposed to estimate Kevlar insertion loss using a volume velocity tube attached to a loudspeaker reference source. A comparison of the results are shown in Fig. 4.10. Within the frequency range 1000 Hz to 2200 Hz, a similar

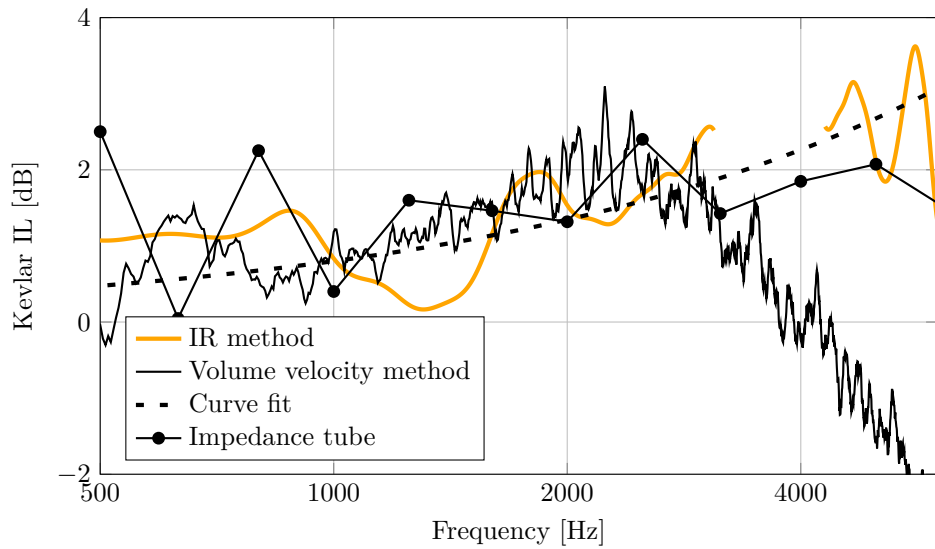


Figure 4.10: Comparison of Kevlar insertion loss (IL) determined by the impulse response (IR) method, volume velocity method and impedance tube method. A simple curve fit is shown in dashed.

trend is seen between the three methods with variations of 1-2 dB. A rough curve fit is found,

$$\Delta\text{Kevlar} = a \cdot (f/1000)^{0.75}, \quad (4.5)$$

where $a = 0.8$. This is based on "eye-balling" the general trend. A more scientific approach would have been a nonlinear regression between the three estimates, however, the question then arises: What type of model is expected? And how should each method be weighted in the regression? For instance, the impedance tube method did not hold a tensioned Kevlar sample, is that equally good as a method in the test section with the actual tensioned Kevlar wall? The curve fit in Fig. 4.10 is a lack of a better alternative and shows that it is difficult to find a reliable method for estimating the Kevlar IL.

4.6 Conclusion

In this chapter, three test section designs was described and the hybrid test section in PLCT was presented. The Kevlar insertion loss was estimated through three different methods, and a simple curve fit was found that scales with frequency. The turbulent boundary layer loss was estimated in Paper C, where a linear Mach scaling was observed. Issues with measurement equipment and conditions led to large variations in the results, showing the need for more research on these topics. Future work should address how tension of Kevlar affects the insertion loss and TBL loss, and investigate possible structural vibrations. Effects of the boundary layer thickness on the TBL loss could hopefully give a better physical understanding and make comparisons between facilities easier.

Chapter 5

Noise quantification of a NACA63018 airfoil

With the knowledge about background noise in the tunnel and the effects of sound propagation in the Kevlar-walled test section, it is now possible to address the last objective of this thesis: Quantification of trailing edge noise. The theoretical basis was given in Chapter 3, with beamforming, Source Power Integration (SPI) and deconvolution introduced as methods for quantifying noise. In this chapter, measurements of a NACA63018 airfoil in the Poul la Cour Tunnel (PLCT) are presented and three methods applied to obtain estimates of the trailing edge noise: DAS beamforming with SPI, CLEAN-SC and DAMAS.

5.1 Benchmark validation

The aeroacoustic community has produced benchmark test cases for cross-validation of existing methods and for validation of new algorithms [58, 57]. The numerical code used throughout this dissertation, is implemented in the open source package AeroAcoustics.jl [86], which has been developed as part of the PhD study. It is written in Julia [87] and made open source to benefit other researchers and reproducible research in general. Another open-source project is Acoular [88]. The NASA2 benchmark, described in [57], is used to validate the numerical implementations included in the AeroAcoustics.jl package. The NASA2 benchmark test case consists of measurements originally conducted at the Quiet Flow Facility (QFF) at NASA and published in [49]. The results from [49] with DAMAS and diagonal removal (DR), given in dB (1/3 octave bands) per foot span, are compared to three methods implemented in the AeroAcoustics.jl package: DAS, CLEAN-SC and DAMAS. Diagonal removal is applied to all methods and the results for leading and trailing edge noise, given in dB per foot span, are shown in Fig. 5.1. The leading and trailing edge noise is dominating the high and low end of the spectra,

respectively, with a cross-over at 12 000 Hz. Using the original source integra-

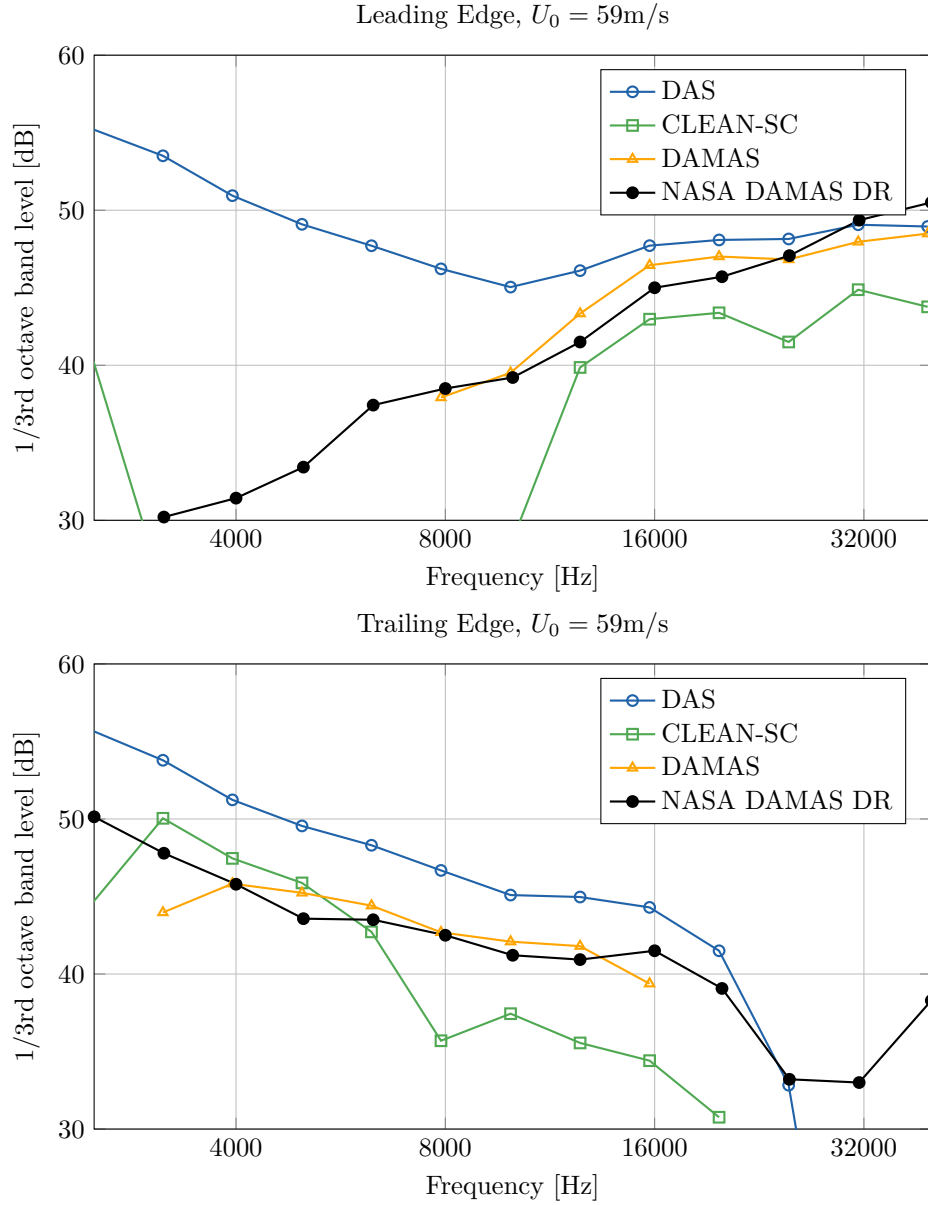


Figure 5.1: Noise quantification of leading edge (top) and trailing edge (bottom) of benchmark test case NASA2. Results of delay-and-sum (DAS) beam-forming with source integration, CLEAN-SC, and DAMAS. Measurements by Brooks and Humphreys presented in [49] with DAMAS and diagonal removal (NASA DAMAS DR) and made available as test case by Chris Bahr, NASA.

tion with DAMAS from [49] (NASA DAMAS DR) as a reference, the results

of DAS beamforming with SPI and CLEAN-SC from AeroAcoustics.jl are not satisfactory. Only a few of the 1/3 octave bands are close to the reference level. For DAS, this is an expected results, since the leading and trailing edge was only separated by 0.38 m. With a measurement distance of 1.66 m and a microphone array diameter of 0.2 m, the lower frequency limit, stated in Eq. (4.3), is 9000 Hz. This is clearly seen in the leading edge results in the top plot of Fig. 5.1. For CLEAN-SC and DAMAS, the results align best with the reference when the corresponding source is dominating, that is, above 8000 Hz for the leading edge noise, and below 12 000 Hz for trailing edge noise. CLEAN-SC shows large variations in results, whereas, the DAMAS implementation in AeroAcoustics.jl follows the reference (NASA DAMAS DR) within a few dB in a large frequency range. However, the DAMAS implementation is not capable of resolving the source (leading or trailing edge) when another dominating source is present, seen in the lack of leading edge results below 8000 Hz and trailing edge results above 16 000 Hz.

5.2 NACA 63018 validation

The NACA 63018 airfoil was chosen as reference airfoil for validating the acoustic capabilities of PLCT. It is a symmetric airfoil with chord length 0.9 m and span of 2 m. It was constructed with very high precision and trailing edge thickness of 1.35 mm.

The measurements were conducted at three different flow speeds and angles of attach ranging from $\pm 16^\circ$. In the presentation below, a subset of measurements have been selected, and summarized in Table 5.1. The microphone

Ma [-]	U_0 [m/s]	Re [-]	α [°]
0.099	33.52	2.13e6	0
0.147	49.47	3.13e6	0
0.146	49.19	3.11e6	-4
0.143	48.06	3.06e6	-8
0.143	48.34	3.07e6	4
0.140	47.34	3.00e6	8
0.198	66.83	4.21e6	0

Table 5.1: NACA 63018 noise measurement parameters. Reynolds number referenced to chord length 0.9 m.

array, situated at a distance of 2.785 m from the center of the test section, was used to record 20 s time sequences with a sample rate of 65 536 Hz, and 24 bit resolution. The time recordings were stored for further processing.

First, preparation of cross-spectral matrices using Welch's method [89] with a Hanning window of 16384 samples and 50% overlap, were computed, resulting in a frequency resolution of 4 Hz. Then, the cross-spectral matrices

were further compressed by summation into 1/12th octave bands in a frequency range of 200 Hz to 8 kHz. The subsequent analysis is based on these CSMs. Beamforming maps are computed from the CSMs, with steering vector that incorporates the time and amplitude correction derived in Paper C. From the beamforming maps, three methods are used to estimate integrated spectra: Source power integration (SPI), DAMAS, and CLEAN-SC. All methods use an integration region over the trailing edge of the airfoil, centered at mid-span $(\Delta x, \Delta y) = (0.5, 0.8)\text{m}$. The result is given in dB per meter span by dividing by Δy , and finally, Kevlar and TBL corrections, found in Paper C, are applied.

Signal-to-noise ratio

A comparison of the background noise and airfoil measurement noise, is computed by their respective autospectra from the array microphone mean. The background noise, measured in the empty tunnel, and airfoil noise, compared at closest possible flow speeds are shown in Fig. 5.2. Around $U_0 = 50\text{ m/s}$ the background noise and airfoil noise is captured at very similar flow speeds. There is a positive signal-to-noise ratio below approximately 1800 Hz. However, at higher frequencies, the background noise is dominating the autospectra, which demonstrate the need for microphone array methods. At all flow speeds, the pitot tube, that was mentioned in Sec. 2.4, gives a clear peak in the autospectra. Since the pitot tube is situated about 2 m upstream of the airfoil, it is in most cases possible to filter away that noise by source integration of the acoustic maps.

Trailing edge noise model

A trailing edge noise (TEN) model is used to validate measurements in the following analysis. The TEN model is described in [90]. It is a derivative of the the so-called TNO trailing edge nose model [91], but has been improved in various aspects. It uses CFD RANS [92] computations to obtain the mean flow and turbulence characteristics in the boundary layer of the airfoil. Turbulence spectra are modelled with the empirical model of von Karman [93] and the surface pressure fluctuations are calculated using the solution of the Poisson equation derived in [94]. Finally the far field trailing edge noise is computed using the theoretical framework that was summarized by Howe [9]. The model does not take trailing edge bluntness into account.

Kevlar corrections

In Paper C, acoustic level corrections due to Kevlar IL and TBL loss, were estimated experimentally. Combined with the experimental results presented

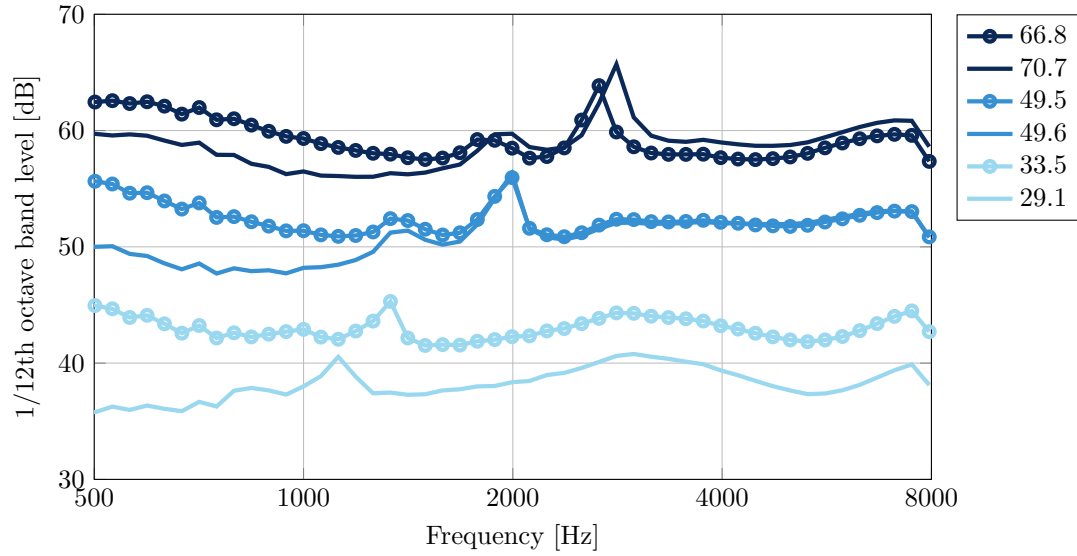


Figure 5.2: Autospectra of background noise (solid) at three flow speeds [m/s] and airfoil measurement noise (solid with markers) at three (similar) flow speeds.

in Chapter 4, the curve fit functions are

$$\Delta Kevlar = 0.8 \cdot (f/1000)^{0.75} \quad (5.1)$$

$$\Delta TBL = 10 \cdot \left(1 - e^{-(0.00125 \cdot f)^2}\right) Ma. \quad (5.2)$$

These functions are shown for three flow speeds in Fig. 5.3.

Refraction correction

The sound propagation from airfoil to microphone array traverses a velocity discontinuity at the Kevlar wall and refraction of sound occurs. This can be modelled by a ray-tracing procedure described by Amiet [8] as a shear-layer correction. A derivation over two shear layers was given in Paper C. With small modifications to that, a refraction correction for a plane shear-layer situated at the Kevlar wall is used in the following. The propagation time correction in Paper C divided the path from source to microphone, r , into three sub paths, $r = r_1 + r_2 + r_3$, where r_1 was the path from the source opposite of the test section and microphone array to the first Kevlar wall, r_2 the path through the test section to the second Kevlar wall, and r_3 , the path from the Kevlar wall to microphone (Fig. 2 in Paper C). Modifying this propagation path by setting $r_1 = 0$ and changing r_2 to be the path from source (airfoil at center of test section) to Kevlar wall, and following the derivations, a time

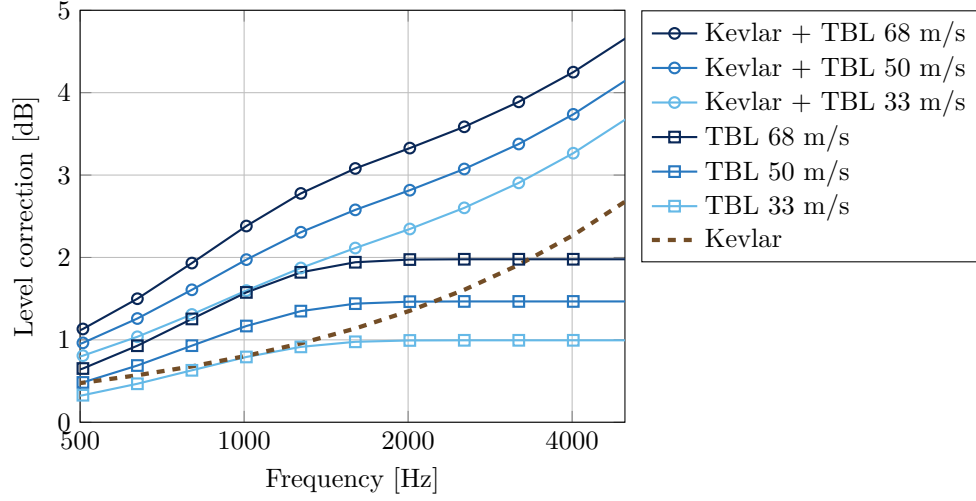


Figure 5.3: Kevlar insertion loss and turbulent boundary layer (TBL) loss.

correction is obtained. The amplitude correction, derived in Paper C, also accounted for the transmission loss over two shear layers. Equation (11) in Paper C states the sub-corrections to the amplitude. Modifying this by setting $\left| \frac{\hat{p}_{t1}}{\hat{p}_{t2}} \right|^2 = \left| \frac{\hat{p}_{i2}}{\hat{p}_{i1}} \right|^2 = 0$, the amplitude correction for a single shear layer is obtained. The combined correction is implemented in AeroAcoustics.jl [86] and an example at $U_0 = 49$ m/s is shown in Fig. 5.4.

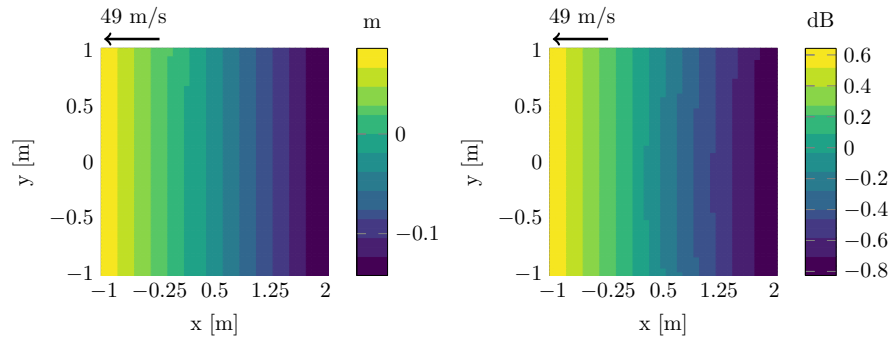


Figure 5.4: Refraction correction for a plane shear layer (situated in the Kevlar wall plane). Left: Propagation path correction relative to free-field propagation. Right: Amplitude correction.

Diagonal removal

An example of the standard beamforming results with and without diagonal removal (DR) are shown in Fig. 5.5. The effect of DR is dramatic and greatly improves the signal-to-noise ratio. Diagonal removal is used throughout the following analysis.

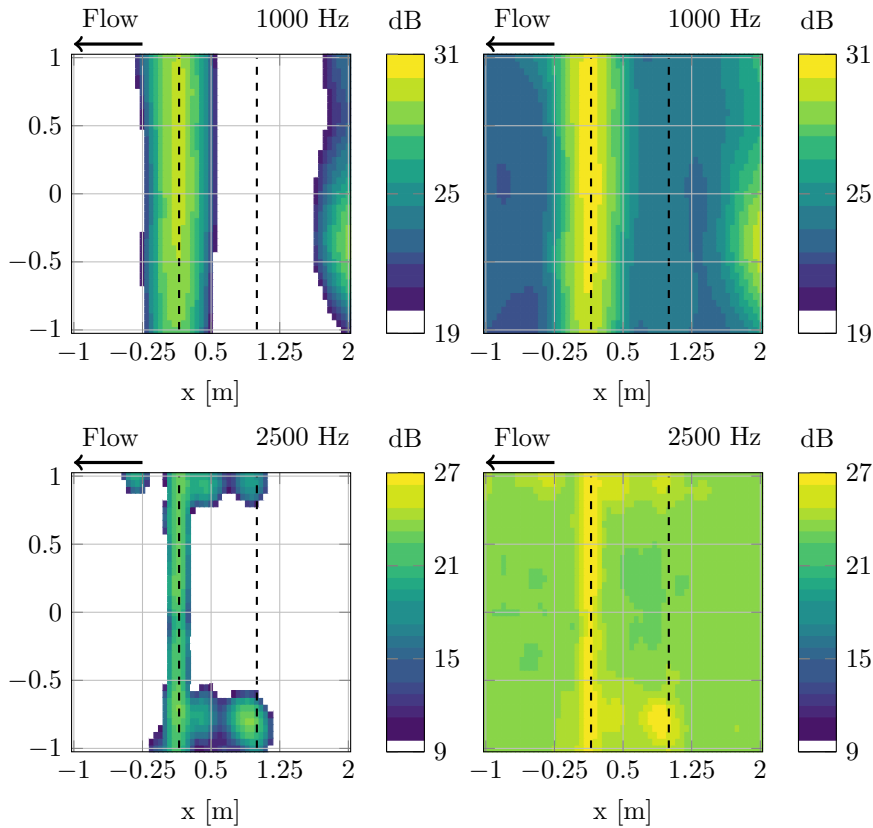


Figure 5.5: Beamforming with diagonal removal (left) and without (right). The dynamic range is 12 dB.

Beamforming

Beamforming maps with diagonal removal are shown in Fig. 5.6 from 500 Hz to 3500 Hz. In 5 of the beamforming maps, the trailing edge of the NACA63018 is clearly identified. At 1496 Hz and 1995 Hz a dominant source is visible in the far right side, just outside the maps. This is the pitot tube that was mentioned in Chap. 2.4 and seen in the autospectra in Fig. 5.2. The peak is seen in the frequency range 1500 Hz to 2300 Hz and at 1995 Hz it is too dominating to get a clear map of the trailing edge. The reason is sidelobe contamination,

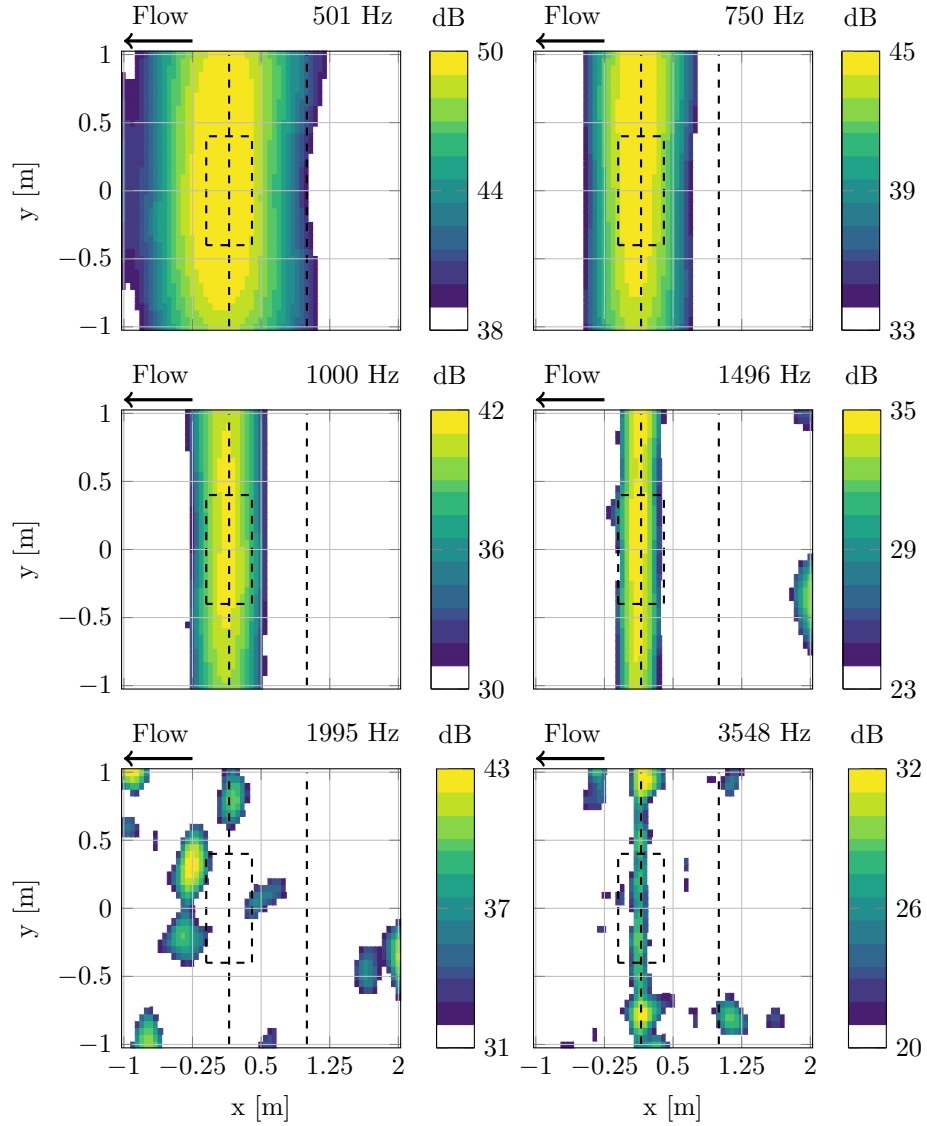


Figure 5.6: Beamforming maps of NACA63018 at $Re\ 3\ mio$, $U_0 = 49\ m/s$, $\alpha = 0^\circ$.

which is seen when plotting the point-spread function in Fig. 5.7. The theoretical array performance was described by the Maximum Sidelobe Level (MSL) and shown in Fig. 4.5. At 1995 Hz, the MSL is $-15\ dB$. If the peak level of the pitot tube is very high, its sidelobe level will be comparable to the trailing edge noise, effectively removing the trailing edge from the beamforming map. Source integration using DAS and SPI is shown in Fig. 5.8. The level corrections in Eq. (5.1) and (5.2). Overall, there is a good agreement between DAS and the TEN model. The level corrections due to Kevlar and TBL loss

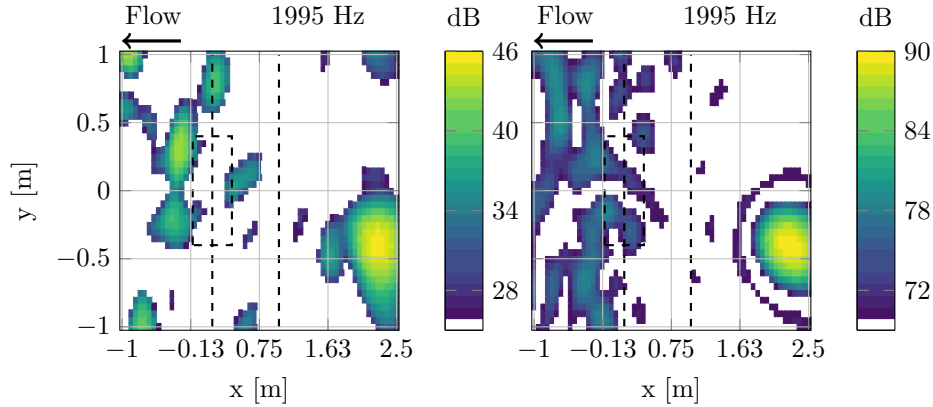


Figure 5.7: Left: Beamforming map of NACA63018 at 1995 Hz, $Re\ 3\ mio$, $U_0 = 49\ m/s$, $\alpha = 0^\circ$. Right: Point-spread function at peak source location. Sidelobe contamination is clearly seen in the integration region. The dynamic range is 21 dB.

provides a better fit from 1000 Hz than DAS without the level corrections. In both cases, below 750 Hz, an increasing deviation is observed. This could be related to overestimation of power below the Rayleigh limit (970 Hz) or uncertainties in the TEN model. At frequencies above 3000 Hz a broad hump is seen, with level increases up to 10 dB above the TEN model. This hump is due to trailing edge bluntness. Despite the lack of a visible trailing edge in the beamforming map at 1995 Hz, the source integration result only give a small 3 dB dip in level. A technique to improve this is presented in the following.

CLEAN-SC

To investigate the effect of the loop-gain parameter in CLEAN-SC, and to find a parameter that will be used in the subsequent analysis, a range of parameters are used for source integration and comparison with the TEN model is used as a reference value. In Fig. 5.9 source integration with $\phi = 0.2, 0.5, 0.9$ is shown. In the frequency range 600 Hz to 2000 Hz (approximately the range with a positive SNR), the levels are very similar and showing good agreement with the TEN model. However, from 2000 Hz to 4000 Hz, larger variation are starting to occur. Looking at the acoustic source maps in Fig. 5.9, a distributed line source is seen at 562 Hz, and a single dominant source is visible at 1995 Hz. To aid visualization, the pixel-sized values of the CLEAN-SC acoustic maps have been convolved with a gaussian filter. At low frequencies, the loop-gain parameter tends to distribute the line source into point sources for $\phi = 0.9$. At 1995 Hz, it is clear that the dominant source is the pitot tube, located about 2.5 m upstream of the trailing edge of the airfoil. This was also seen in the beamforming maps in Fig. 5.6. The source integration spectra in Fig. 5.9 have

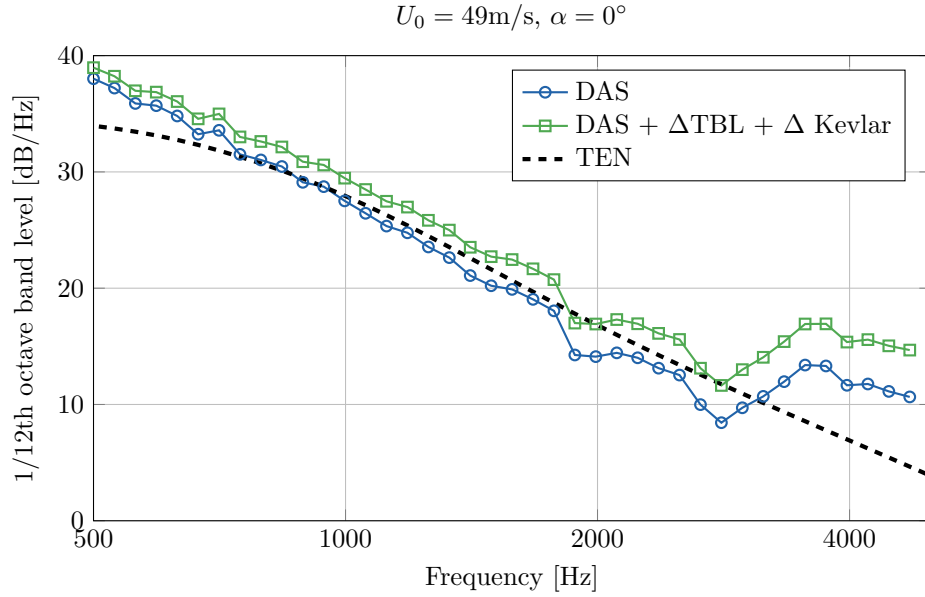


Figure 5.8: Source power integration of NACA63018 beamforming maps shown with and without level corrections due to turbulent boundary layer (TBL) loss and Kevlar insertion loss.

a small dip at this frequency that is not a characteristic of the airfoil. To remedy this, a practical solution would be to attempt to reduce the vortex shedding on the pitot tube or remove it completely. A post-processing technique is also possible, described by Sijtsma as "removal of dominant sources" [47]. Using this approach in the frequency range 1700 Hz to 2400 Hz, the trailing edge is recovered in the source maps shown in Fig. 5.11. To use this method, it is required that the source is visible in the maps, therefore the limits have been extended compared to the DAS maps in Fig. 5.6. Compared to Fig. 5.10, the maximum level is 6 dB lower by removing the dominant source. The distribution of the line source at the trailing edge is very similar across the three maps at 1995 Hz, and the tendency to distribute sources in clusters, that is seen at low frequencies, is not observed. Thus, in the following analysis, a loop-gain of $\phi = 0.5$ will be used, and the peak removal technique applied in frequency ranges where the pitot tube is known to be dominating.

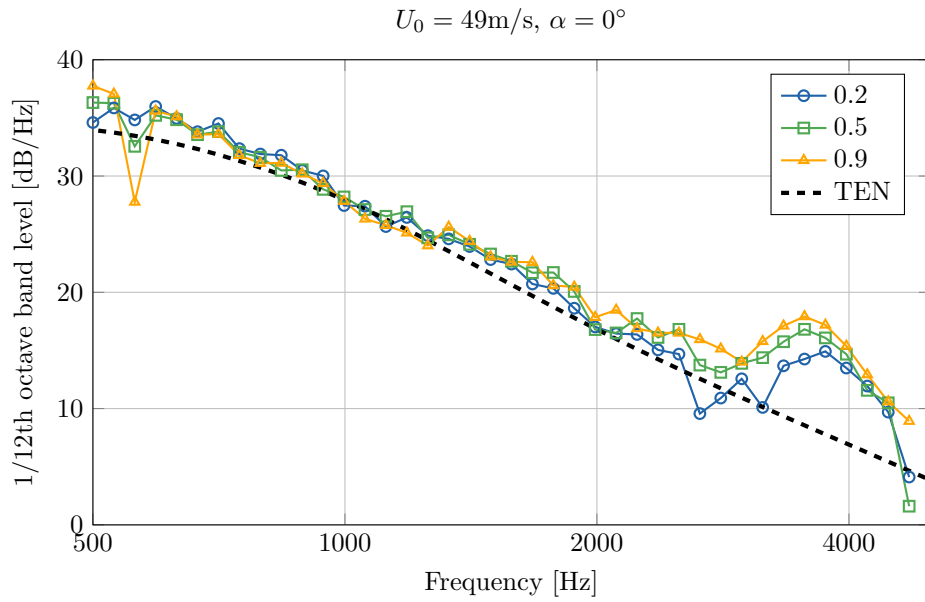


Figure 5.9: Source integration of NACA63018 airfoil with CLEAN-SC algorithm and three different loop gain parameters. Maximum number of iterations are 100.

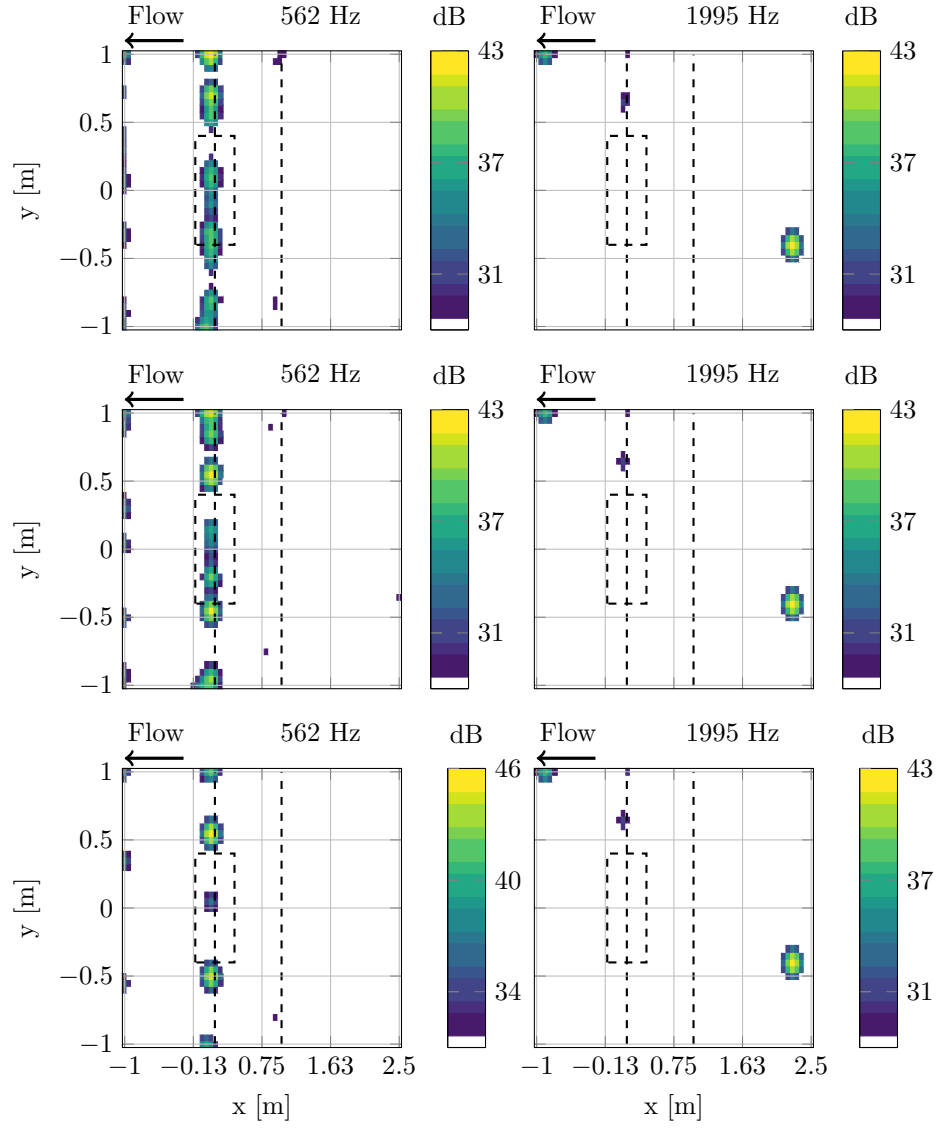


Figure 5.10: CLEAN-SC maps for two frequency bands with loop gain parameters $\phi = 0.2, 0.5, 0.9$ from top to bottom. Source maps are convolved with a Gaussian filter to aid visualization. Dynamic range is 15 dB.

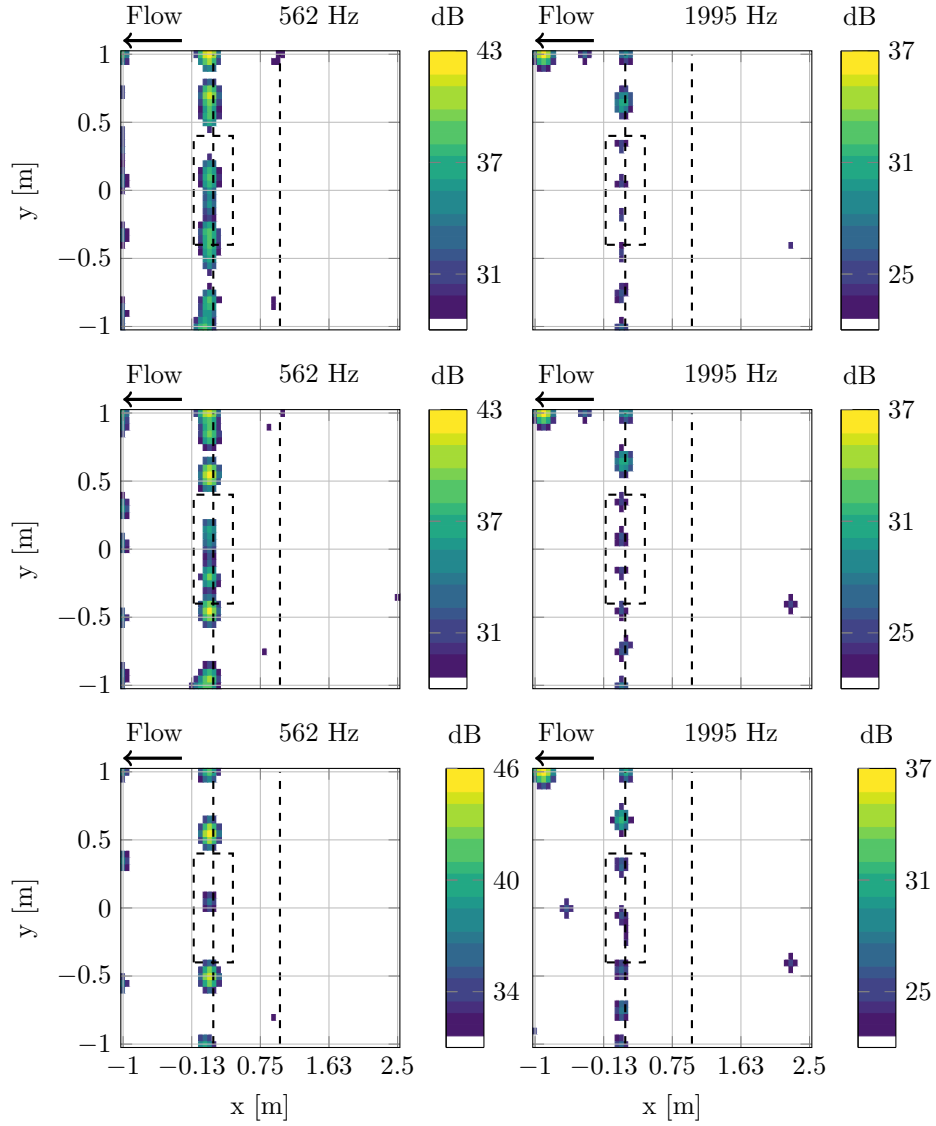


Figure 5.11: CLEAN-SC maps with removal of dominant peak source at 1995 Hz with loop gain parameters $\phi = 0.2, 0.5, 0.9$ from top to bottom.

DAMAS

In the benchmark validation of the NASA2 test case, described previously, the DAMAS method showed promising results. To investigate the effect of number of iterations with DAMAS, source integration is calculated at 50, 100, and 500 iterations. In Fig. 5.12, the number of DAMAS iterations is poorly reflected in the source integration spectra. Above 1000 Hz, there is almost no difference observed, which is also seen in the acoustic maps in Fig. 5.13. At 750 Hz, the width and distribution of the source is changing with number of iterations. At 2000 Hz there is a level decrease of about 5 dB due to the pitot tube, which is also seen in Fig. 5.13. As it was mentioned in the benchmark validation above, the DAMAS implementation fails to resolve the correct source when another dominating source is present. Below 1000 Hz, there are some discrepancies in the source integration results, however, due to the low resolution of beam-forming, it is not possible to conclude a consistent behavior of DAMAS. In the following, DAMAS is computed with 50 iterations.

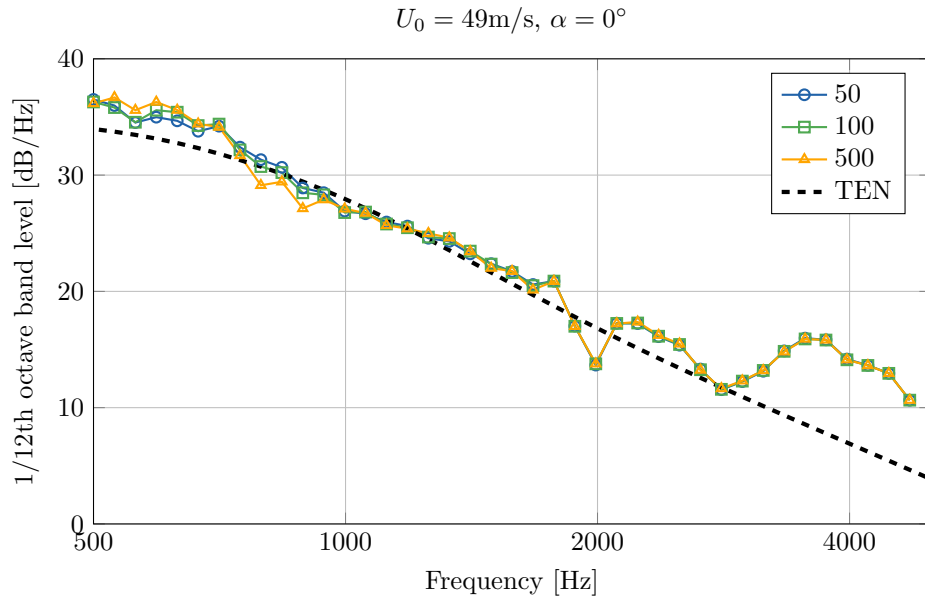


Figure 5.12: Source integration of NACA63018 airfoil with DAMAS algorithm and three different iterations.

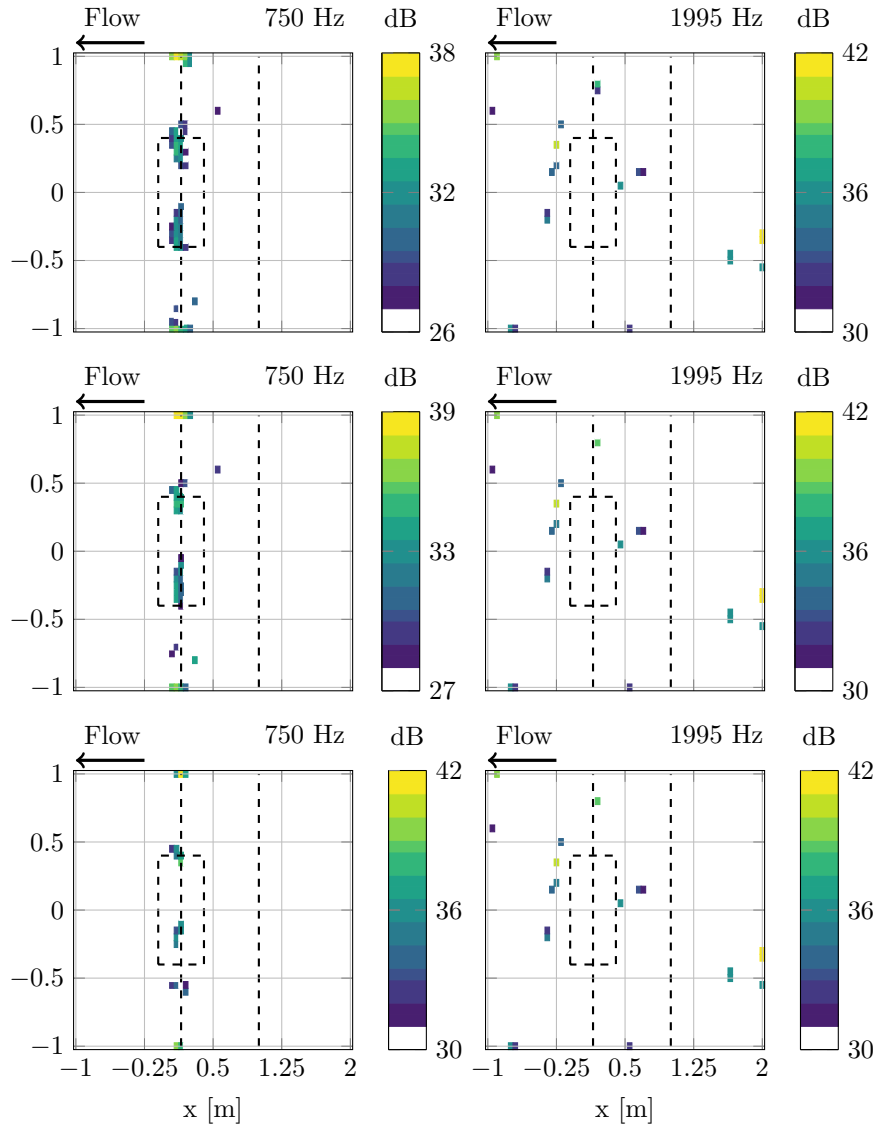


Figure 5.13: DAMAS maps for two frequency bands with 20, 50, 100 iterations from top to bottom.

5.3 Results

In the following sections, acoustic source maps and results of source integration with DAS, DAMAS, and CLEAN-SC are presented.

Re 3mio, zero angle of attack

The trailing edge noise of the NACA63018 airfoil at Reynolds number 3 mio and zero angle of attack is estimated with DAS, CLEAN-SC ($\phi = 0.5$ and 500 iterations) and DAMAS (50 iterations). Source integration results are shown in Fig. 5.14. Overall, a good agreement between methods and the TEN model is found. At low frequencies, below 750 Hz, the levels estimated by the TEN model is about 3 dB lower than the DAS, CLEAN-SC and DAMAS, increasing to about 5 dB for DAS at 500 Hz. The low frequency discrepancy is expected, since all the methods are based on beamforming and hence Rayleigh's criterion. In Eq. (4.3), a conservative lower frequency limit of 970 Hz was found. Around the frequency of the pitot peak, 2000 Hz, all three methods show a small dip in level, DAMAS being affected the most with about 8 dB. The lack of resolving secondary sources is a known issue with DAMAS, and was discussed above. At frequencies above 2000 Hz there is a very good agreement between the methods up to 4000 Hz. The deviation from the TEN model is due to TE bluntness noise that is not accounted for in the model. The acoustic source maps for 750 Hz and 1995 Hz are shown in Fig. 5.15. At 750 Hz the trailing edge is clearly visible in the beamforming map, which is expected due to a positive SNR. The DAMAS map shows a clustering of the trailing edge near mid-span and at the floor and ceiling of the test section. It was shown above, that increasing the number of iterations with DAMAS did not produce a significantly better source distribution, but it did decrease the width slightly. More importantly, it was shown that the source integration did not change with increasing number of iterations. The CLEAN-SC map does not show a trailing edge source, but the peak source has clearly been removed.

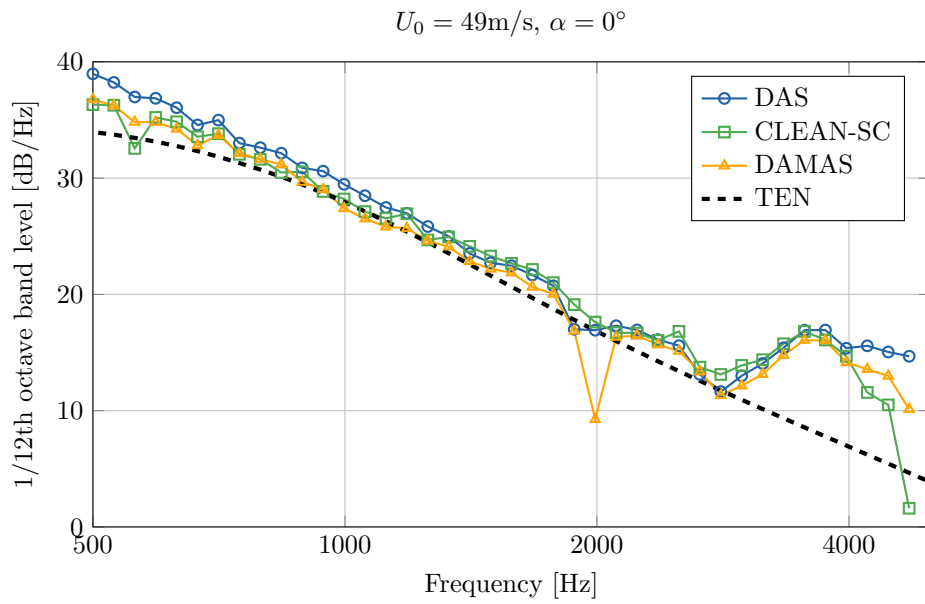


Figure 5.14: Comparison of algorithms for noise quantification on a NACA63018 airfoil

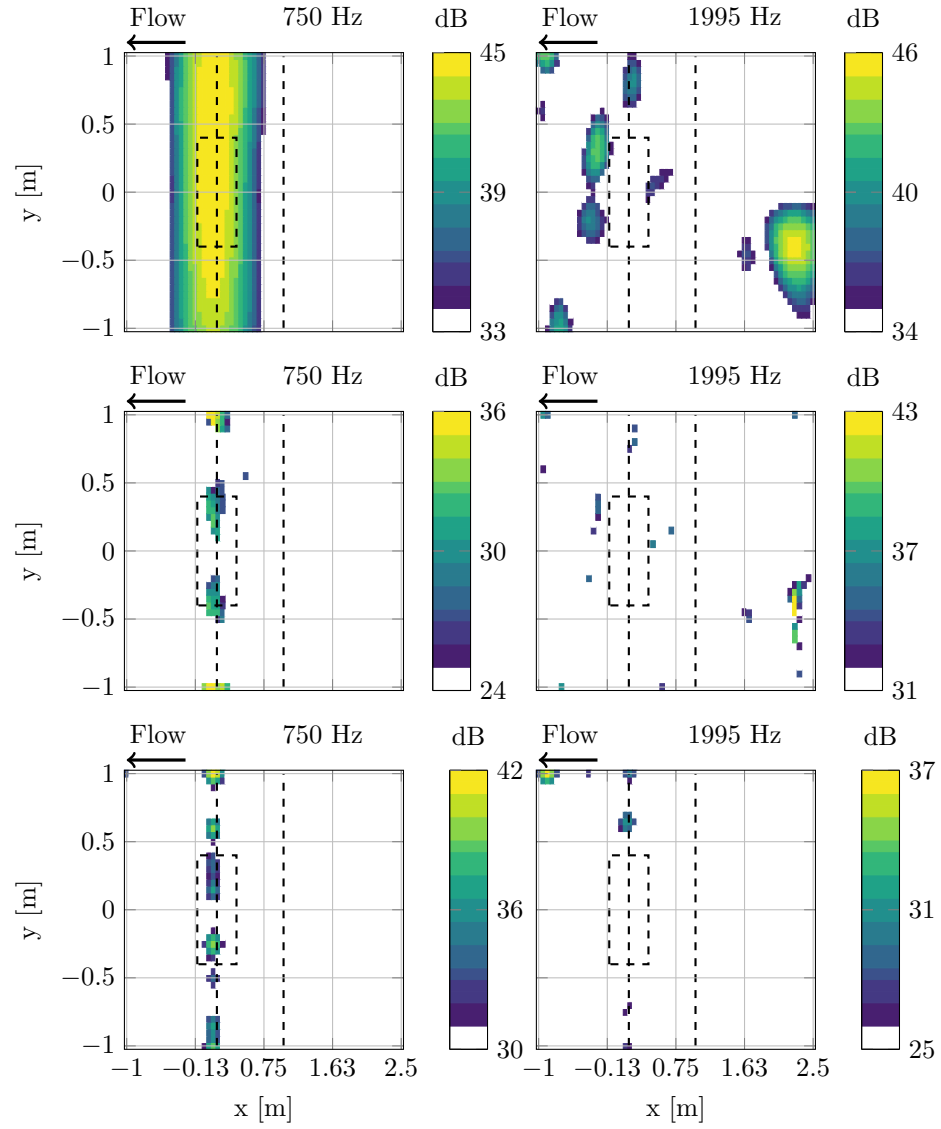


Figure 5.15: Comparison of algorithms for noise quantification on a NACA63018 airfoil. From top to bottom: Beamforming, DAMAS, and CLEAN-SC.

Re 3mio, angles of attack -8,-4,4,8

Following the procedure above for zero angle of attack, source integration results for $\alpha = -8, -4, 4, 8$ processed with CLEAN-SC are shown in Fig. 5.16 with deviations from $\alpha = 0^\circ$. Overall, a change in slope is seen with increasing angle of attack. At higher angles of attack, the boundary layer thickness on the airfoil increases, resulting in a frequency shift towards lower frequencies. Since the NACA63018 airfoil is symmetric, the noise emission is theoretically similar for positive and negative angles. However, the directivity of the trailing edge source changes and could potentially affect the results slightly, depending on the position of the microphone array.

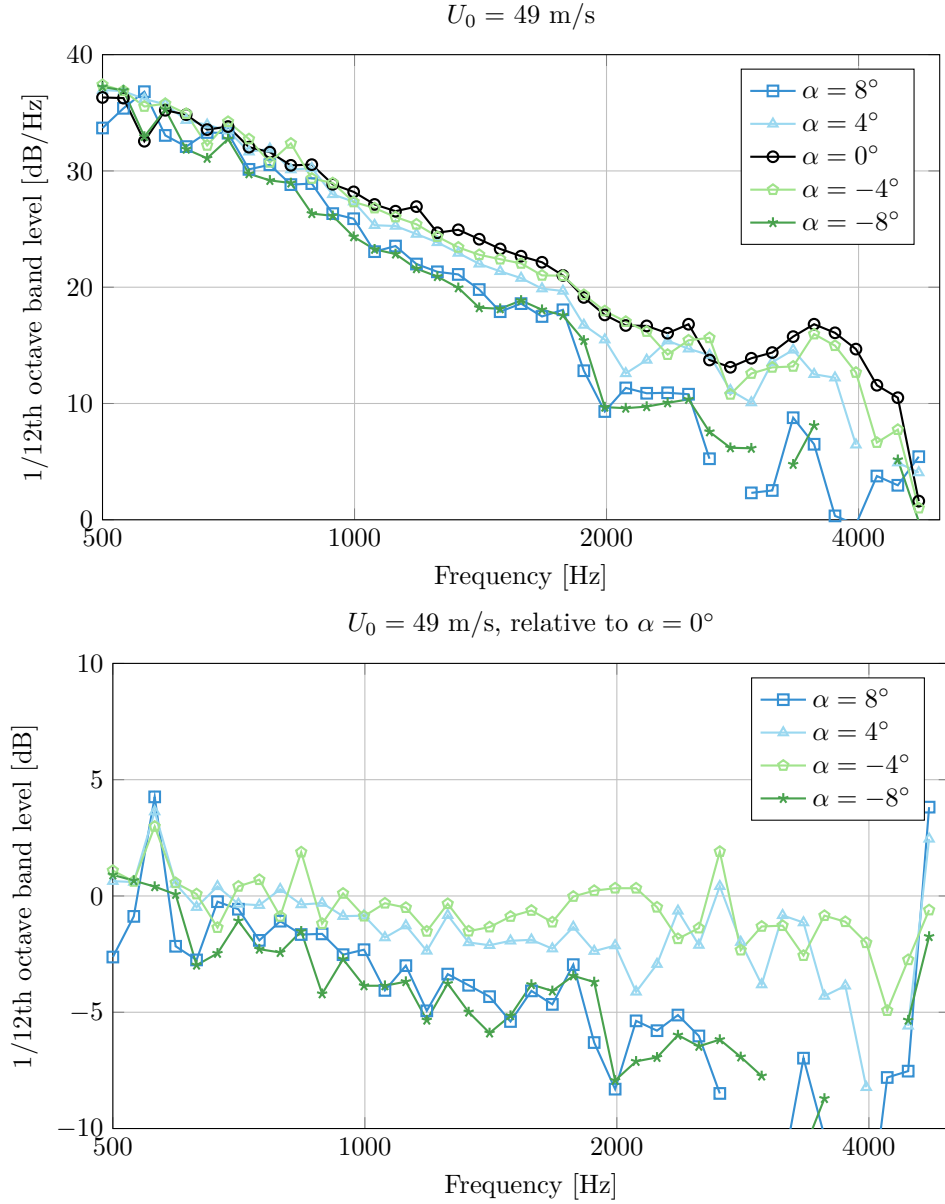


Figure 5.16: NACA63018 at Re 3 mio for angles of attack -8,-4,4,8. Bottom: Level difference relative to zero angle of attack $SPL_\alpha - SPL_0$.

Re 2 mio, zero angle of attack

At Reynolds number 2 mio and at zero angle of attack, the beamforming maps are shown in Fig. 5.18. A clear trailing edge source is seen in a large frequency range. The peak from the pitot tube is seen at 1000 Hz but it is not dominating as it was the case at Reynolds number 3 mio. Source integration results, following the same procedure as above, are shown in Fig. 5.17. A good agreement between methods are seen from 500 Hz to 3000 Hz. The broad hump above 2000 Hz is related to bluntness noise. A small disagreement is seen towards 4000 Hz where the noise emission of the airfoil is quite low. The difference is likely artifacts from the background noise. The acoustic source maps are shown in Fig. 5.19. All methods provide a visible trailing edge source.

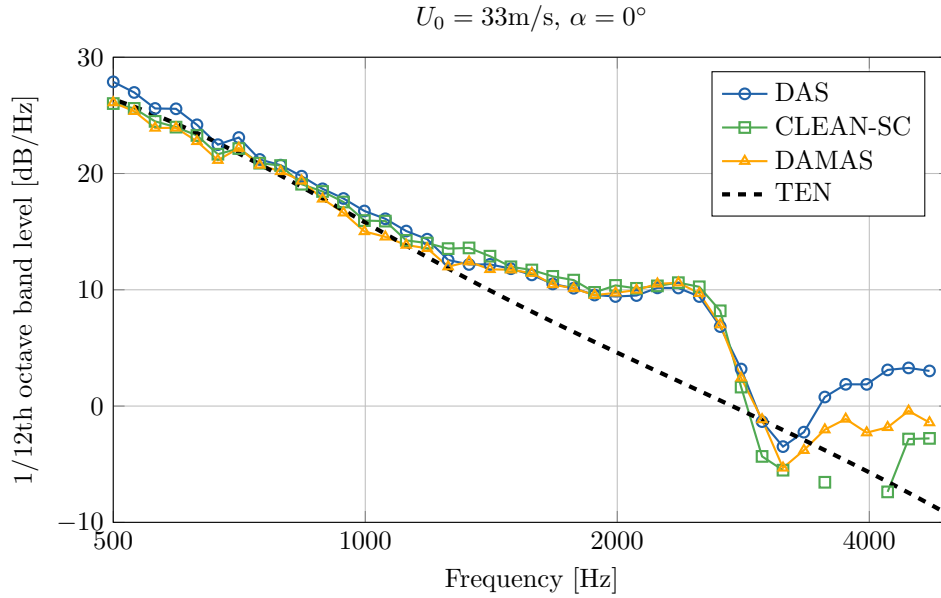


Figure 5.17: Comparison of algorithms for noise quantification on a NACA63018 airfoil

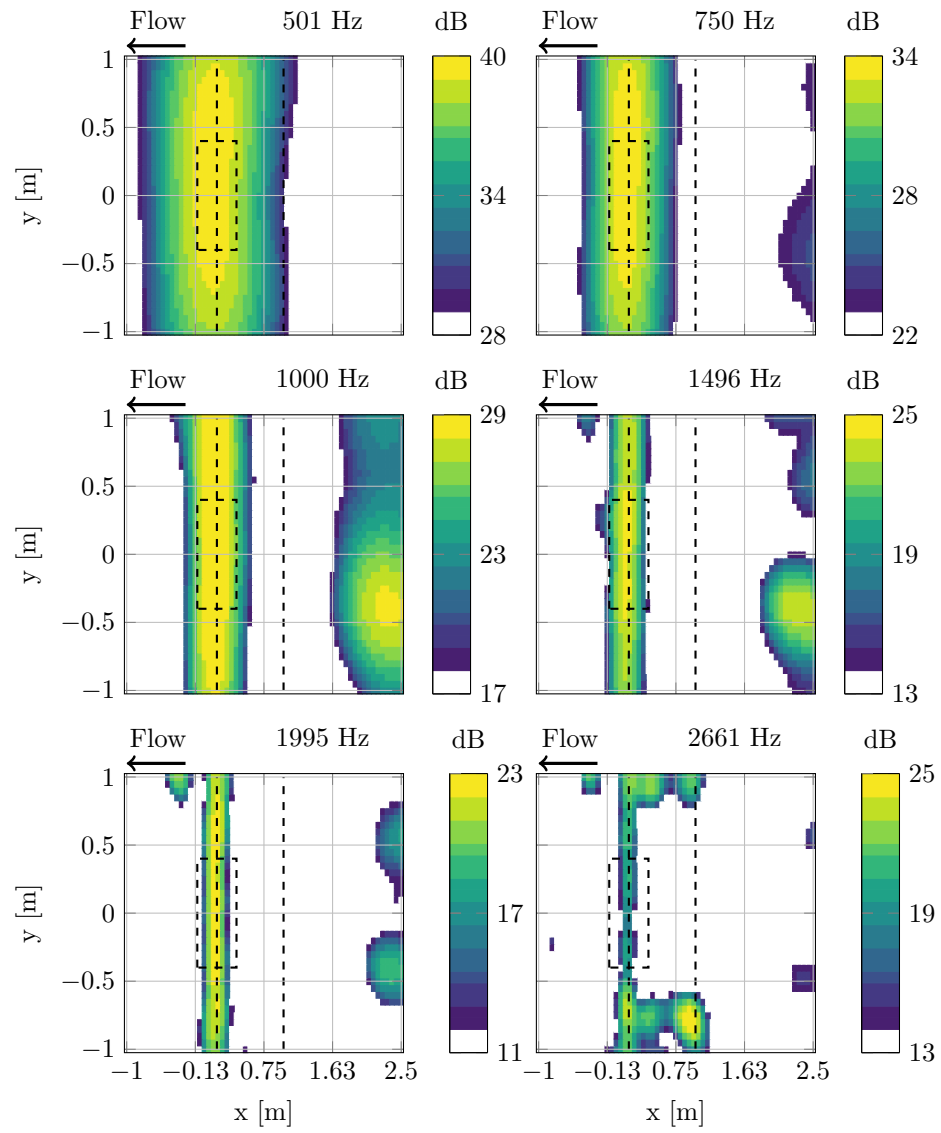


Figure 5.18: Beamforming maps of NACA63018 airfoil

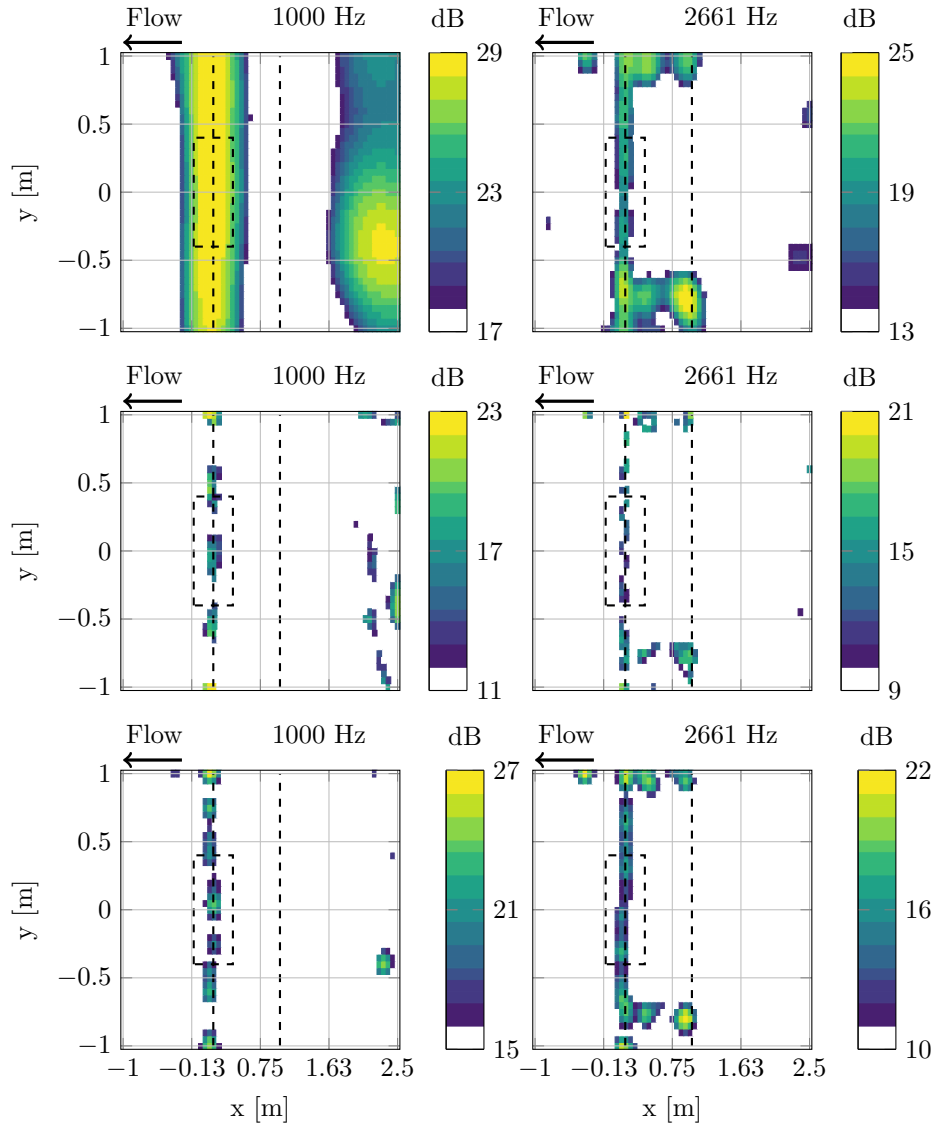


Figure 5.19: Comparison of algorithms for noise quantification on a NACA63018 airfoil. From top to bottom: Beamforming, DAMAS, and CLEAN-SC.

Re 4 mio, zero angle of attack

At Reynolds number 4 mio and at zero angle of attack, the beamforming maps are shown in Fig. 5.21. A positive SNR ensures a clear trailing edge noise source in the low frequencies. At 1995 Hz and 2661 Hz, the pitot tube source is visible, and obscuring at the trailing edge at 2661 Hz. The CLEAN-SC algorithm is again used to remove the dominant source, which can be seen in effect in the integrated spectra in Fig. 5.20. Level increases of up to 10 dB is observed with DAS and DAMAS due to the dominant source. The peak removal technique of CLEAN-SC is very beneficial here. However, some peaks are still visible. This can be tuned by hand, by removing more than just the first dominant source, as it was done for Reynolds number 3 mio above. Since the method does not have an objective criterion for choosing how many dominant sources to remove, there is a risk of fitting data. Acoustic source maps are shown in Fig. 5.22. At 2661 Hz, only CLEAN-SC is capable of resolve the source, but several artifacts are still present in the map. At 3548 Hz, all methods are capable of resolving the source.

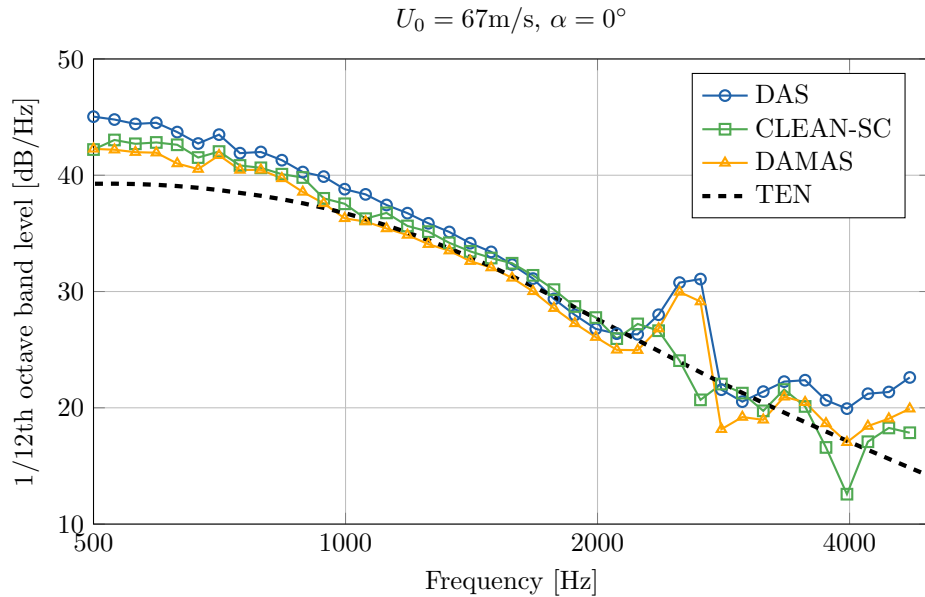


Figure 5.20: Comparison of algorithms for noise quantification on a NACA63018 airfoil

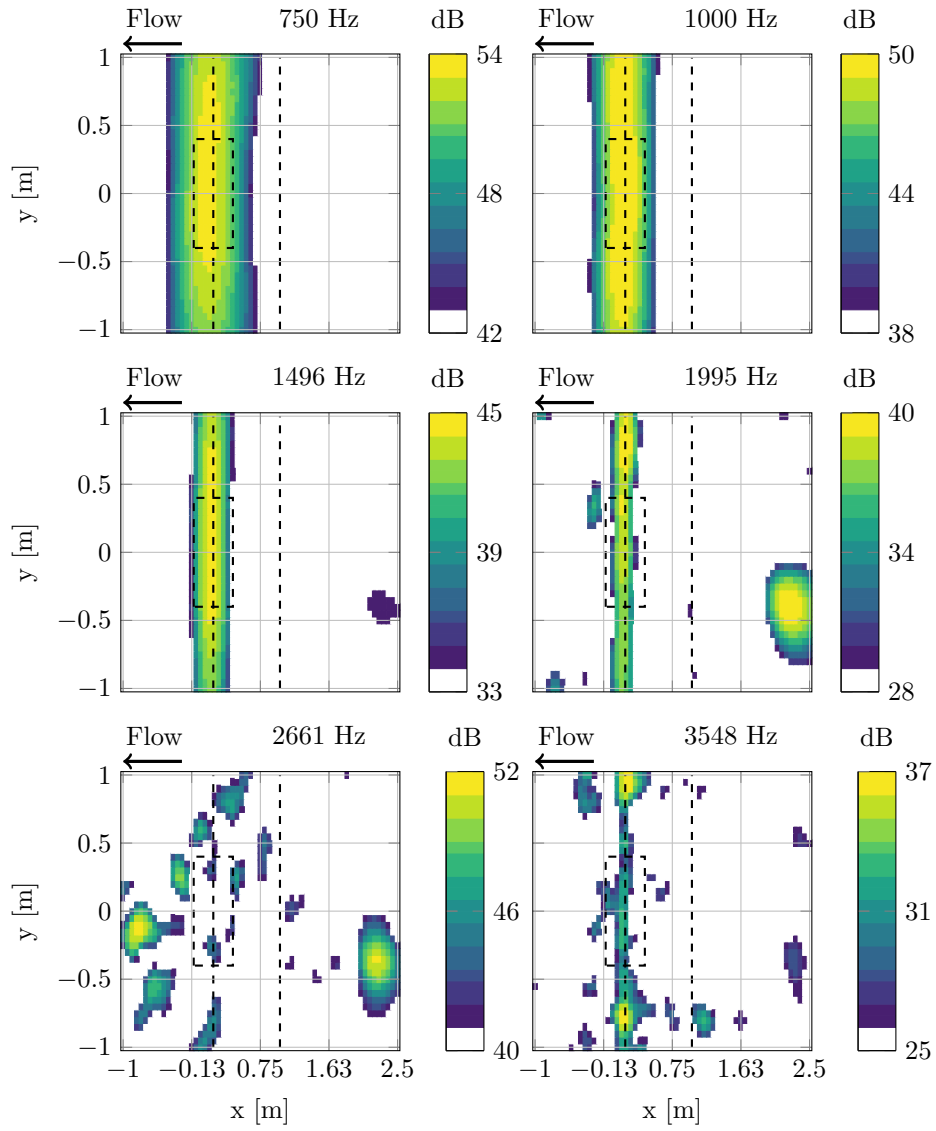


Figure 5.21: Beamforming maps of NACA63018 airfoil

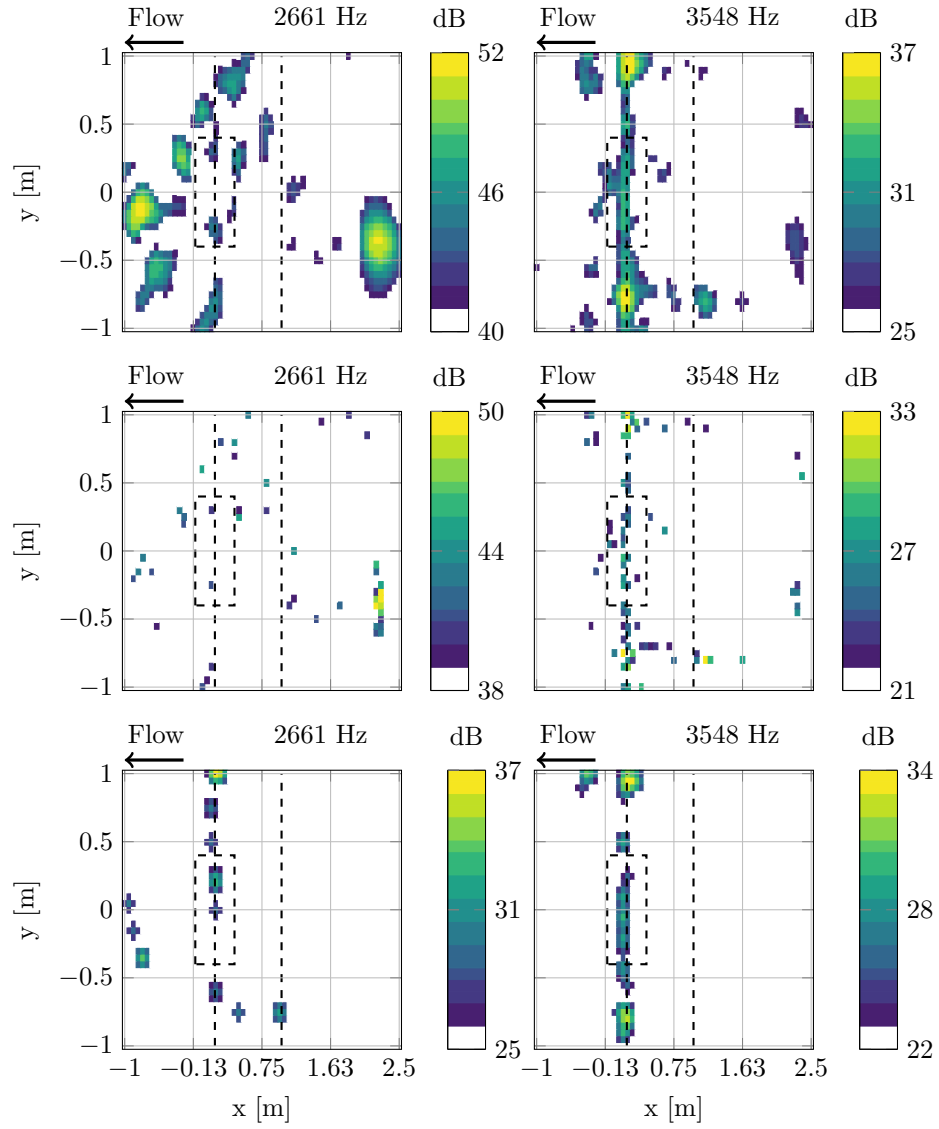


Figure 5.22: Comparison of algorithms for noise quantification on a NACA63018 airfoil. From top to bottom: Beamforming, DAMAS, and CLEAN-SC.

Strouhal scaling

The source integration results, shown above, are compared at zero angle of attack in a Strouhal number plot with a Mach number scaling. The boundary layer thickness is used as a reference length in the Strouhal number. In Fig. 5.23, it is seen, that three curves collapse using a Ma^5 scaling. Additionally, the broad hump, that was visible at Reynolds number 2 mio and 3 mio also collapse, indicating that it was indeed trailing edge bluntness that caused it.

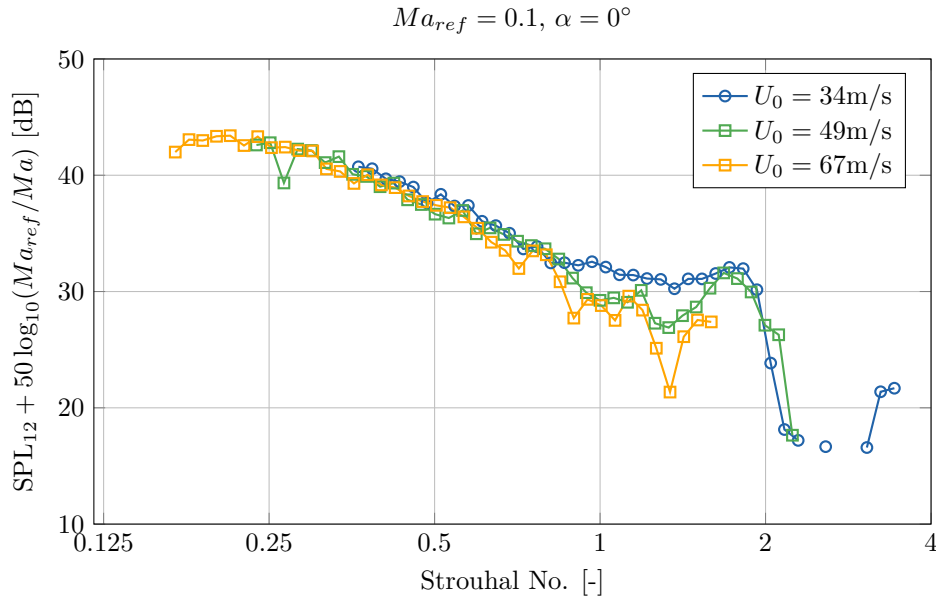


Figure 5.23: Strouhal number scaling of source integration spectra using CLEAN-SC.

5.4 Conclusion

The NACA63018 was used as a reference airfoil to test methods for estimating trailing edge noise. The results were compared to a trailing edge noise model. The model did not take into account bluntness noise, but a Strouhal plot showed, that this is in fact the case. Additionally, the results scale with Ma^5 . Both DAS, DAMAS and CLEAN-SC was found to provide reliable results, and where the pitot peak affected the spectra, the removal of dominant sources was applied successfully using CLEAN-SC. In future wind tunnel campaigns it is suggested to reduce vortex shedding of the pitot tube or remove it completely. Even if the pitot tube is removed completely, the method of dominant source removal is still applicable in cases with, e.g., junction noise or other distinct sources.

Chapter 6

Concluding remarks

The overall goal of this PhD study has been to investigate methods for quantifying noise from wind turbine blade sections in a wind tunnel. To achieve this, the measurement conditions and sound propagation properties have been examined. Revisiting the objectives from the Introduction:

- Validate the acoustic design of the Poul la Cour Tunnel through simulations and measurements.
- Implement and develop signal processing techniques for microphone array measurements specific to the conditions in the Poul la Cour Tunnel. Taking into account the background noise, losses introduced by the Kevlar walls and corrections related to the aerodynamic properties of the flow.
- Setup and validate aeroacoustic measurements.
- Implement and develop methods for quantification of trailing edge noise.

In Chapter 2, the design of the Poul la Cour Tunnel was described and the background noise level was found to scale with $Ma^{5.5}$. In Paper A, the acoustic design validation of PLCT was conducted using a methodology based on impulse responses. The transmission loss of the acoustic absorbers was estimated in-situ and compared to a numerical model, finding good agreement in the frequency range 1000 Hz to 5000 Hz. This concludes the first objective.

In Chapter 3, common microphone array techniques, such as delay-and-sum beamforming, diagonal removal, source power integration, and deconvolution and inverse methods, were reviewed. Additionally, performance metrics, resolution, and applicable frequency ranges of the microphone array setup at PLCT were introduced and discussed. In Paper B, effects of boundary conditions and regularization on a deconvolution algorithm, were investigated. It was found that the solution is very sensitive to the regularization parameter and that a parameter estimation method is needed to provide reliable

results. The acoustic loss due to Kevlar and turbulent boundary layer was examined in Chapter 4 and Paper C. The Kevlar loss was determined with three different methods and a general trend was found. The results were compared to existing literature, finding good agreement in the frequency dependency, but higher losses were found in this study. The TBL loss was examined in Paper C. Using a reference source with known sound power level, the acoustic loss through two Kevlar walls was estimated at six different flow speeds by source integration of beamforming maps. The TBL loss was found to scale linearly with Mach number in the frequency range 1000 Hz to 4000 Hz, and a curve fit was determined. A comparison of the TBL loss estimated at similar facilities showed large variations in results, indicating a need for more research on this topic. This concludes the second objective of this PhD study.

The last two objectives of this PhD study were examined in Chapter 5, where measurements of a NACA63018 airfoil was conducted in PLCT. Noise quantification of the trailing edge noise was performed with DAS beamforming, DAMAS and CLEAN-SC, and found to provide reliable results. A pitot tube, situated in the contraction, has been a returning issue in many of the measurements presented. The method of dominant source removal with CLEAN-SC was investigated and found to be able to remove the pitot tube source from the acoustic maps and remedy source integration results. A trailing edge noise model was used as a reference for the implemented methods and found to agree well in a wide frequency range. A lack of agreement was seen below 750 Hz and above 3000 Hz-4000 Hz, depending on flow speed, and for bluntness noise, which was not accounted for in the model. Overall, the three methods performed reliably and a Mach number scaling of Ma^5 was found. The numerical implementation of methods for post-processing and noise quantification has been collected in the open source library AeroAcoustics.jl [86].

Future research questions for the Kevlar-walled wind tunnel, that have emerged from the results of the this PhD study, are:

- How can structural vibrations of Kevlar be measured consistently across facilities, how does it change with pre-tension, and what is its relation to Kevlar and turbulent boundary layer losses?
- How can the turbulent boundary layer thickness on the Kevlar wall be measured consistently across facilities, and what is its relation to the turbulent boundary layer loss?
- Which analytical models exist for describing Kevlar insertion loss, and how can effects of flow and source directivity be incorporated?
- What are the uncertainties in estimating trailing edge noise with microphone array methods, and how can uncertainty quantification be integrated into the post-processing tool chain?

- CLEAN-SC is capable of removing dominant sources in the acoustic source maps. How can an automatic method for removal of sources outside a predefined area be implemented numerically?

In general terms, this PhD study has provided a validation of the acoustic setup in PLCT for determination of trailing edge noise spectra. However, the contributions reach further than just PLCT. The experimental in-situ method for estimation of transmission loss, described in Paper A, could be applied at other facilities where acoustic absorbers are installed. In Paper B, a simulation study indicated that the low frequency limit of beamforming could be decreased by using an extended domain as boundary condition. The method proposed in Paper C, for estimation of TBL loss, and associated refraction correction for two shear layers, can be applied at other research facilities, providing a general applicable methodology.

Paper A

Submitted for publication.

Acoustic Design Validation of an Anechoic Wind Tunnel

Oliver Lylloff^{*1}, Andreas Fischer¹, Christian Bak¹, and Efren Fernandez Grande²

¹DTU Wind Energy
Technical University of Denmark (DTU)
Frederiksborgvej 399
DK-4000 Roskilde, Denmark.
²DTU Electrical Engineering
Technical University of Denmark (DTU)
Ørstedes Plads
DK-2800 Kongens Lyngby, Denmark.

November 14, 2020

Abstract

This paper presents the acoustic design of a new anechoic wind tunnel and describes an experimental method for its validation. A methodology is presented to estimate in-situ the individual transmission losses of the acoustically treated fan, guide vanes and diffuser, at zero flow. The experimental results are compared to a finite element simulation, that was conducted prior to construction of the wind tunnel. The results show, that the presented methodology enables the validation of the wind tunnel design in 1/3 octave bands in the range from 1000 Hz to 5000 Hz, and in some cases down to 250 Hz. The experimental method shows promise of being generally applicable for the validation of the acoustic design of wind tunnels.

1 Introduction

Wind tunnel facilities dedicated to aeroacoustic testing have been in operation for many years. These tunnels are frequently used by the automotive and aerospace industry as well as national research institutions [1, 2, 3, 4, 5]. Several university-owned wind tunnels have also been put into operation over the last decade [6, 7, 8, 9, 10, 11, 12]. The common purpose of these tunnels is to study noise generated by the flow of air passing over various objects in a controlled environment, both from an acoustic as well as an aerodynamic standpoint.

The present paper is focused on the acoustic design of the newly-commissioned Poul la Cour Tunnel (PLCT), situated at the Wind Energy Department of the Technical University of

^{*}Corresponding Author: OLLYL@DTU.DK

Denmark, which is an anechoic wind tunnel dedicated to wind energy research. A finite element simulation was performed prior to construction to evaluate and assess the design criteria of the wind tunnel. The numerical results were presented in [9] and this study investigates an experimental in-situ method for the validation of these.

Common for all wind tunnels dedicated to acoustic testing is that a low background noise level is required. The flow itself is typically generated by a fan (placed far from the test section) and guided through the airline circuit to the test section, where the object under test is studied with acoustic equipment. One of the main contributions to the background noise in the tunnel is the fan itself. Thus, much effort has gone into the study of fan noise and attenuation strategies; one common strategy is to integrate acoustic absorbers (also called silencers) in the airline circuit [13, 14, 15]. In Ref. [13] one of the first discussions on fan noise reduction in a wind tunnel is given. Later, Soderman et al. studied fan noise reduction in a wind tunnel with a specific focus on the acoustic behavior of turning vanes (or guide vanes) [14]. Further, in Ref. [15] a comprehensive overview of acoustic treatment options for a wind tunnel was given, that includes: Non-intrusive liners, splitters, baffles, and treated turning vanes. In an attempt to determine reverberation times the authors used an impulsive sound source, however, due to non-conclusive results, a scale-model experiment was used instead to estimate reverberation times. Recent studies of acoustic wind tunnels [6, 11] used a combination theoretical predictions and silencer manufacturer calculations to validate the acoustic design. In addition to that, Chong et al., measured the transmission loss of the primary silencer using an sound intensity probe [7].

Two common performance measures used to assess the properties of silencers are the transmission loss and insertion loss. The transmission loss of a silencer is defined as the difference in incident and transmitted power level with an anechoic termination, whereas the insertion loss is defined as the difference in acoustic power level with and without the silencer inserted [16]. In 1955 Raes described the use of impulse responses to obtain the transmission loss of building partitions in-situ [17]. More recently, in Ref. [18], road noise barriers were studied and an experimental in-situ method for the determination of transmission loss was presented. A non-periodic excitation signal was used to obtain a transfer function between two microphones on either side of the barrier. The experimental results were compared to laboratory measurements, showing good agreement [18]. In the present study, a similar approach is taken. Specifically, the use of a non-periodic excitation signal to obtain transfer functions, and furthermore, the design of a window to time-gate the transfer functions. However, the wind tunnel environment in which the measurements are conducted (a concrete duct), requires other considerations than that of the free-field assumption that could be applied Ref. [18].

With the practical issues described above, in the early studies of wind tunnels, and the common use of numerical techniques in more recent works, the need for an experimental in-situ validation method has arisen. One such method is proposed and examined in the present paper. With inspiration from [17, 18], the objective of this work is to derive an experimental in-situ method for the validation of the numerically simulated transmission loss found in [9]. The approach taken, is to analyze impulse responses captured before and after a silencer and from that estimate transmission losses. The experimental estimation is carried out in the Poul la Cour Tunnel without flow.

The paper is structured as follows. First, in Section 2, an overview of the wind tunnel and the acoustic design is presented. In Section 3, the experimental method is described. The numerical results of the study in Ref. [9] is summarized in Section 3.5 with additional results of the present paper. Experimental and numerical results are compared in Section 4 and discussed in Section 5. Finally, conclusions are given in Section 6.

2 Wind tunnel overview and design

This study is conducted in the Poul La Cour Tunnel (PLCT) situated at the Wind Energy Department of the Technical University of Denmark, which has a closed loop airline, shown in Figure 1 with individual elements summarized in Table 1.

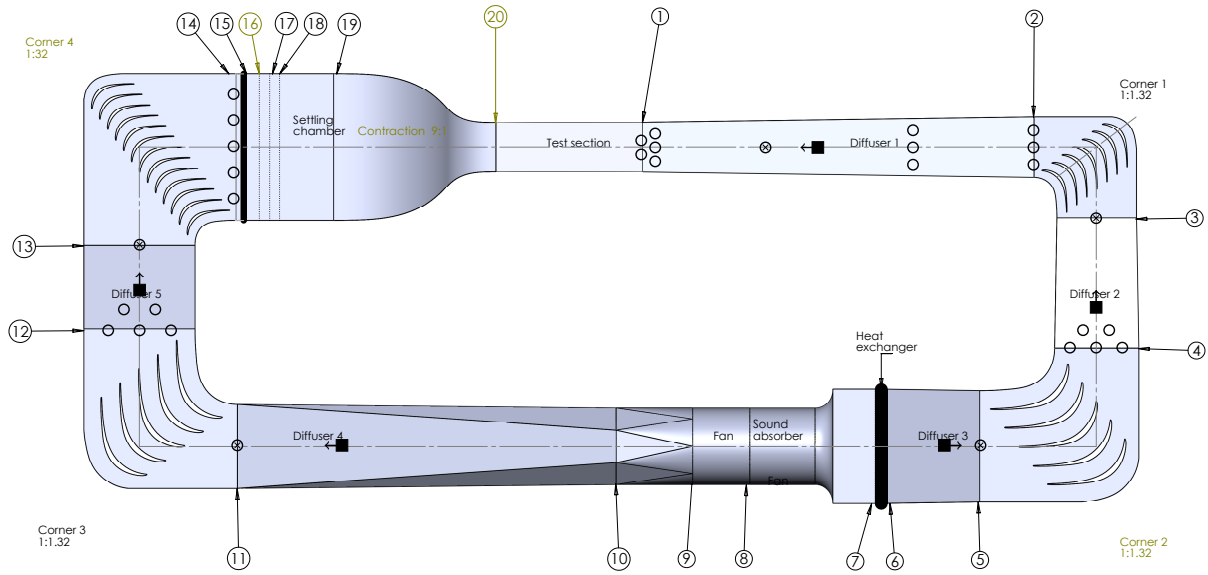


Figure 1: The Poul la Cour Tunnel. Position of loudspeaker (■) and microphones at inlet (⊗) and outlet (○) of silencer for 5 measurement campaigns. Flow direction is in clockwise direction. Adapted from [9].

Table 1: Elements of PLCT

1-2	Diffuser 1	6-7	Heat exchanger	10-11	Diffuser 4	14-19	Settling chamber
2-3	Corner 1 guide vanes	7-8	Fan silencer	11-12	Corner 3 guide vanes	19-20	Contraction
3-4	Diffuser 2	8-9	Fan	12-13	Diffuser 5	20-1	Test section
4-5	Corner 2 guide vanes	9-10	Fan silencer	13-14	Corner 4 guide vanes		

The flow is driven by a 2.4 MW fan and a maximum speed of 105 m/s can be achieved. The test section has a cross section of 2×3 m and is 9 m long. The walls of the test section can be exchanged between aerodynamic hard walls and aero-acoustic Kevlar walls. The Kevlar walls are 6 m long and cover the part of the test section which begins 1 m downstream of the contraction. The test section is surrounded by an anechoic chamber. The acoustic field in the anechoic

chamber was tested according to ISO 3745 [19]. It is close to an ideal free field above frequencies of 125 Hz. However, in the frequency range between 200 Hz and 3150 Hz the deviation from ideal free field conditions is ± 2 dB which is slightly higher than allowed according to ISO 3745.

2.1 Silencer design

Three components of the acoustic design is described briefly here; the fan silencer, guide vanes, and diffuser. For additional details, the reader is referred to [9].

Common to the three silencer designs is a porous type absorber with mineral wool covered by a perforated steel plate. The thickness of the porous material is $d_{abs} = 0.4$ m (in the corners limited to the thickness of the guide vanes) and the thickness of the perforated plate is $d_{panel} = 1$ mm with a hole radius of $a = 0.6$ mm and an open area ratio of $\eta = 33\%$. The flow resistivity of the chosen mineral wool is $\sigma = 10000 \text{ N s m}^{-4}$. With these material properties, the absorption coefficient is calculated using a transfer matrix method [20, chap. 6] for a perforated plate with porous absorption and rigid backing, shown schematically in Figure 2. The absorption coefficients for normal incidence and random incidence, calculated assuming a locally reacting surface, are given in Table 2.

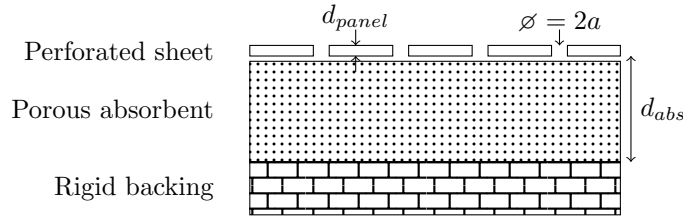


Figure 2: Helmholtz absorber model for silencers. Adapted from [20].

f [Hz]	63	125	250	500	1000	2000	4000
α_{θ}	0.65	0.76	0.85	0.90	0.92	0.93	0.92
α_{\perp}	0.51	0.64	0.79	0.90	0.96	0.99	0.99

Table 2: Absorption coefficients for random incidence (α_{θ}) and normal incidence (α_{\perp}) of porous type absorber in 1/1 octave bands.

At the fan, porous absorbers are placed in the walls surrounding the fan, and in the nose and tail cone. The fan silencer is designed to attenuate noise from the fan blade passing frequency and its first harmonics, approximately below 300 Hz. In the diffuser, just downstream of the test section, absorbing panels are installed in walls and ceiling to reduce background noise from the fan. The design of the guide vanes is based on a parallel baffle model and the distance between successive guide vanes is chosen to obtain a peak absorption at $f = c/2h$, where c is the speed of sound and $2h$ is the distance between two guide vanes. In corners 1 and 4 (see Fig. 1), $2h = 0.6$ m, and in corners 2 and 3, $2h = 1.1$ m, which gives a peak absorption of the parallel baffles at 570 Hz

and 310 Hz, respectively. The flow resistivity of the porous absorbing material was chosen to obtain high absorption at these peak frequencies. The length of each guide vane was chosen to limit direct propagation by high frequencies using a ray-geometric consideration.

3 Methods

The wind tunnel airline is considered to be a rigid-walled duct with several individual silencers inserted at separated locations. The duct is assumed to be infinite in the axis along the duct (z direction). In the frequency domain, the pressure field in the duct can be described by the Helmholtz equation.

The analytical solution to the Helmholtz equation in a three-dimensional duct (infinite along z -axis) with rigid wall boundary conditions is described by the modal shape functions [21],

$$\Psi_{m,n}(x, y, z) = \sqrt{\epsilon_m \epsilon_n} \cos\left(\frac{m\pi}{L_x} x\right) \cos\left(\frac{n\pi}{L_y} y\right) \quad (1)$$

where $\epsilon_{m,n} = 1$ for $m = n = 0$ and $\epsilon_{m,n} = 2$ for $m, n > 0$ and L_x and L_y are dimensions of duct. At $m = n = 0$, the fundamental mode, only plane wave propagation exists along the z -axis. For higher order modes, $(m, n) \neq (0, 0)$, the mode shapes have corresponding eigenfrequencies $f_{m,n} = c/2\sqrt{(m/L_x)^2 + (n/L_y)^2}$ [21]. Consequently, below the cut-off frequency, $f_c = c/L$, a free-field wave propagation along the duct axis is often assumed [16]. Above the cut-off frequency, modal patterns dominate the sound field. The modal density, that is, the number of modes per frequency, is a quadratic function of frequency [22]. At a sufficiently high modal overlap, the sound field can be considered diffuse [23]. Nélisse et al. further derived a heuristic for the cut-off frequency in 1/3 octave bands: 6 modes (in 2D) and 20-30 (in 3D) per 1/3 octave band [24].

3.1 Transfer function measurement

The acoustic transfer function between two microphones can be determined as the ratio of their respective frequency spectra [22]. In rooms and large spaces, the transfer function between two points is typically obtained through the Fourier-transformed ratio of impulse responses. The use of non-periodic sweeps to obtain impulse responses is a widely used technique in acoustics [22]. In mathematical terms, the output $y(t)$ of a linear time-invariant system can be described as a convolution of the input $x(t)$ with the system's impulse response $h(t)$. The impulse response $h(t)$ can be obtained from $y(t)$ by construction of an inverse filter $f(t)$ that can fold the input signal $x(t)$ into a Dirac delta function, $x(t) * f(t) \Rightarrow \delta(t)$, such that, $h(t) = y(t) * f(t)$, where $*$ is the convolution operator [22]. To reduce variability, several sweeps can be averaged (or longer sweeps can be used). Let $x_i(t)$ be the reference signal of the i 'th sweep, $y_{i,j}(t)$ the measured signal of the i 'th sweep at the j 'th position, then, the averaged impulse response is

$$h_j(t) = \frac{1}{N} \sum_i^N \mathcal{F}^{-1} \left(\frac{\mathcal{F}(y_{i,j})}{\mathcal{F}(x_i)} \right), \quad (2)$$

where N is the number of sweeps, $\mathcal{F}(\cdot)$ is the Fourier Transform and $\mathcal{F}^{-1}(\cdot)$ its inverse. In this study, the transmission loss (TL) is estimated from the ratio of impulse responses obtained with two microphones, one at the inlet of an acoustic absorber and one at the outlet. The averaged impulse responses, $h_{1,j}(t)$ and $h_{2,j}(t)$ of the two microphones, respectively, are time-gated and compared in 1/3 octave bands to yield the final result,

$$TL_j = 10 \cdot \log_{10} \left(\frac{P_{1,j}}{P_{2,j}} \right), \quad (3)$$

where $P_{1,j}$ and $P_{2,j}$ are 1/3 octave band spectra of $h_{1,j}(t)$ and $h_{2,j}(t)$ respectively. The results shown in Sec. 4 are given as the mean and standard deviation over j of all TL_j .

3.2 Window function

To time-gate impulse responses, a window function is constructed with inspiration from Ref. [18]. The window function is constructed by the left half of a Blackman-Harris window of total length 2.5 ms, a flat part of length 100 ms, and the right half of another Blackman-Harris window of total length 2.10 ms. The window is positioned such that the flat part begins 5 ms before the impulse response peak. The window design used in Ref. [18] is constructed from a free-field assumption. Specifically, the flat part of their window is designed to time-gate the response to the transmitted part of the impulse response, thereby avoiding the diffracted part. The situation is quite different in a wind tunnel duct, where the reverberant space and complex geometries makes it more difficult to separate transmission from diffraction. Experimentation has shown, that a window length of 100 ms captures a sufficient amount of initial transmitted energy (and some early reflections) while minimizing the influence of the long reverberation times in the airline duct. In Fig. 3, a logarithmic sweep, pressure time history and a time-gated impulse response is shown.

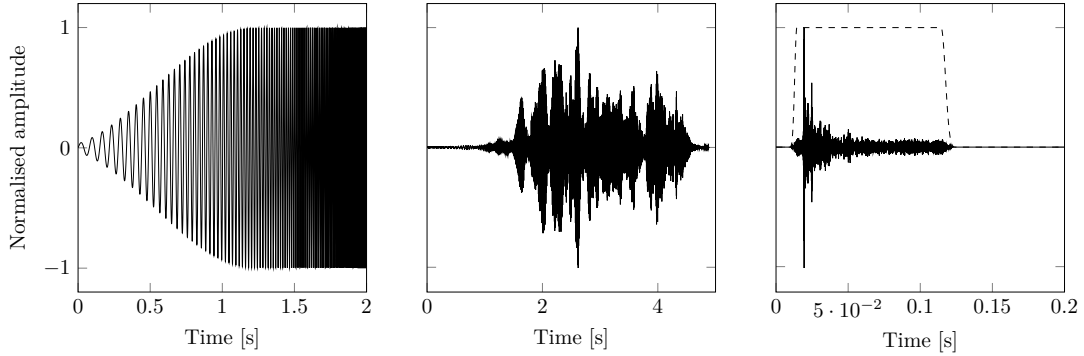


Figure 3: Left: Excitation signal (logarithmic sweep), Middle: Raw recording from inlet of absorber, Right: Impulse response with window function applied (dashed line is window).

3.3 Experimental setup

The experimental estimation of transmission losses was conducted in a wind tunnel airline at zero flow over 4 days in October 2019. The equipment consisted of a loudspeaker (B&K Omnisource Type 4295), two microphones (GRAS 1/2" free-field type 146AE), an amplifier (B&K type 2734), a PC to generate excitation signals at a sampling rate of 48 kHz, and a PC connected to a data acquisition system (B&K type 3050-A-060). At each measurement location (4 corners with guide vanes and the diffuser), the loudspeaker was placed in the direction of sound propagation from the fan into the absorber in question at a fixed distance (5 to 8 meters). Positions are shown in Fig. 1 and pictures of setup in Fig. 4. Microphone 1 was placed at the inlet of the absorber, in the horizontal center of the duct, and microphone 2 at the outlet. Measurements were taken at 5 different positions behind the outlet to get a rough spatial average. Each measurement consisted of 8 10s logarithmic sine-sweeps to reduce variability, which resulted in impulse responses averaged over 40 sweeps in total. Impulse responses at inlet and outlet were low-pass filtered with a cut-off frequency of 20 kHz and time-gated by applying the window function described in Sec. 3.1. One-third octave band spectra were determined and the transmission loss computed from Eq. (3).



Figure 4: Experimental setup at corner guide vanes. At inlet of corner (top image), a loud-speaker is pointing into the corner at a distance of approximately 5 to 8 meter. Just in front of the corner, a microphone is placed. At the outlet (bottom image), a microphone is positioned at 5 different locations to get a rough spatial average.

At the guide vane corners the rigid duct wall pose a limitation to the lower frequency range of the measurements. The distance from wall to microphone L_{mic} should be larger than half a wavelength to avoid bias due to wall interference, corresponding to a lower frequency cut-off $f_{\text{min}} = c/(2L_{\text{mic}})$. This is most relevant to the measurement near the guide vanes, where walls, floor and ceiling are rigid. At the diffuser, microphones were placed near absorbing panels in walls and ceiling and only the floor was rigid. The cut-off frequency associated with diffuseness is approximated by the number of modes per 1/3 octave band in a 2D enclosure (width and height of duct) at each measurement position. The lowest 1/3 octave band with 6 or more modes is taken as the cut-off frequency [24]. The cut-off frequencies for the corner measurements are summarized in Table 3.

Corner	(W x H) [m]	$L_{\text{min,mic}}$ [m]	$f_{\text{c,mic}}$ [Hz]	$f_{\text{c,diffuse}}$ [Hz]
1	4.8 x 6.25	0.8	250	160
2	5.2 x 9.4	1.2	200	125
3	5.2 x 9.4	1.6	125	125
4	4.8 x 6.25	1.6	125	125

Table 3: Cut-off frequencies due to boundary interference ($f_{\text{c,mic}}$) and diffuseness ($f_{\text{c,diffuse}}$).

To assess whether a free-field assumption is applicable, measurements were taken upstream and downstream of corner 1, in straight tunnel sections without absorbing material. The duct cross-sectional area decreases from 22 m² to 18 m² downstream of corner 1 (in upstream direction) and from 14 m² to 10 m² upstream (in upstream direction). The overall sound pressure levels were taken at increasing distances to a loudspeaker excited by a 10 s swept-sine signal (with 4 averages at each position). Figure 5 shows a log-log plot of the sound decay as function distance to loudspeaker. The results indicate that a free-field assumption is not valid, as the measurements would have followed a straight line in Figure 5. Therefore it is necessary to take into account the boundary reflections and reverberation, and it becomes relevant to assess the power flow through the tunnel – a methodology that is presented in the following section.

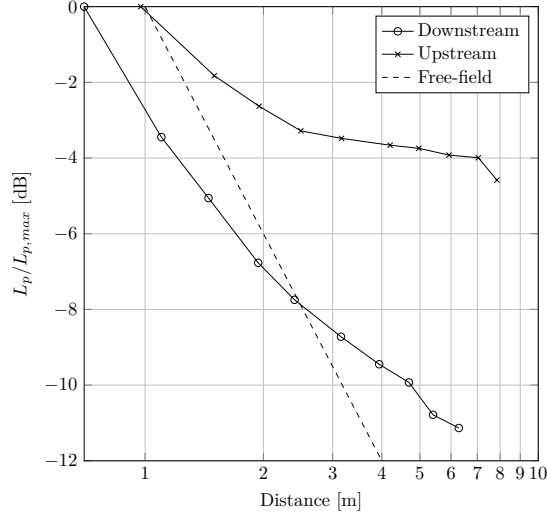


Figure 5: Measurements of sound decay as function of distance downstream and upstream of Corner 1.

3.4 Fan silencer

The methodology used for the corner TL above is not applicable to the fan's silencer, as the sound field changes rapidly in space and obtaining a spatially averaged quantity is not straightforward. An alternative approach (denoted a power-flow method) has been adopted, where a sound power reference source is used to examine the sound power that is effectively dissipated at the fan's silencer. The sound power reference source (B&K type 4204) was placed at the fan and at several other locations around the airline (see Fig. 7), while the transmission loss was measured in the test section with two microphones (GRAS 1/2" free-field type 146AE), positioned at the inlet and outlet (number 20 and 1 in Fig. 1). Using the transmission loss at each of the measurement positions, the transmission loss of the fan silencer, measured in upstream and downstream directions, was determined. In Ref. [25] Beissner suggests that a plane-wave approximation is fair at distances far from source. This was the assumption made in the finite element model [9] and it was seen to be consistent with the measurements of the guide vanes. Consequently, the estimation of the transmission loss of the fan silencer is calculated from the sound power reference level of the source assuming a plane wave propagation and considering the intensity to be constant over a plane moving along the duct axis (from inlet I_{in} to outlet I_{out}),

$$I_{in} = \frac{P}{A_{in}}, \quad I_{out} = \frac{p^2}{\rho c}, \quad TL = 10 \cdot \log_{10} \frac{I_{in}}{I_{out}}, \quad (4)$$

where P is the reference sound power, A_{in} is the duct cross-section at a specified position, p^2 is the squared sound pressure of the microphones in the test section, and ρ is the density of air.

The downstream transmission loss was estimated as follows. The sound power reference source was first placed at the inlet of corner 3 (Pos 1 in Fig. 7) to measure the total transmission loss of corner 3, 4 and contraction, here denoted as TL_{pos1} . Then, the sound power reference

source was moved to the fan (Pos 2 in Fig. 7) and the total transmission loss of fan, corner 3, 4 and contraction, TL_{pos_2} , was measured (using the same reference area A_{in} as position 3). Finally, the transmission loss of the fan was estimated by the difference between measurements at position 1 and 2 $TL_{fan,down} = TL_{pos_2} - TL_{pos_1}$. The upstream transmission loss was estimated in a similar manner, by taking the difference between measurements at position 3 (Pos 3 in Fig. 7) and position 2 $TL_{fan,up} = TL_{pos_2} - TL_{pos_3}$.

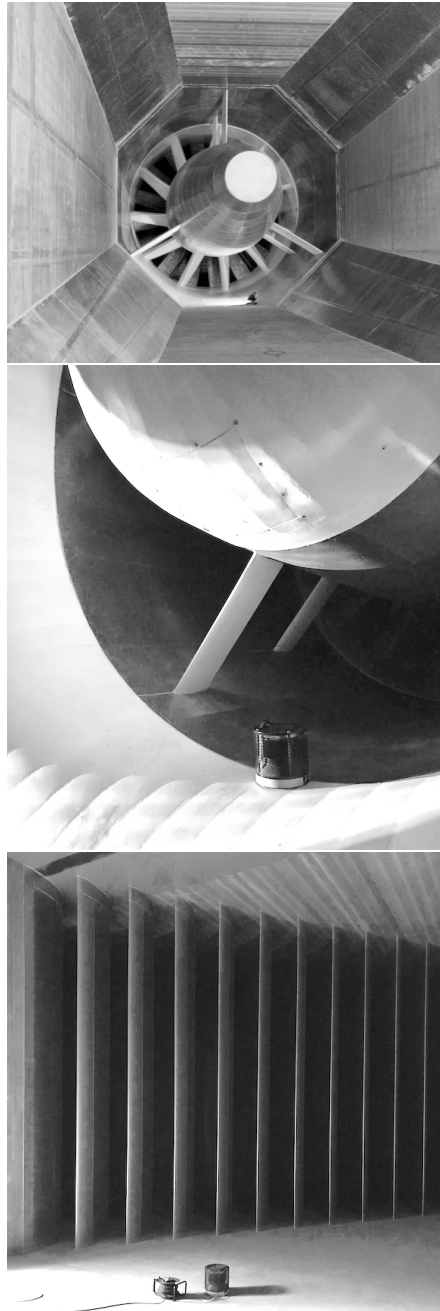


Figure 6: Experimental setup for fan silencer. Top image shows perforated panels with absorbing material in the walls surrounding the fan and tail cone of the fan itself. Middle and bottom images show a sound power reference source placed near the fan's nose cone (middle image) and at the corners (bottom image) to assess the transmission loss of the fan silencer.

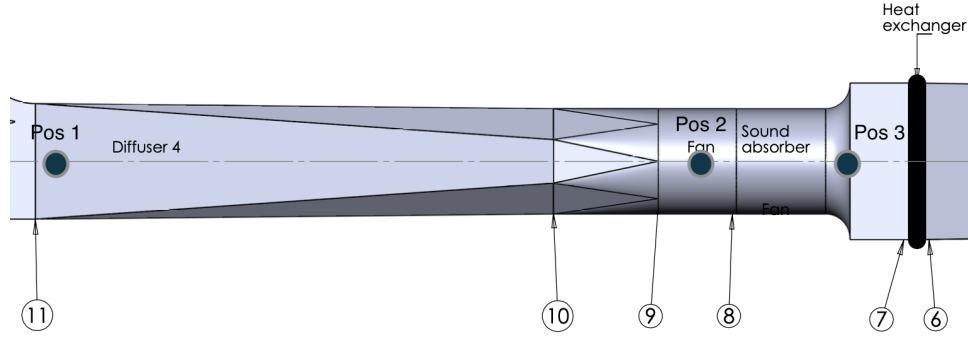


Figure 7: Experimental setup for estimating transmission loss of fan silencer. Positions (1, 2, and 3) of sound power reference source placements are shown in black markers.

3.5 Numerical simulation

The acoustic design of the Poul la Cour Tunnel was evaluated prior to construction with a numerical finite element model. For a detailed description of the method, the reader is referred to [9]. The transmission loss of the diffuser was also assessed in Ref. [9], however, the amount of absorption in the diffuser has increased by a factor of about three since the original design and finite element simulation. Therefore, in order to model the transmission loss of the diffuser, another numerical approach is taken in the present study. A combined ray-tracing and finite difference (FDTD) method [26] is applied to a simplified 3D model of the diffuser, with constant cross-section area, using the absorption coefficients from Table 2. The output of the method is impulse responses at predefined positions and the transmission loss is estimated from the method described in Sec. 3.1.

In the following sections, numerical and experimental results are compared. To evaluate the agreement between the finite element model and the proposed experimental methodology an arbitrary criterion of 3 dB is used. If the the results fall within this criterion, the numerical model is said to be validated by the experimental method.

4 Results

4.1 Guide vanes

The transmission loss of the guide vanes in one-third octave bands is shown in Fig. 8. At high frequencies (2000 Hz-5000 Hz), an agreement within 3 dB is observed between the numerical results from [9] and measurements. At low frequencies (63 Hz-160 Hz), there is a clear discrepancy between the numerical results and measurements. This is in line with the applicability of the experimental method, due to boundary interference, shown in Table 3. The peak of the transmission loss is found in the 500 Hz band for corners 1 and 4 and in the 315 Hz band for corner 2 and 3. This is in agreement with the guide vane design described in Sec. 2. Furthermore,

the background noise was measured at each corner. The signal-to-noise (SNR) ratios shown in Fig. 9 verifies that the transmission losses shown in Fig. 8 are not affected by background noise.

Discrepancies above 300 Hz (the cut-off between 2D and 3D finite element simulations in [9]) are likely due to different source characteristics between the finite element model and measurements. In the finite element simulation, a plane wave impinging on the absorbers is assumed, whereas the experimental setup used a point source. The point source can be approximated as a plane wave at large distances but given the limited space available in the wind tunnel, the source distance might not have been sufficient for a plane wave approximation to hold. The consequence of this is that more sound will be scattered going into the absorber and increase the number of wave reflections before exiting, resulting in a higher transmission loss. This is especially true at low frequencies, where the source distance is shorter, relatively, compared to the wavelength.

A noticeable deviation between experimental and numerical results is seen for corner 2 (second sub-figure from top in Fig. 8). In the range 500 Hz-1000 Hz, experimental results show up to 10 dB higher TL compared to the simulation. Comparing this to corner 3, which has the exact same dimensions as corner 2, where a good agreement between experimental and numerical results is observed, it is questionable if the numerical results are trustworthy in this frequency range.

One benefit of the proposed method is the ability to study the sound propagation in the time-domain by looking at the impulse responses. To exemplify, a schematic overview of corner 1 is shown in Fig. 10. The measured impulse responses, filtered in 1/3 octave bands, at inlet and outlet of corner 1 are shown in Fig. 11 for 200 Hz and 500 Hz. The distance between each guide vanes is 0.6m, designed to achieve a maximum absorption at half a wavelength $f = c/0.6 \approx 570$ Hz, assuming a parallel baffle as mentioned in Sec. 2.1. This is seen from the impulse responses in Fig. 11, where the transmitted energy at the outlet (dashed line) is much higher at 200 Hz than at 500 Hz. Thus, at 500 Hz, a much smaller fraction of the incident energy is transmitted to the receiver at the outlet, which is in line with the expected absorption properties of the guide vane design. Additionally, at 200 Hz the impulse response at the inlet has a maximum at approximately $\tau = 45$ ms with a second peak around $\tau = 75$ ms. The second peak, which carries about 25% of the energy of the first peak, is most likely due to a reflection from the end-wall, behind the guide vanes, as it coincides with a travel time of $2 \cdot 6 \text{ m} / 340 \text{ m/s} \approx 35$ ms. At low frequencies, the sound waves propagate largely undisturbed through the guide vanes. At higher frequencies, the propagation is expected to be due to multiple reflections through the guide vanes. Considering a 2D wave impinging on the corner, the wave travels through different paths. The shortest path is via the left side of the corner, and the longest via the right. Path distances from the plane at the inlet microphone to the three microphone positions (A1-A3) at the outlet are approximately 6, 9 and 12m, corresponding to propagation times of 17 ms, 26 ms, and 35 ms. This behavior is observed by a cross-correlation analysis (omitted here due to space constraints) at 1/3 octave bands 1250 Hz and 4000 Hz. Microphone position A1 attains the highest correlation coefficient at both 1250 Hz and 4000 Hz compared to position A2 and A3. This is expected since the microphone at A1 is placed right at the exit of the inner most channel of the guide vanes and less exposed to scattering and reflections from multiple channels than the microphones positioned at A2 and A3. The maximum time lag, τ_{max} , is seen to increase

from position A1 to A3: 16 ms, 27 ms, and 33 ms, corresponding to the expected travel times found above. This shows, that a wave impinging on the guide vanes travels through individual channels, where energy is absorbed by the absorbing panels in the guide vane walls, and at high frequencies transmitted with a time delay corresponding to the travel time of that particular channel. These findings are in line with the results in [14], where the frequency-dependent propagation paths for non-absorbing guide vanes are mapped.

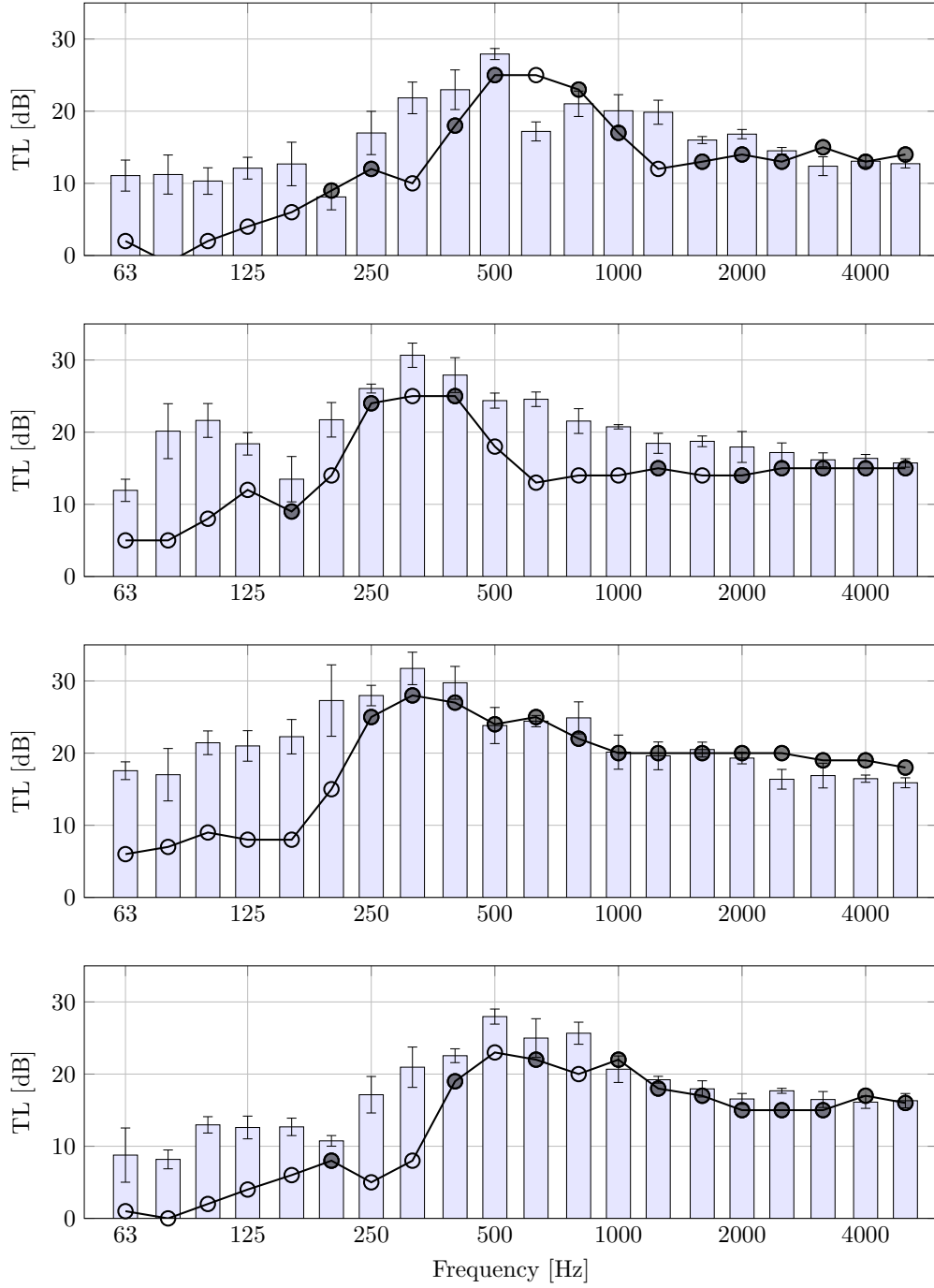


Figure 8: Transmission loss (TL) of guide vanes 1 to 4 (from top to bottom) in 1/3 octave bands. Comparison between simulations (line with circle marks) and measurements (filled bars). Circle marks are filled where difference between simulations (from [9]) and measurements (with uncertainty) is less than 3dB. Error bars indicate one standard deviation of measurements.

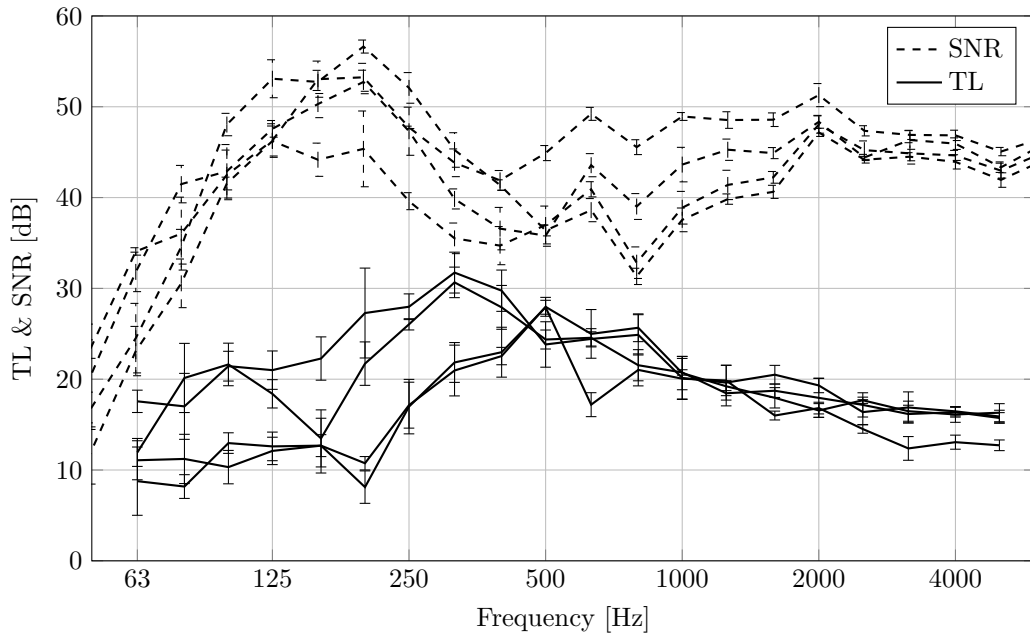


Figure 9: Signal-to-noise ratios (SNR) shown with guide vanes transmission losses (TL) from Fig. 8. The SNR is sufficiently above the insertion losses to ensure that background noise does not affect TL estimation.

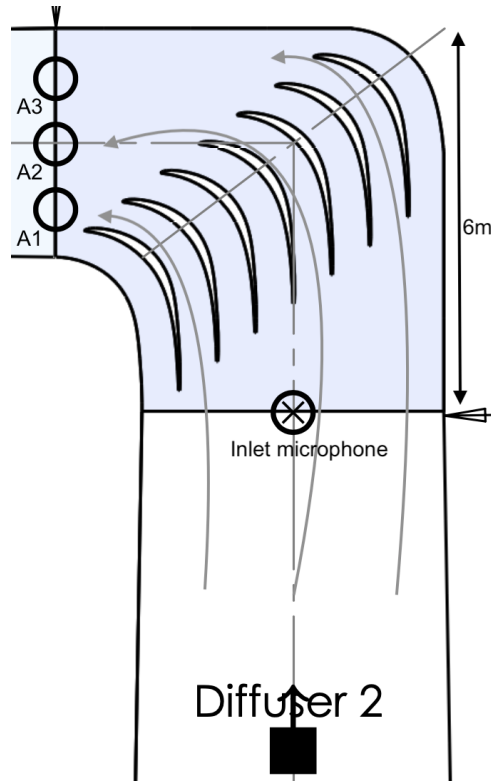


Figure 10: Schematic of corner 1 and wave propagation paths. Loudspeaker (■) and microphones at inlet (⊗) and outlet (⊙).

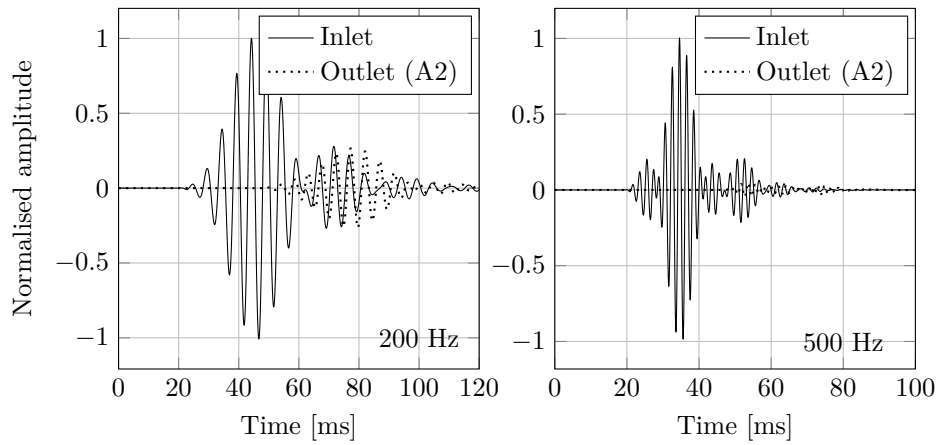


Figure 11: Impulse response at inlet and outlet of corner 1 in 1/3 octave bands 200 Hz (left) and 500 Hz (right).

4.2 Diffuser

The transmission loss of the diffuser is shown in Figure 12. As mentioned above, the numerical results were not obtained by a finite element simulation as it was the case for the guide vanes and fan silencer. Instead, a combined ray-tracing and FDTD method was applied to a simplified 3D model of the diffuser. Agreements within 3 dB between the experimental and numerical results are seen in the mid-frequency range from 400 Hz to 1600 Hz. Slightly larger deviations are observed in some 1/3 octave bands towards 5000 Hz. At frequencies below 400 Hz, the experimentally determined transmission loss is 5 to 10 dB higher than the simulations. This is in line with the bias due to wall interference mentioned above.

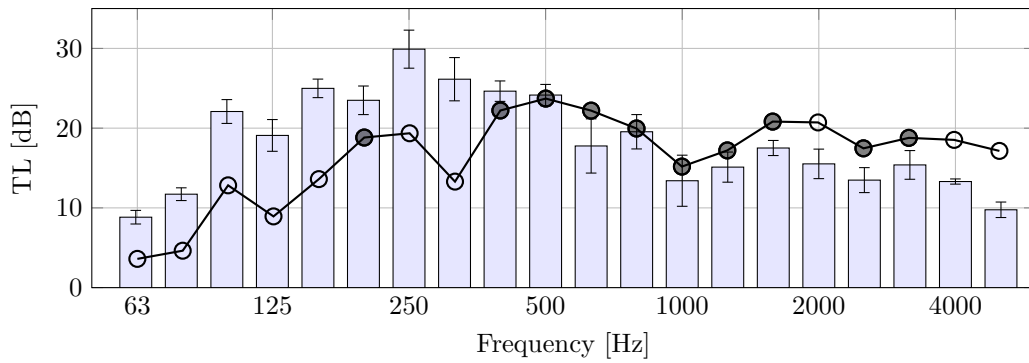


Figure 12: Transmission loss of the diffuser in 1/3 octave bands. Circle marks are filled where difference between simulations (described in Sec. 3.5) and measurements (with uncertainty) is less than 3dB. Error bars indicate one standard deviation of measurements.

4.3 Fan silencer

The transmission loss of the fan is given in the downstream direction (through corners 3 and 4) and upstream direction (through corners 2 and 1). Downstream results are shown in Fig. 13. Agreements within 3dB between the finite element simulation and measurements are seen in the 1/3 octave bands from 630Hz to 3150Hz. At lower frequencies, the measured transmission loss is 10 to 20 dB lower than the simulations. From the signal-to-noise ratio (shown in dashed in Fig. 13) it is evident, that this difference at low frequencies can be ascribed to insufficient power of the reference source. Upstream results are shown in Fig. 14. A better agreement is seen in the low frequencies compared to the downstream transmission loss in Fig. 13. At frequencies from 1000Hz and above, the measurements show a higher transmission loss than the simulations.

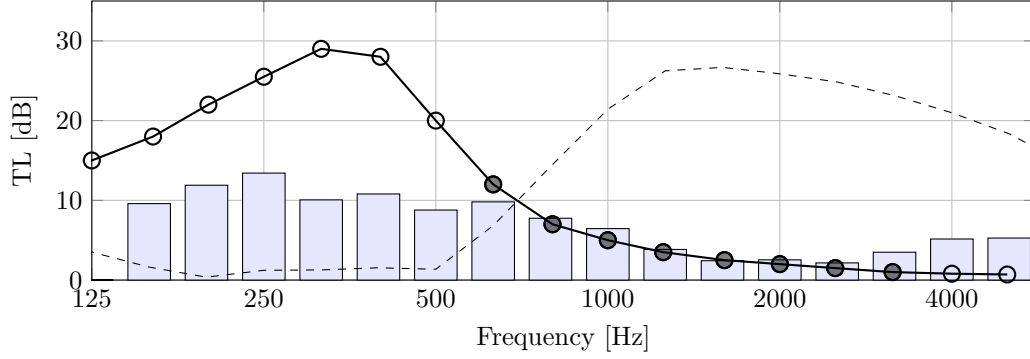


Figure 13: Transmission loss (TL) of fan (downstream direction) in 1/3 octave bands. Comparison between simulations (line with circle marks) and measurements (filled bars). Circle marks are filled where difference between simulation and measurements is less than 3dB. Signal-to-noise ratio is shown in dashed.

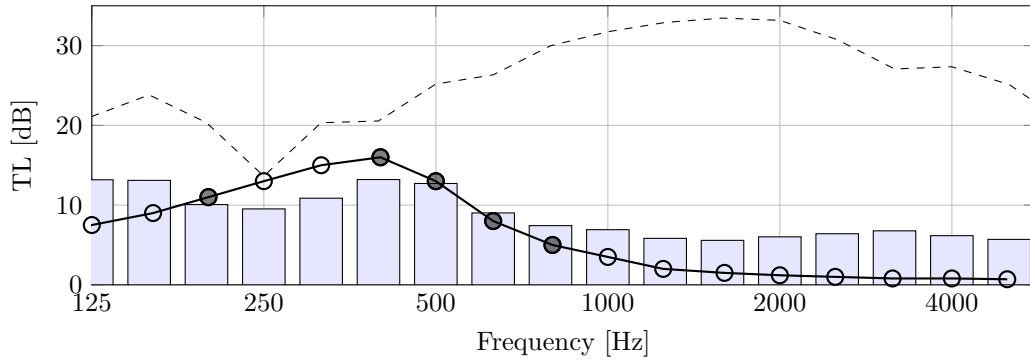


Figure 14: Transmission loss (TL) of fan (upstream direction) in 1/3 octave bands. Comparison between simulations (line with circle marks) and measurements (filled bars). Circle marks are filled where difference between simulation and measurements is less than 3dB. Signal-to-noise ratio is shown in dashed.

5 Discussion

The presented methodology has in general enabled validation of numerical simulations in-situ at mid to high frequencies. However, the method is not valid in the low-frequency range where the physical distance of the microphone to rigid surfaces (typically the floor) presents a clear bias by overestimation of the transmission loss. In the experimental setup, microphones were placed at a height of approximately 1.6 m while the height of the airline duct varied from approximately 6 m-9 m. Moving the microphones further from the floor would have improved the low frequency results, however, the distance to the side walls still limits the method. Additionally, in the frequency range from the first duct modes to a sufficiently diffuse sound field, modes dominate the sound field and makes measurements more prone to positional bias. This is also observed in the standard deviation of measurements at low frequencies (see Fig. 8). More spatial averages could improve the results at low frequencies.

Alternative measurement techniques with either an intensity probe or a rotating microphone stand could also be employed. Both methods measure a larger spatial average of the sound field compared to the methodology of the present paper and is thus less affected by positional bias due to duct modes. These methods, however, are not suitable for impulse response measurements and the accompanying time-domain analysis that comes with it and exemplified above.

6 Conclusion

In this study, a methodology for in-situ estimation of transmission loss in a wind tunnel was presented. A comparison between a finite element simulation and experimental results showed good agreement in the mid to high frequencies, validating the numerical model and the acoustic design of the wind tunnel. In addition, the proposed method provided insight regarding the sound propagation via assessment of impulse responses. The present work opens for further investigations of the design of acoustic wind tunnels which is not possible via numerical methods. Alternative methods, based on power-flow considerations, have been presented and discussed, wherever the proposed method was not applicable. Overall, more than half of the frequency bands across all results were validated, which suggests that the method has good potential as a general approach to validate in-situ the transmission loss of wind tunnel absorbers.

Acknowledgments

The authors wish to acknowledge Peter Davidsson for constructive discussions about the finite element simulations, and Ebba Dellwik and Helge Aagaard Madsen for their comments during the writing of this manuscript.

References

- [1] H. H. Hubbard and J. C. Manning. *Aeroacoustic research facilities at NASA Langley Research Center: Description and operational characteristics*. Tech. rep. 1983.
- [2] M. Pott-Pollenske and J. Delfs. “Enhanced capabilities of the Aeroacoustic Wind Tunnel Braunschweig”. In: *14th AIAA/CEAS Aeroacoustics Conference (29th AIAA Aeroacoustics Conference)*. 2008. DOI: 10.2514/6.2008-2910.
- [3] T. Ito et al. “Aerodynamic/aeroacoustic testing in anechoic closed test sections of Low-speed wind tunnels”. In: *16th AIAA/CEAS Aeroacoustics Conference (31st AIAA Aeroacoustics Conference)*. American Institute of Aeronautics and Astronautics Inc., Jan. 2010, pp. 2010–3750. DOI: 10.2514/6.2010-3750.
- [4] A. Bergmann. “The aeroacoustic wind tunnel DNW-NWB”. In: *18th AIAA/CEAS Aeroacoustics Conference (33rd AIAA Aeroacoustics Conference)*. 2012. DOI: 10.2514/6.2012-2173.
- [5] F. Méry. “Low speed anechoic closed test section at ONERA S1MA wind tunnel”. In: *22nd AIAA/CEAS Aeroacoustics Conference, 2016*. 2016. DOI: 10.2514/6.2016-2895.
- [6] E. Sarradj et al. “Acoustic and aerodynamic design and characterization of a small-scale aeroacoustic wind tunnel”. In: *Applied Acoustics* 70.8 (Aug. 2009), pp. 1073–1080. DOI: 10.1016/j.apacoust.2009.02.009.
- [7] T. Chong, P. Joseph, and P. Davies. “Design and performance of an open jet wind tunnel for aero-acoustic measurement”. In: *Applied Acoustics* 70.4 (Apr. 2009), pp. 605–614. DOI: 10.1016/j.apacoust.2008.06.011.
- [8] W. J. Devenport et al. “The Kevlar-walled anechoic wind tunnel”. In: *Journal of Sound and Vibration* 332.17 (2013), pp. 3971–3991. DOI: 10.1016/j.jsv.2013.02.043.
- [9] W. Devenport et al. “Design and Operation of Hybrid Aeroacoustic Wind Tunnels”. In: *Design and Operation of Aeroacoustic Wind Tunnel Tests for Group and Air Transport*. Vol. STO-EN-AVT. Jan. 2017. DOI: 10.14339/STO-EN-AVT-287.
- [10] P. Liu et al. “Design and performance of a small-scale aeroacoustic wind tunnel”. In: *Applied Acoustics* 116 (Jan. 2017), pp. 65–69. DOI: 10.1016/j.apacoust.2016.09.014.
- [11] Y. D. Mayer et al. “Design and performance of an aeroacoustic wind tunnel facility at the University of Bristol”. In: *Applied Acoustics* 155 (Dec. 2019), pp. 358–370. DOI: 10.1016/j.apacoust.2019.06.005.
- [12] C. Doolan et al. “The UNSW anechoic wind tunnel”. In: *Australian Acoustical Society Annual Conference, AAS 2018*. Australian Acoustical Society, Jan. 2019, pp. 79–80.
- [13] L. L. Beranek, S. Labate, and U. Ingard. “Noise Control for NACA Supersonic Wind Tunnel”. In: *Journal of the Acoustical Society of America* 27.1 (Jan. 1955), pp. 85–98.
- [14] P. Soderman and L. Hoglund. “Wind-tunnel fan noise reduction including effects of turning vanes on noise propagation”. In: American Institute of Aeronautics and Astronautics (AIAA), Mar. 1979, pp. 1–6. DOI: 10.2514/6.1979-642.
- [15] R. E. Hayden and J. F. Wilby. *Sources, paths, and concepts for reduction of noise in the test section of the NASA Langley 4x7m wind tunnel*. Tech. rep. Jan. 1984.

- [16] M. L. Munjal. *Acoustics of ducts and mufflers : with application to exhaust and ventilation system design*. Wiley, 1987.
- [17] A. C. Raes. “A Tentative Method for the Measurement of Sound Transmission Losses in Unfinished Buildings”. In: *Journal of the Acoustical Society of America* 27.1 (Jan. 1955), pp. 98–102. DOI: 10.1121/1.1907502.
- [18] M. Garai and P. Guidorzi. “European methodology for testing the airborne sound insulation characteristics of noise barriers in situ: Experimental verification and comparison with laboratory data”. In: *The Journal of the Acoustical Society of America* 108.3 (Jan. 2000), pp. 1054–1067. DOI: 10.1121/1.1286811.
- [19] *Acoustics – Determination of sound power levels and sound energy levels of noise sources using sound pressure – Precision methods for anechoic rooms and hemi-anechoic rooms*. Standard. Geneva, CH: International Organization for Standardization, 2012.
- [20] T.J. Cox. *Acoustic Absorbers and Diffusers*. CRC Press, Jan. 2002. DOI: 10.1201/9781482288254.
- [21] F. Jacobsen and P. M. Juhl. *Fundamentals of General Linear Acoustics*. Wiley, 2013.
- [22] H. Kuttruff. *Room Acoustics, Fifth Edition*. CRC Press, Apr. 2014, pp. 1–374. DOI: 10.1201/9781482266450.
- [23] M. R. Schroeder and K. H. Kuttruff. “On Frequency Response Curves in Rooms. Comparison of Experimental, Theoretical, and Monte Carlo Results for the Average Frequency Spacing between Maxima”. In: *The Journal of the Acoustical Society of America* 34.1 (1962), pp. 76–80. DOI: 10.1121/1.1909022.
- [24] H. Nélisse and J. Nicolas. “Characterization of a diffuse field in a reverberant room”. In: *The Journal of the Acoustical Society of America* 101.6 (1997), pp. 3517–3524. DOI: 10.1121/1.418313.
- [25] K. Beissner. “On the plane-wave approximation of acoustic intensity”. In: *The Journal of the Acoustical Society of America* 71.6 (June 1982), pp. 1406–1411. DOI: 10.1121/1.387835.
- [26] R. Thomas. *Wayverb: Hybrid waveguide and ray-tracing room acoustic simulator with GPU acceleration*. <https://github.com/reuk/wayverb>. Version 0.0.1. Aug. 2017.

Paper B

Published in Conference Proceedings of Berlin Beamforming Conference (Be-BeC), 2018.



NOISE QUANTIFICATION WITH BEAMFORMING DECONVOLUTION: EFFECTS OF REGULARIZATION AND BOUNDARY CONDITIONS

Oliver Lylloff¹ and Efren Fernandez-Grande²

¹Aerodynamic Design, Dep. Wind Energy, Technical University of Denmark
Frederiksborgvej 399, 4000, Roskilde, Denmark

²Acoustic Technology, Dep. Electrical Engineering, Technical University of Denmark
Ørsted Plads 352, 2800 Kgs. Lyngby, Denmark

ABSTRACT

Delay-and-sum (DAS) beamforming can be described as a linear convolution of an unknown sound source distribution and the microphone array response to a point source, i.e., point-spread function. Deconvolution tries to compensate for the influence of the array response and reveal the true source distribution. Deconvolution is an inverse problem in which measurement noise can become dominant and yield meaningless solutions if the problem is not regularized (typically with Tikhonov regularization or a sparsity constraint). Therefore, the obtained solution estimate depends on the choice of regularization parameter, which in turn is highly problem dependent. Additionally, if sound sources are located near the edges of the computational domain, a discontinuity of sound power occurs that can result in a "ringing" effect in the deconvolved image. To remedy this, various boundary conditions can be assumed to model the sound field behaviour outside the computational domain. In this paper, noise quantification from deconvolution is investigated to better understand the derived effect on absolute noise levels. Using benchmark test cases from the aero-acoustic community, absolute noise levels is obtained from deconvolution and compared to that of the test cases. The effects of regularization and boundary conditions are discussed and practical usage scenarios are given.

1. INTRODUCTION

Delay-and-sum (DAS) beamforming is a popular signal processing technique for localizing aero-acoustic sources. Due to inadequate resolution at low frequencies and grating lobes at high frequencies [1], deconvolution methods can be applied to improve the source localization [2]. The outcome is typically a more precise source localization with the ability to obtain absolute

noise levels from selected regions. Classical deconvolution algorithms, such as DAMAS [3], CLEAN [4], NNLS [5], RL [6, 7] have been shown to produce successful reconstructions [2, 8–10]. However, these algorithms and the reconstructions they produce still have limitations and an extended computational cost is one of the main drawbacks.

The deconvolution problem is typically formulated as a linear least-squares problem that can be readily solved by a number of available algorithms [11]. However, in practical usage scenarios, some care is required to obtain trustworthy and physical solutions. The deconvolution problem is often large, which makes a solution infeasible for some (higher-order) algorithms. Additionally, due to the ill-posed nature of the deconvolution problem, regularization is typically added to avoid solutions dominated by noise [12].

There has been a natural interest from the aero-acoustic community to adopt algorithms that originate from the fields of image deblurring and inverse problems, e.g., [13–18]. While these advances show promising results for the deconvolution problem, it can be difficult to evaluate the reconstructions without a common reference. To promote quantitative assessments of microphone array techniques, standardized test data sets (synthesized and experimental) have recently been made publicly available [19]. The first quantitative comparison of deconvolution algorithms across several different research institutions was given in [20, 21].

The purpose of this work is to investigate how absolute noise levels, derived from beamforming deconvolution, are affected by adding regularization and boundary conditions. The synthetic data set described in [20] is used in this work.

Two common regularization strategies are applied to a deconvolution algorithm: A squared ℓ_2 -norm and a sparsity inducing ℓ_1 -norm. Combined with 7 different boundary conditions, absolute noise levels are reconstructed and evaluated against the reference spectra that accompanies the test data set. To give a fair comparison between different boundary conditions and regularization terms, a so-called proximal gradient algorithm (FISTA [13, 22]) is chosen to perform the deconvolution task. The theory behind proximal methods originates from convex optimization theory [23] and has the advantage that a single implementation of the deconvolution algorithm can evaluate several different regularization strategies.

The data generation, analysis and figures used for the paper is available online [24] in the spirit of reproducible research.

This paper is organized as follows: In Sec. 2, the problem formulation and beamforming framework is described. The deconvolution problem is then stated and the proximal approach is introduced for adding regularization. The simulation study in Sec. 3 is divided into two cases: the first focuses on boundary conditions, and the second on choice of regularization.

In the following, vectors are denoted by boldface lowercase letters and matrices by boldface uppercase letters.

2. BEAMFORMING DECONVOLUTION

Consider the sound pressure measured using a microphone array with M microphones due to a single point source located at \mathbf{r}_s . Assuming free-field conditions and no flow, the sound pressure at the m 'th microphone, \mathbf{r}_m , is,

$$p(\mathbf{r}_m) = \frac{q(\mathbf{r}_s)}{|\mathbf{r}_s - \mathbf{r}_m|} e^{-jk|\mathbf{r}_s - \mathbf{r}_m|} \quad (1)$$

where q is the strength of the source, $|\mathbf{r}_s - \mathbf{r}_m|$ is the distance from the sound source to the m 'th microphone, and k is the wave number [25]. By collecting the sound pressure from all microphones and arranging them in a vector $\mathbf{p} \equiv [p(\mathbf{r}_1), p(\mathbf{r}_2), \dots, p(\mathbf{r}_M)]^T$, and computing the cross spectral matrix $\mathbf{C} \equiv E\{\mathbf{p}\mathbf{p}^H\}$, the mean-squared beamforming output for a focus point \mathbf{r}_f is given by,

$$b(\mathbf{r}_f) = \mathbf{v}(\mathbf{r}_f)^H \mathbf{C} \mathbf{v}(\mathbf{r}_f) \quad (2)$$

where $\mathbf{v}(\mathbf{r}_f)$ is a steering vector that contains transfer functions from the microphone array to the focus point, $(\cdot)^H$ is the hermitian transpose, and $E\{\cdot\}$ is the expectation operator. Computing the real part of Eq. (2) for all focus points in the area of interest produces a beamforming map.

The formulation of the steering vector \mathbf{v} can be found in different variations in the literature. In [26] four variants are collected and identified that can either reconstruct the source position or level correctly. In this work, formulation III, that was found to reconstruct the level correctly, is used,

$$v_m(\mathbf{r}_f) = \frac{e^{-jk(|\mathbf{r}_f - \mathbf{r}_m| - |\mathbf{r}_f - \mathbf{r}_0|)}}{|\mathbf{r}_f - \mathbf{r}_0| |\mathbf{r}_f - \mathbf{r}_m| \sum_{j=1}^N |\mathbf{r}_f - \mathbf{r}_j|^{-2}}. \quad (3)$$

Assuming incoherent sources, the cross-spectral matrix \mathbf{C} can be modelled as

$$\tilde{\mathbf{C}} = \sum_{n=1}^{N^2} \overline{|q|^2} \cdot \mathbf{v}(\mathbf{r}_n) \mathbf{v}(\mathbf{r}_n)^H, \quad (4)$$

where $\overline{(\cdot)}$ is the spectral average. The beamforming output in Eq. (2) can thus be modelled as

$$b(\mathbf{r}_f) = \sum_{n=1}^{N^2} \overline{|q|^2} \cdot \text{PSF}(\mathbf{r}_f, \mathbf{r}_n) \quad (5)$$

where n is the n 'th grid point in a $N \times N$ computational grid, PSF is the beamforming output due to a unit-power point source, i.e., point-spread function,

$$\text{PSF}(\mathbf{r}_f, \mathbf{r}_n) = \mathbf{v}(\mathbf{r}_f)^H [\mathbf{v}(\mathbf{r}_n) \mathbf{v}(\mathbf{r}_n)^H] \mathbf{v}(\mathbf{r}_f). \quad (6)$$

The PSF array, \mathbf{P} , is the matrix, or image, of a source placed in a particular grid point \mathbf{r}_n . Computing \mathbf{P} for all grid points and stacking them column-wise produces the blurring matrix \mathbf{A} with dimensions $N^2 \times N^2$. If the point-spread function is shift-invariant, Eq. (5) is modified to

$$b(\mathbf{r}_f) = \sum_{n=1}^{N^2} \overline{|q|^2} \cdot \text{PSF}(\mathbf{r}_f - \mathbf{r}_n) \quad (7)$$

which corresponds to a linear convolution of the source distribution and a single point-spread function. The PSF array, \mathbf{P} , is then only computed for a source located at the centre of the domain and the blurring matrix \mathbf{A} is a block Toeplitz with Toeplitz blocks (BTTB) matrix. It is known that the Fast Fourier Transform can be used to efficiently compute matrix vector products $\mathbf{A}\mathbf{x}$ without forming \mathbf{A} explicitly [12].

The deconvolution problem is given by,

$$\underset{\mathbf{q} \in \mathbb{R}^{N \times N}}{\text{minimize}} \quad \frac{1}{2} \|\mathbf{A}\mathbf{q} - \mathbf{b}\|_2^2, \quad (8)$$

where $\mathbf{q} = [|q_1|^2, |q_2|^2, \dots, |q_{N^2}|^2]$, $\mathbf{A}\mathbf{q}$ is a two-dimensional convolution product computed by $\mathcal{F}^{-1}[\mathcal{F}(\mathbf{q}) \odot \mathcal{F}(\mathbf{P})]$, where \mathcal{F} and \mathcal{F}^{-1} is the 2D Fourier Transform operator and its inverse, and (\odot) is the element-wise product. The computational advantage comes from the fact that the convolution $\mathbf{A}\mathbf{q}$ can be performed by the Fast Fourier Transform without forming the blurring matrix \mathbf{A} . Due to its periodic nature, padding is required to avoid wrap-around errors [27]. This padding impose a boundary condition on the beamforming map, i.e., the assumed behaviour of the sound field outside the field of view. The derived effect of boundary conditions on reconstructed noise levels are the focus of this paper.

2.1. The Proximal Approach

The optimization problem stated in Eq. (8) is convex, which means that if a minimum of the deconvolution problem can be found it is guaranteed to be a global minimum of the optimization problem [28].

The starting point in Eq. (8) can provide useful reconstructions, however, a non-negativity constraint is typically added to the optimization problem due to the non-negative source powers, \mathbf{q} ,

$$\underset{\mathbf{q} \in \mathbb{R}^{N \times N}}{\text{minimize}} \quad \frac{1}{2} \|\mathbf{A}\mathbf{q} - \mathbf{b}\|_2^2 + I_+(\mathbf{q}) \quad (9)$$

$$\text{where } I_+(\mathbf{q}) = \begin{cases} 0, & \text{if } q \in \mathbb{R}_+^n \\ \infty, & \text{otherwise,} \end{cases}$$

where \mathbb{R}_+^n is the non-negative orthant [28]. This formulation is equivalent to the non-negative least squares problem NNLS [2, 5]. What is clear from this formulation is that the objective function is no longer differentiable and deconvolution algorithms that depend on the first or second derivative will break.

With the proximal approach, the optimization problem is split into differentiable and non-differentiable parts. The proximal operator of a non-differentiable function g , is given by

$$\text{prox}_g(v) = \underset{x}{\text{argmin}} \left(g(x) + \frac{1}{2} \|x - v\|_2^2 \right). \quad (10)$$

$\text{prox}_g(v)$ can be interpreted as a point that compromises between minimizing g and being near v [23]. For example, the proximal operator of the indicator function in Eq. (9) is the Euclidean projection of \mathbf{q} onto \mathbb{R}_+^n , i.e., $\max(0, \mathbf{q})$.

With this framework in place, it is possible to introduce additional variations of the optimization problem (9). In this work, two well-known formulations will be applied, namely a squared ℓ_2 -norm regularization term

$$\underset{\mathbf{q} \in \mathbb{R}^{N \times N}}{\text{minimize}} \quad \frac{1}{2} \|\mathbf{A}\mathbf{q} - \mathbf{b}\|_2^2 + \lambda \|\mathbf{q}\|_2^2 + I_+(\mathbf{q}) \quad (11)$$

which is a constrained variation of Tikhonov regularization [29], and a ℓ_1 -norm regularization term,

$$\underset{\mathbf{q} \in \mathbb{R}^{N \times N}}{\text{minimize}} \quad \frac{1}{2} \|\mathbf{A}\mathbf{q} - \mathbf{b}\|_2^2 + \lambda \|\mathbf{q}\|_1 + I_+(\mathbf{q}), \quad (12)$$

which induce sparse solutions and is similar to compressive sensing or LASSO [30]. Other interesting variations that is straight-forward to implement with the proximal approach, include the edge-preserving Total Variation Denoising [31] and Elastic Net [18].

The deconvolution algorithm, which is used in this study, is based on a fast proximal gradient algorithm, FISTA [22], that has been applied to beamforming deconvolution in [13] and extended in [14, 32].

2.2. Boundary Conditions

Boundary conditions model the behaviour of the beamforming map outside the field of view [33]. Consider for instance the simple example of a 3×3 matrix \mathbf{X} ,

$$\mathbf{X} = \begin{bmatrix} 1 & 2 & 3 \\ 4 & 5 & 6 \\ 7 & 8 & 9 \end{bmatrix}.$$

The most common boundary condition is a zero boundary condition. When applied to \mathbf{X} , the matrix is embedded into a larger matrix padded with zeros,

$$\mathbf{X}_{\text{zeroBC}} = \begin{bmatrix} \mathbf{0} & \mathbf{0} & \mathbf{0} \\ \mathbf{0} & \mathbf{X} & \mathbf{0} \\ \mathbf{0} & \mathbf{0} & \mathbf{0} \end{bmatrix}.$$

This boundary condition is a common choice when performing convolutions via the Fast Fourier Transform [27]. If the beamforming map is confined to the centre and nearly zero at the edges, a zero boundary condition might be a realistic model of the behaviour outside the field of view. However, if the beamforming map is nonzero, as is often the case at low frequencies, the sound power "spills over the edge" of the computational domain and a discontinuity occurs that can affect the reconstructed sound map. Four common choices of boundary conditions are shown in Fig. 10.

An additional boundary condition is proposed in this work, the extended BC, that simply requires a re-computation of the beamforming map in an extended computational domain that is larger than the original. The "padding" in this case is just the computed extension of the beamforming map and thus relieves sharp discontinuities at the edge. In all cases, the padding is removed after deconvolution to the region of interest.

3. SIMULATION STUDY

In this study, a synthetic test case of four incoherent point sources are considered (Benchmark 7: Four Monopole Sources [19]). The sources are arranged in a square with side lengths of 0.2 m and a microphone array with 64 microphones is placed at a distance of 0.75 m (see Fig.

1). There are two subcases included in the data set: subcase a, all sources have equal power, and subcase b, where the sources have different power. Reference spectra of each source are included in the data set and the reconstructed sound maps presented in the following are evaluated against the reference by the level difference $\Delta L = L - L_{\text{ref}}$ for each individual frequency bin. The reconstructed levels are estimated by a spatial integration over a square with a side length of 0.1 m centered at the nominal source position.

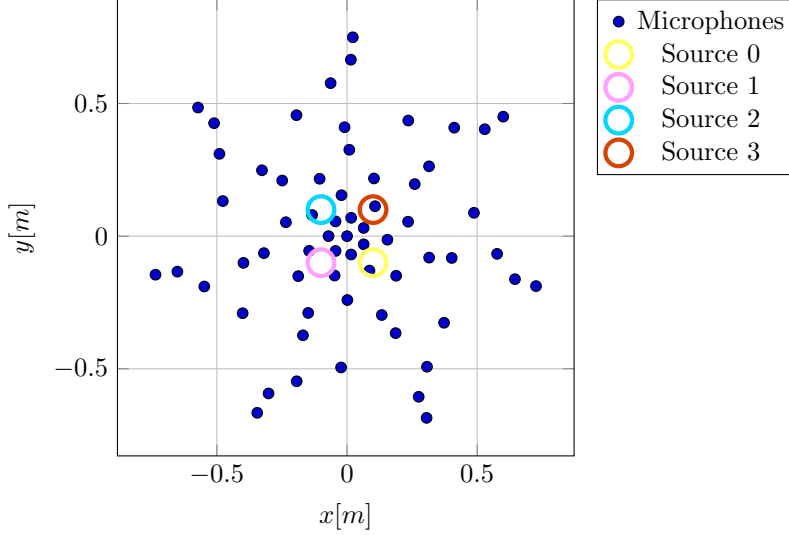


Figure 1: Geometry of the setup.

3.1. Case I: Boundary Conditions

The purpose of this case is to analyse the effects of boundary conditions at low frequencies when the beamforming map has a wide mainlobe and a large discontinuity appears at the edge. Four monopoles with equal power (Benchmark 7, subcase a [19]) is reconstructed from beamforming maps at 7 frequencies $f = [700, 800, 1000, 1500, 2000, 2500, 5000]$ Hz, each with a bin width of 50 Hz. Additionally, 6 different boundary conditions (and one without) is applied to the beamforming maps, this gives a total of 49 reconstructions. The computational domain is restricted to $x = y = [-0.2; 0.2]$ m and the measurement distance is $z = 0.75$ m. The maximum number of iterations with the deconvolution algorithm is set to 3000.

Beamforming maps padded to size $(2N - 1) \times (2N - 1)$ by 6 different boundary conditions (zero, replicate, symmetric, periodic, reflect, and the proposed extended BC) are shown in Fig. 2. Due to the symmetry of the source distribution, the symmetric, periodic, and reflect boundary conditions, coincide and have similar appearances. The beamforming maps at $f = 1000$ Hz and $f = 1500$ Hz are shown in Fig. 3. From a visual inspection, the four sources are barely separated at $f = 1500$ Hz, and at $f = 1000$ Hz it is no longer possible to identify them.

The reconstructed source levels for Source 3 are shown in Table 1. For the sake of brevity, results for the remaining sources, which is very similar, are omitted. All reconstructions at and above 1500 Hz show small level deviations from the reference within ± 1 dB. Below 1500 Hz, only the extended boundary condition, is capable of reconstructing the source level correctly.

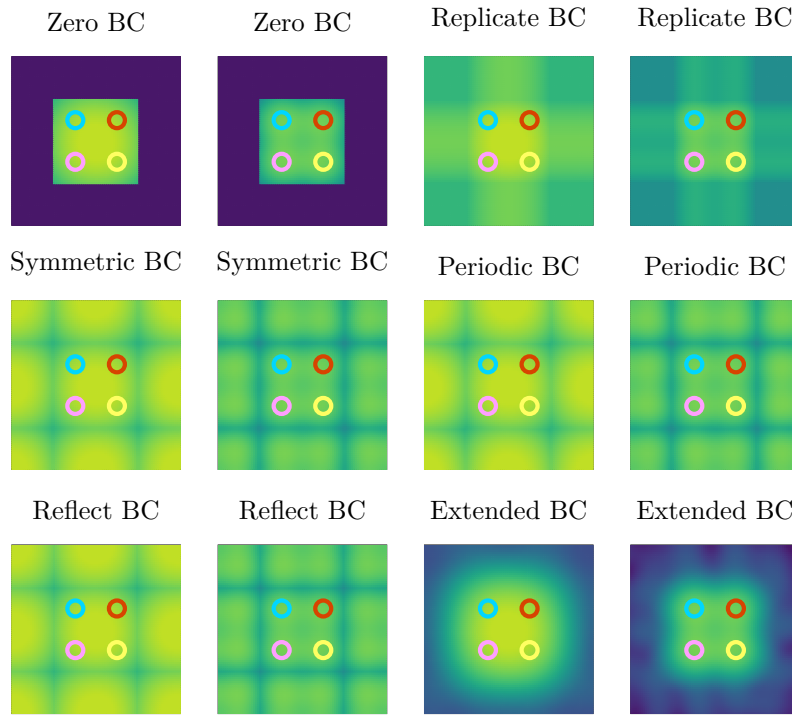


Figure 2: Padded beamforming maps at 1000 Hz (left of each pair) and 1500 Hz (right of each pair). The area of interest is $x = y = [-0.2; 0.2]$ m padded to $x = y = [-0.4; 0.4]$ m and the dynamic range is 18 dB.

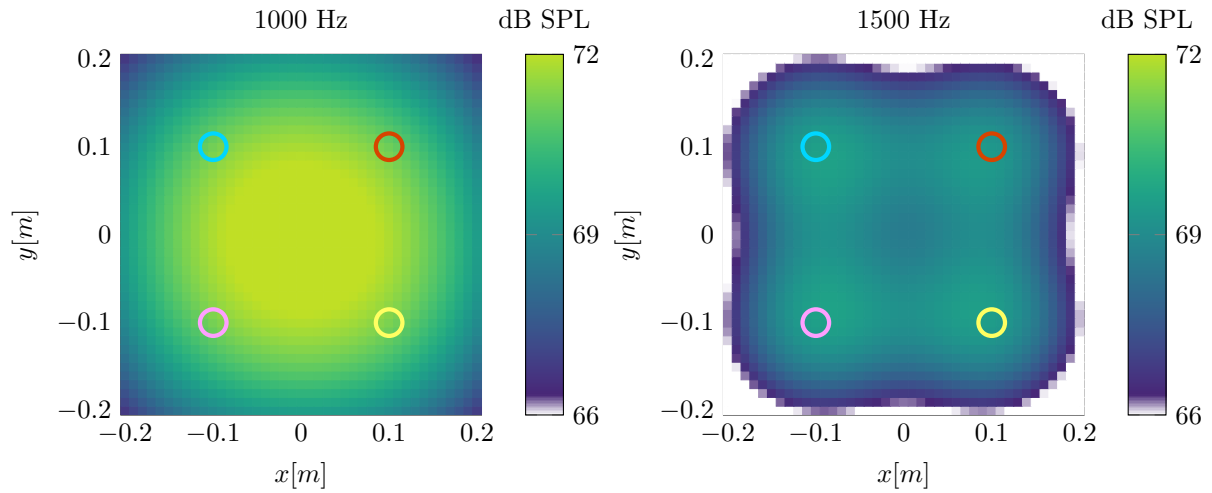


Figure 3: Case I: Beamforming maps at $f = 1000\text{Hz}$ and $f = 1500\text{ Hz}$. Circles indicate positions of point sources.

Surprisingly, the no BC case, without any padding, performs as well as the other cases. Reconstructed source maps for two boundary conditions (zero BC and extended BC) are shown in Fig. 4. Again, for the sake of brevity, only two reconstructions are shown. The remaining re-

Table 1: Level differences (Source 3) from reference $\Delta L = L - L_{ref}$ [dB]. (-): no data.

f [Hz]	700	800	1000	1500	2000	2500	5000
no BC	–	–	–	0.1	0.7	0.8	0.9
zero BC	–	–	–	0.5	0.8	0.9	0.7
replicate BC	–	–	–	0.5	0.8	0.9	0.8
symmetric BC	–	–	–	0.0	0.6	0.8	0.9
periodic BC	–	–	–	0.0	0.7	0.8	0.9
reflect BC	–	–	–	-0.1	0.6	0.8	0.8
extended BC	–	0.8	0.8	0.6	0.7	0.8	0.7

constructions are very similar to the zero BC case. Upon inspection of the reconstructed maps (Fig. 4), it is clear that the reconstructions become useless below a certain frequency limit. This cut-off frequency occurs around 800 Hz for the extended BC but for all other boundary conditions it is around 1500 Hz.

The Rayleigh criterion is commonly used as a measure of resolution and describes the smallest angular separation at which two sources can be separated [34],

$$R \approx 1.22 \frac{L}{D} \lambda, \quad (13)$$

where L is the (on axis) measurement distance, D is the array aperture and λ the wavelength. The resolution as function of frequency for this specific case, with $L = 0.75\text{m}$ and $D = 1.5\text{m}$ is shown in Fig. 5.

At the cut-off frequency of the extended BC, 800 Hz, the resolution is approximately 0.26 m and at 1500 Hz, which is the cut-off frequency of the remaining boundary conditions, the resolution is approximately 0.14 m. These numbers indicate that there is a relationship between resolution, cut-off frequency and boundary condition. The shortest distance from a source to the edge of the unpadded beamforming map is 0.1 m, except for the case of extended BC, that is padded with the natural extension of the beamforming map, where the shortest distance is 0.3 m. One possible explanation is that when the resolution is too low, the sources cannot be separated from edge and deconvolution fails to reconstruct correctly. The cut-off frequency due to that interpretation is from Eq. (13),

$$f_{\min} = 1.22 \frac{L}{D} \frac{c}{R_{\min}}, \quad (14)$$

where c is the speed of sound and R_{\min} is the shortest distance from a source to the edge of the beamforming map. For $R_{\min} = 0.1$, $f_{\min} = 2092\text{Hz}$. This estimate is much higher than what was found empirically above. The cut-off frequency in Eq. (14) can serve as a rule of thumb for a lower frequency limit of deconvolution given certain boundary conditions, however, it is still based on the Rayleigh criterion which is a convenient reference point for resolution rather than a strict physical limit [35].

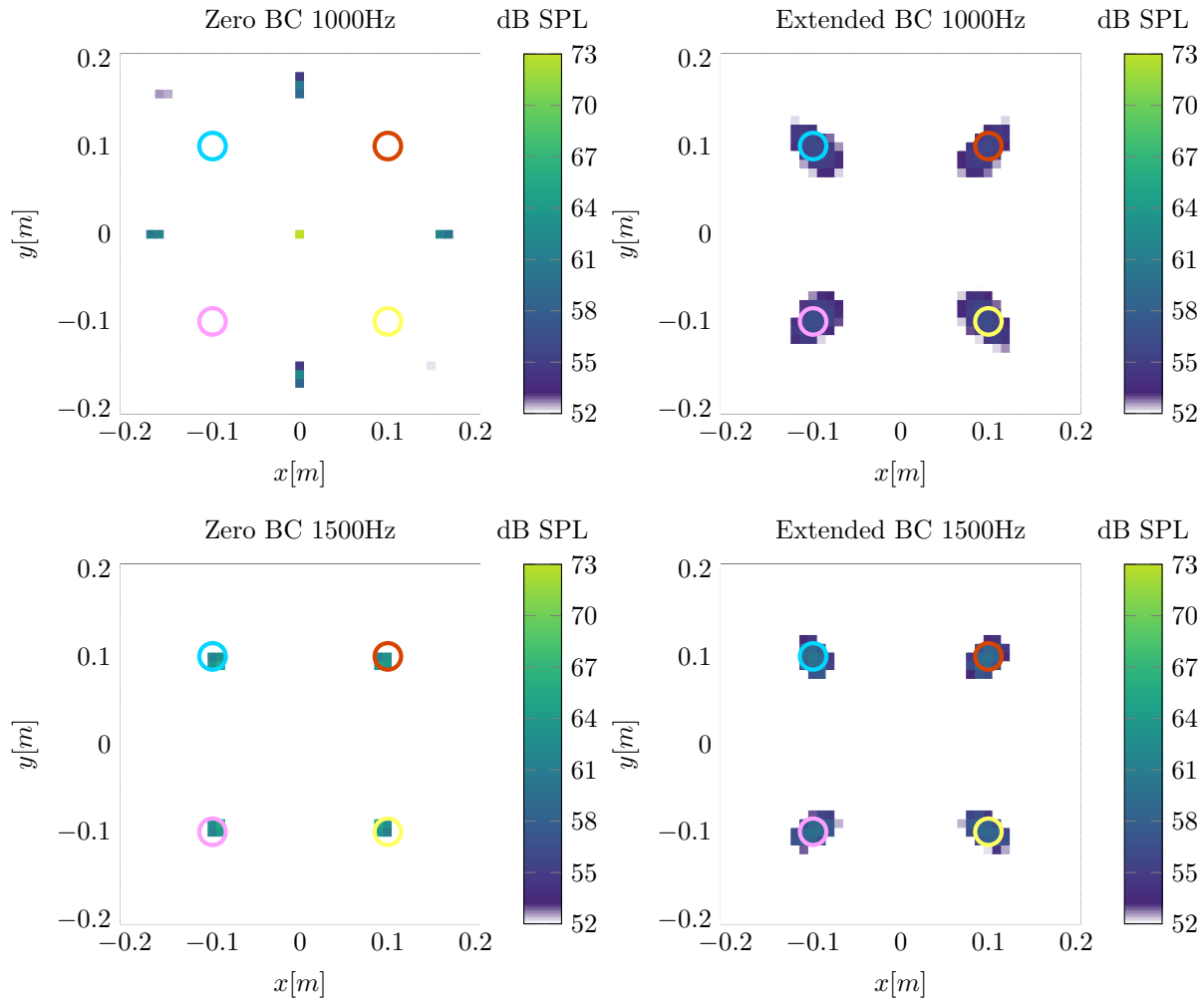


Figure 4: Case I: Reconstructed source maps at $f = 1000\text{Hz}$ and $f = 1500\text{Hz}$. Circles indicate positions of point sources.

3.2. Case II: Regularization

The purpose of this case is to investigate the effects of regularization on absolute noise levels. Similar to Case I (Sec. 3.1), four monopole sources are considered, however, now sub-case b from [19] is used, where the source powers are different. Source 0 is the strongest, Source 1 is -6dB below, Source 2 is -12 dB below Source 0, and Source 3 is -18dB below Source 0. The source levels are reconstructed from beamforming maps at frequencies $f = [500, 550, \dots, 11250]$ Hz with a bin width of 50 Hz. Two regularization terms are added: a ℓ_1 -norm and ℓ_2 -norm term defined in Eq. (11) and (12), respectively, each with 20 different regularization parameters in the range $\lambda = [10^{-5}; 10^2]$. The domain of interest is $x = y = [-0.5; 0.5]$, which gives a cut-off frequency $f_{\min} = 523$ Hz according to Eq. (14). A zero boundary condition is chosen since it was found in Case I that, above the cut-off frequency, all boundary conditions could reconstruct absolute noise levels equally well. The maximum number of iterations with the deconvolution algorithm is again set to 3000.

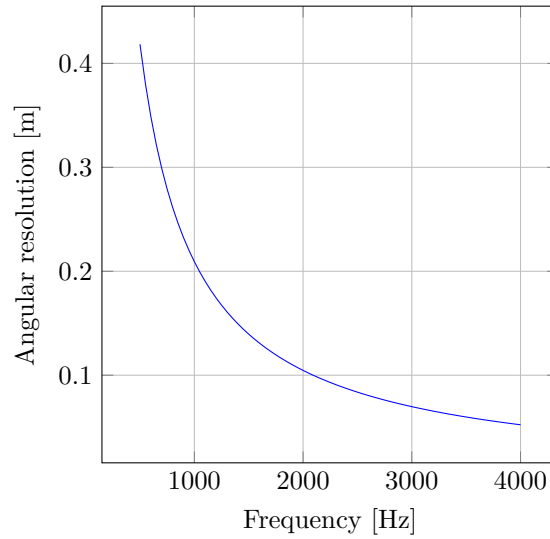


Figure 5: Resolution due to the Rayleigh criterion.

The beamforming maps at $f = 1000$ Hz and $f = 1500$ Hz are shown in Fig. 6 and a comparison between the reconstructions with the two regularization methods are shown in Fig. 7. As expected, the ℓ_1 -norm method induce a more sparse reconstruction than the ℓ_2 -norm. By visual inspection it seems that only two sources are identified properly by the ℓ_1 -norm method whereas three is identified by the ℓ_2 -norm method.

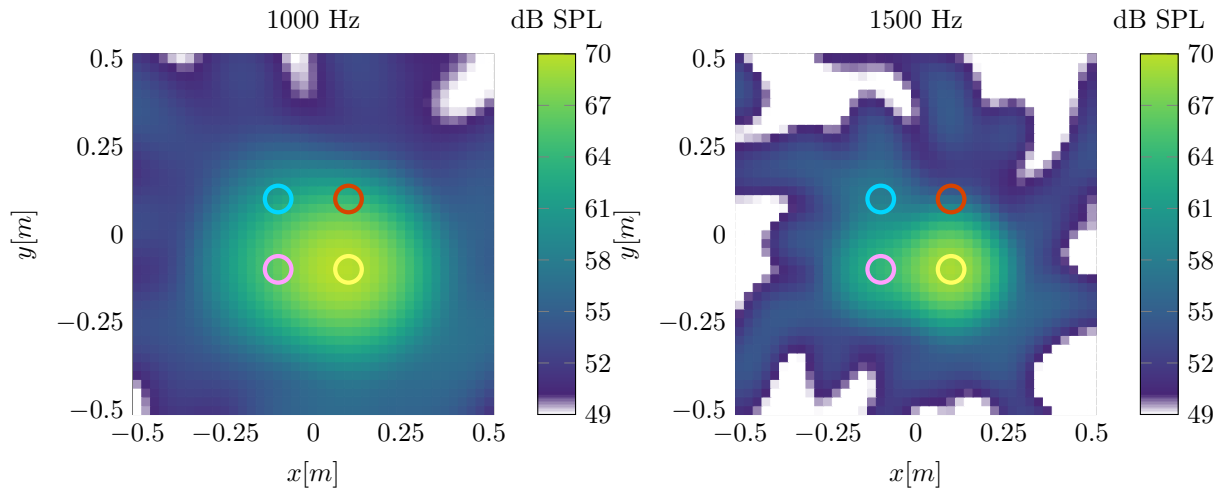


Figure 6: Case II: Beamforming maps at $f = 1000$ Hz and $f = 1500$ Hz. Circles indicate positions of point sources.

The deconvolution problem is solved for every regularization parameter and regularization method in the frequency range of interest. Level differences ΔL are computed by comparing the reconstruction level of each source, determined via spatial integration, with the reference levels from the data set. Figure 8 shows ΔL as function of regularization parameter for 1500 Hz and

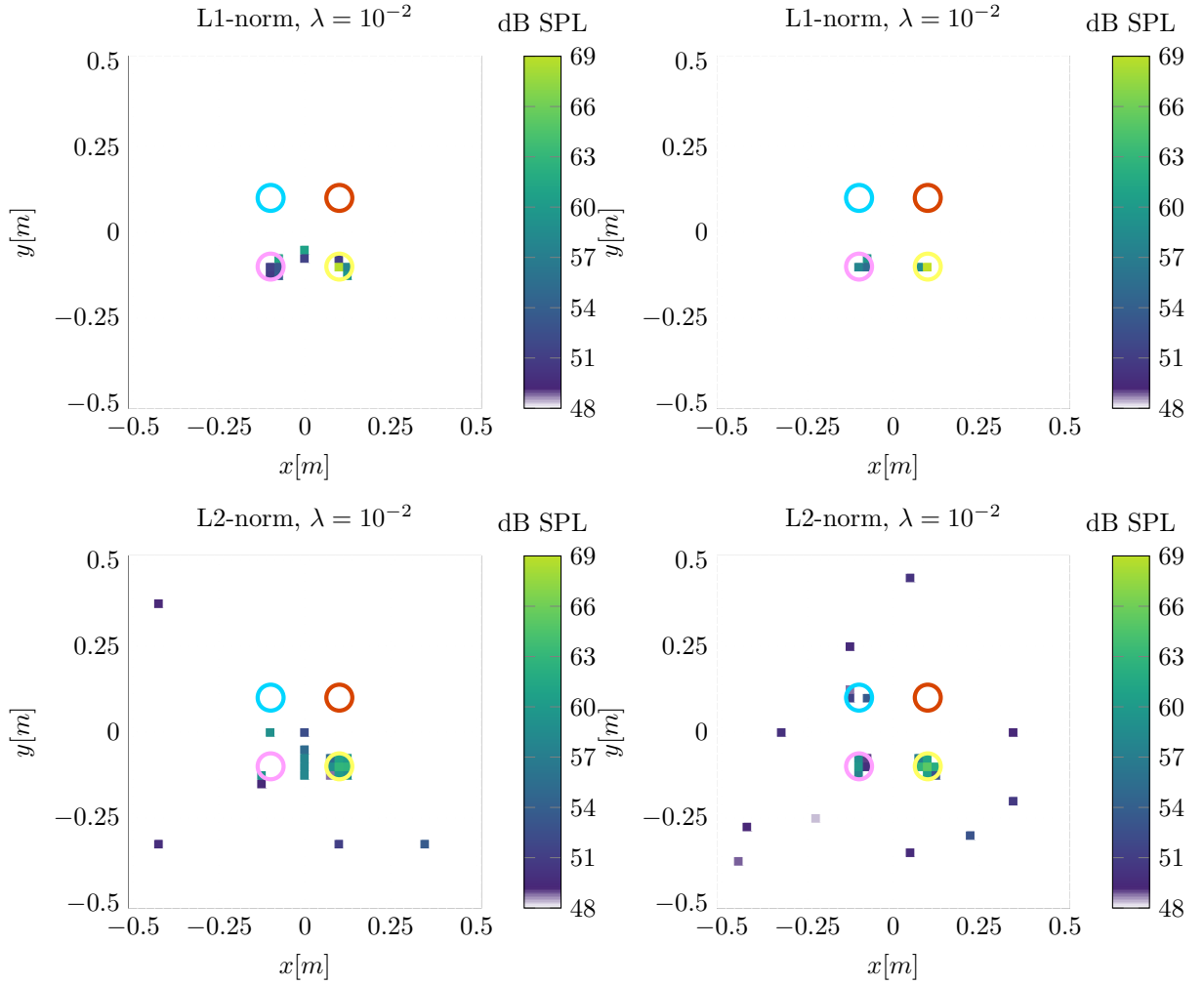


Figure 7: Case II: Reconstructed source maps at $f = 1000\text{Hz}$ (left) and $f = 1500\text{Hz}$ (right) with ℓ_1 -norm and ℓ_2 -norm regularization. Circles indicate positions of point sources.

3000Hz. From this it is clear that both methods can actually identify three of the four sources but due to the chosen regularization parameter, $\lambda = 10^{-2}$, only two is visible with the ℓ_1 -norm method at 1500 Hz.

For small λ values ($< 10^{-4}$), both regularization methods perform well in terms of reconstructed sound levels. This is not an observation that holds in general. The data set has a high signal-to-noise ratio and regularization is not required to obtain good reconstructions. For real-world problems, measurement noise will in general require a need for regularization. For larger values of λ more emphasis is put on the regularization term and both methods display knee-points at which the reconstruction level drops significantly. The λ value at which this point occurs seems to depend on both frequency and signal-to-noise ratio.

The stronger the source, the larger is λ at the knee-point. This behaviour is in line with one of the main drawbacks of ℓ_1 -norm regularization: When λ increases, the source distribution becomes increasingly more sparse and sound power is aggregated around fewer points. The

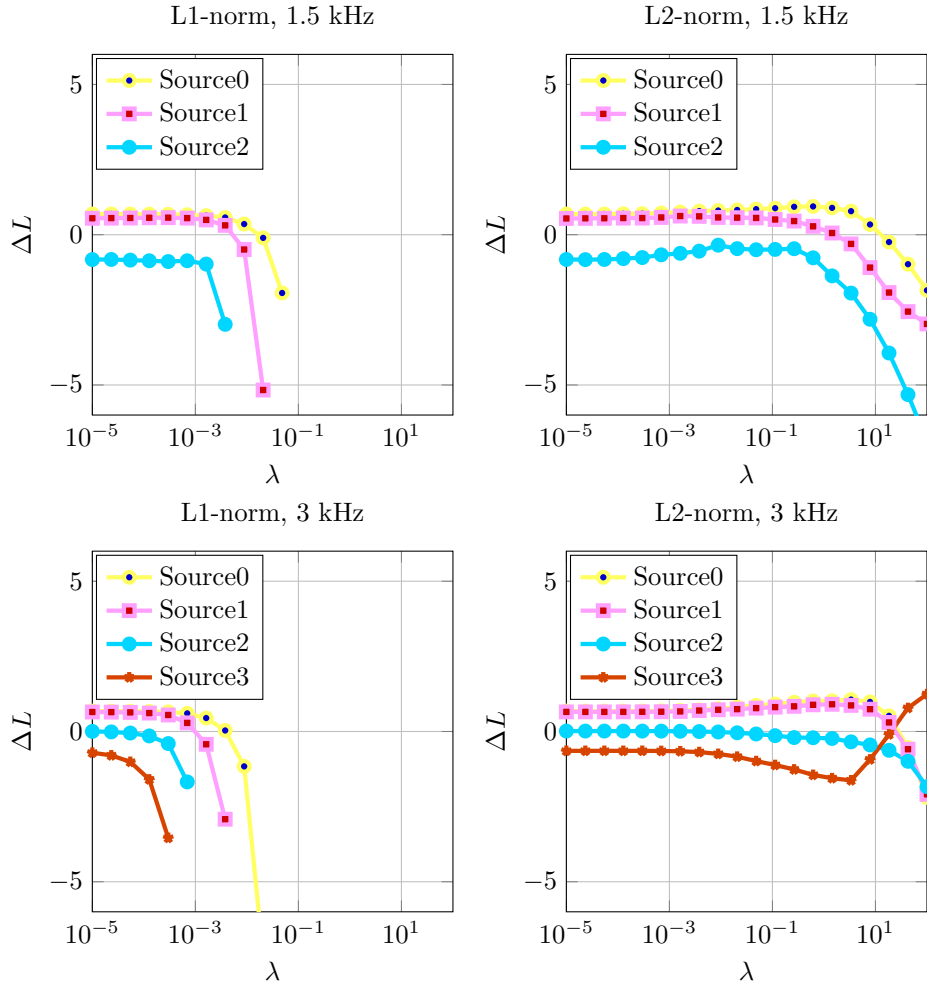


Figure 8: Case II: Level differences for the four sources at $f = 1500$ Hz (above) and $f = 3000$ Hz (below) as function of λ .

sound power of the weakest sources is absorbed into the stronger ones.

Increasing the frequency seems to move the knee-point towards lower λ . This pattern is most clear for ℓ_1 -norm regularization. One possible explanation for the behaviour has to do with the complexity of the underlying model, i.e., point-spread function. The width of the mainlobe of the point-spread function increases as the frequency decreases. This means, that the number of linearly independent rows/columns in the point-spread function, i.e., matrix rank, decrease with frequency, thus the complexity decreases. With lower complexity, a larger regularization is required to induce sparsity.

Using the reference levels from the data set, optimal regularization parameters can be found from the reconstructions. The optimal λ is determined for each frequency to be the largest one that gives a reconstruction level within ± 2 dB of the reference, $|\Delta L| < 2$ dB. These values are shown in Fig. 9 for the two regularization methods. The behaviour of the ℓ_1 -norm method is in line with the observation from Fig. 8: λ increases with decreasing frequency and a clear divide is seen between the sources. The ℓ_1 -norm regularization can reconstruct absolute noise levels

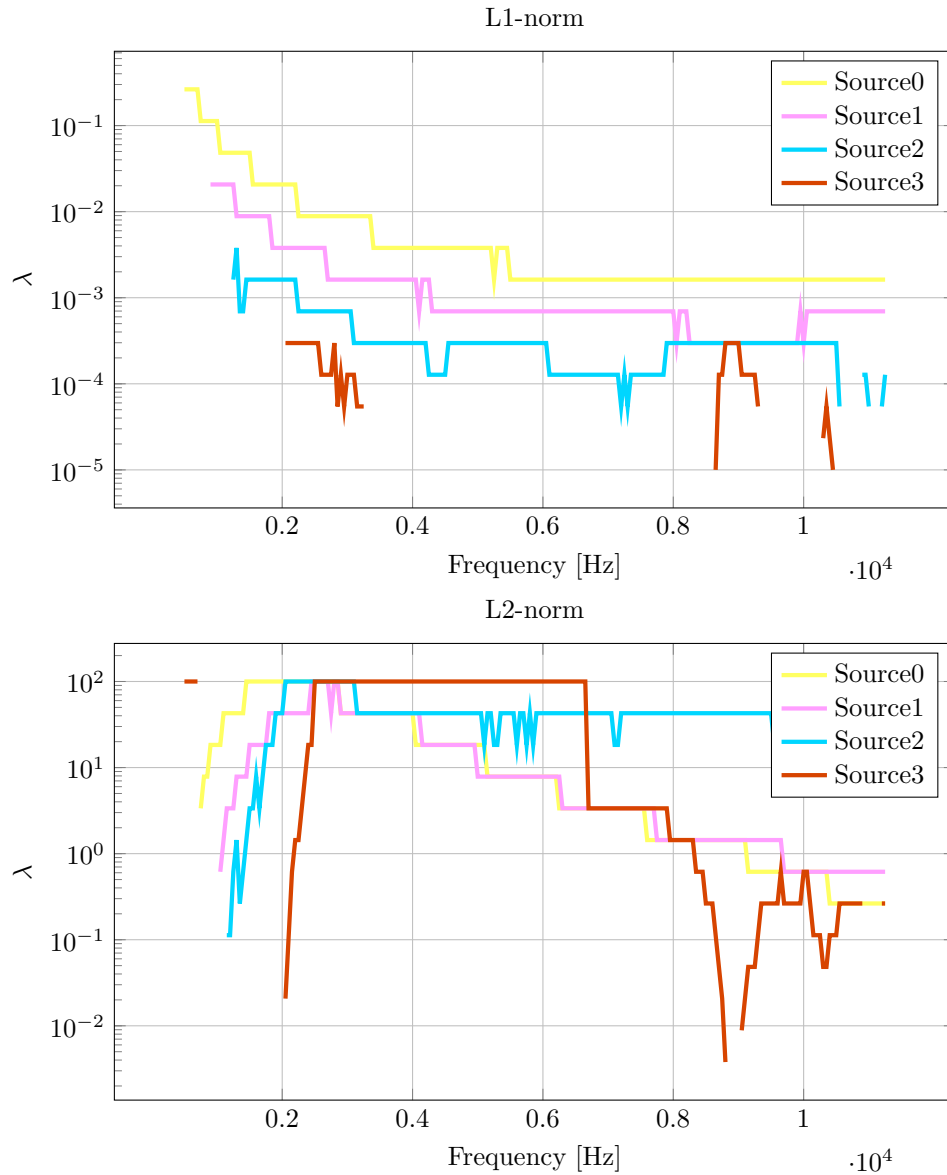


Figure 9: Case II: Optimal λ values as function of frequency for ℓ_1 -norm (above) and ℓ_2 -norm (below).

within ± 2 dB for all but the weakest source in the range from 500 Hz to approximately 10 kHz. The ℓ_2 -norm regularization seems better at reconstructing absolute levels for the weakest source, however, by inspection of the deconvolved maps (omitted here for brevity), the resolution is very low and not useful for source localization.

4. CONCLUSIONS

Absolute noise levels have been reconstructed with beamforming deconvolution and the effects of boundary conditions and regularization have been evaluated against the reference levels.

Seven different boundary conditions have been applied, six of them commonly seen in the deblurring literature, and it has been found that they all give rise to good reconstructions of absolute noise levels within ± 1 dB of the reference. A lower frequency limit has been proposed, based on the Rayleigh criterion, below which deconvolution fails to reconstruct the source distribution. The results indicate that the use of an extended BC extends the frequency range in which deconvolution can successfully be applied at low frequencies.

Two common regularization terms have been investigated and the importance of a correctly chosen regularization parameter has been reviewed. Specifically, the ℓ_1 -norm regularization has been observed to have a clear dependency on frequency and signal-to-noise ratio. Further investigations are required before a general recommendation for regularization parameter estimation can be derived.

This study has been based on results generated by a single deconvolution algorithm using a single data set. Using the same methodology as presented, future investigations should take into account other algorithms and data sets to get a more general picture of boundary and regularization effects on the noise quantification problem.

A. Appendix

Reflect									Replicate								
5	6	5	4	5	6	5	4	5	1	1	1	1	2	3	3	3	3
8	9	8	7	8	9	8	7	8	1	1	1	1	2	3	3	3	3
5	6	5	4	5	6	5	4	5	1	1	1	1	2	3	3	3	3
2	3	2	1	2	3	2	1	2	1	1	1	1	2	3	3	3	3
5	6	5	4	5	6	5	4	5	4	4	4	4	5	6	6	6	6
8	9	8	7	8	9	8	7	8	7	7	7	7	8	9	9	9	9
5	6	5	4	5	6	5	4	5	7	7	7	7	8	9	9	9	9
2	3	2	1	2	3	2	1	2	7	7	7	7	8	9	9	9	9
5	6	5	4	5	6	5	4	5	7	7	7	7	8	9	9	9	9

Symmetric									Periodic								
9	8	7	7	8	9	9	8	7	1	2	3	1	2	3	1	2	3
6	5	4	4	5	6	6	5	4	4	5	6	4	5	6	4	5	6
3	2	1	1	2	3	3	2	1	7	8	9	7	8	9	7	8	9
3	2	1	1	2	3	3	2	1	1	2	3	1	2	3	1	2	3
6	5	4	4	5	6	6	5	4	4	5	6	4	5	6	4	5	6
9	8	7	7	8	9	9	8	7	7	8	9	7	8	9	7	8	9
9	8	7	7	8	9	9	8	7	1	2	3	1	2	3	1	2	3
6	5	4	4	5	6	6	5	4	4	5	6	4	5	6	4	5	6
3	2	1	1	2	3	3	2	1	7	8	9	7	8	9	7	8	9

Figure 10: Common boundary conditions imposed on matrix \mathbf{X} .

References

- [1] J. Hald. “Beamforming and Wavenumber Processing”. *Handbook of Signal Processing in Acoustics*. Ed. by D. Havelock, S. Kuwano, and M. Vorländer. New York, NY: Springer New York, 2008, pp. 131–144. DOI: 10.1007/978-0-387-30441-0_9.
- [2] K. Ehrenfried and L. Koop. “Comparison of Iterative Deconvolution Algorithms for the Mapping of Acoustic Sources”. *AIAA Journal* 45.7 (2007), pp. 1584–1595. DOI: 10.2514/1.26320.
- [3] T. F. Brooks and W. M. Humphreys. “A deconvolution approach for the mapping of acoustic sources (DAMAS) determined from phased microphone arrays”. *Journal of Sound and Vibration* 294.4-5 (2006), pp. 856–879.
- [4] J. A. Högbom. “Aperture synthesis with a non-regular distribution of interferometer baselines”. *Astronomy and Astrophysics Supplement Series* 15.3 (1974), pp. 417–426.
- [5] C. Lawson and R. Hanson. *Solving Least Squares Problems*. Society for Industrial and Applied Mathematics, 1995. DOI: 10.1137/1.9781611971217.
- [6] W. H. Richardson. “Bayesian-based iterative method of image restoration”. *Journal of the Optical Society of America* 62.1 (1972), pp. 55–59.
- [7] L. B. Lucy. “An iterative technique for the rectification of observed distributions”. *Astronomical Journal* 79 (1974), p. 745.
- [8] T. Yardibi et al. “Comparison of Microphone Array Processing Techniques for Aeroacoustic Measurements”. *International Journal of Aeroacoustics* 9.6 (2010), pp. 733–761. DOI: 10.1260/1475-472X.9.6.733.
- [9] Z. Chu and Y. Yang. “Comparison of deconvolution methods for the visualization of acoustic sources based on cross-spectral imaging function beamforming”. *Mechanical Systems and Signal Processing* 48.1 (2014), pp. 404–422. DOI: 10.1016/j.ymssp.2014.03.012.
- [10] Q. Leclère. “A Unified Formalism For Acoustic Imaging Techniques: Illustrations in the Frame of a Didactic Numerical Benchmark”. *Proceedings of the 6th Berlin Beamforming Conference*. Feb. 2016.
- [11] Å. Björck. *Numerical Methods for Least Squares Problems*. Society for Industrial and Applied Mathematics, 1996. DOI: 10.1137/1.9781611971484.
- [12] P. Hansen. *Discrete Inverse Problems*. Society for Industrial and Applied Mathematics, 2010. DOI: 10.1137/1.9780898718836.
- [13] O. Lylloff et al. “Improving the efficiency of deconvolution algorithms for sound source localization”. *Journal of the Acoustical Society of America* 138.1 (2015), pp. 172–180. DOI: 10.1121/1.4922516.
- [14] “Periodic boundary based FFT-FISTA for sound source identification”. *Applied Acoustics* 130 (2018), pp. 87–91. DOI: 10.1016/j.apacoust.2017.09.009.
- [15] L. Hoeltgen et al. “Sparse l1 Regularisation of Matrix Valued Models for Acoustic Source Characterisation”. *arXiv.org* (July 2016). arXiv: 1607.00171v1.

- [16] J. Antoni. “A Bayesian approach to sound source reconstruction: Optimal basis, regularization, and focusing”. *The Journal of the Acoustical Society of America* 131.4 (2012), pp. 2873–2890. DOI: 10.1121/1.3685484.
- [17] A. Xenaki, P. Gerstoft, and K. Mosegaard. “Compressive beamforming”. *The Journal of the Acoustical Society of America* 136.1 (2014), pp. 260–271. DOI: 10.1121/1.4883360.
- [18] X. Li, W. Tong, and M. Jiang. “Sound Source Localizarion Via Elastic Net Regularization”. *Proceedings of the 5th Berlin Beamforming Conference*. 2014.
- [19] *Benchmarking Array Analysis Methods*. 2018. URL: <https://www.b-tu.de/fg-akustik/lehre/aktuelles/arraybenchmark> (visited on 03/04/2018).
- [20] E. Sarradj et al. “A Microphone Array Method Benchmarking Exercise using Synthesized Input Data”. June 2017.
- [21] C. J. Bahr et al. “A Comparison of Microphone Phased Array Methods Applied to the Study of Airframe Noise in Wind Tunnel Testing”. *23rd AIAA/CEAS Aeroacoustics Conference*. Reston, Virginia: American Institute of Aeronautics and Astronautics, June 2017, pp. 1–19.
- [22] A. Beck and M. Teboulle. “A Fast Iterative Shrinkage-Thresholding Algorithm for Linear Inverse Problems”. *SIAM Journal on Imaging Sciences* 2.1 (Jan. 2009), pp. 183–202.
- [23] N. Parikh and S. Boyd. “Proximal Algorithms”. *Foundations and Trends in Optimization* 1 (Aug. 2013), pp. 123–231.
- [24] O. Lylloff and E. Fernandez-Grande. *Noise Quantification with Beamforming Deconvolution: Effects of Regularization and Boundary Conditions - reproducible research steps*. 2018. URL: <https://gitlab.windenergy.dtu.dk/ollyl/BeBeC18> (visited on 03/04/2018).
- [25] F. Jacobsen and P. M. Juhl. *Fundamentals of general linear acoustics*. Wiley, 2013.
- [26] E. Sarradj. “Three-Dimensional Acoustic Source Mapping with Different Beamforming Steering Vector Formulations”. *Advances in Acoustics and Vibration* 2012.4 (2012), pp. 1–12. DOI: 10.1155/2012/292695.
- [27] J. D. Maynard, E. G. Williams, and Y. Lee. “Nearfield acoustic holography: I. Theory of generalized holography and the development of NAH”. *Journal of the Acoustical Society of America* 78 (1985), pp. 1395–1413.
- [28] S. P. Boyd and L. Vandenberghe. *Convex optimization*. Cambridge university press, 2004.
- [29] A. N. Tikhonov and V. Y. Arsenin. *Solutions of ILL-Posed Problems*. V.H. Winston & Sons, 1977.
- [30] R. Tibshirani. “Regression Shrinkage and Selection via the Lasso”. *Journal of the Royal Statistical Society. Series B (Methodological)* 58.1 (1996), pp. 267–288.
- [31] A. Xenaki, E. Fernandez-Grande, and P. Gerstoft. “Block-sparse beamforming for spatially extended sources in a Bayesian formulation”. *Journal of the Acoustical Society of America* 140.3 (Sept. 2016), pp. 1828–1838. DOI: 10.1121/1.4962325.

- [32] Z. Chu et al. “Improvement of Fourier-based fast iterative shrinkage-thresholding deconvolution algorithm for acoustic source identification”. *Applied Acoustics* 123 (2017), pp. 64–72. DOI: 10.1016/j.apacoust.2017.03.010.
- [33] P. Hansen, J. Nagy, and D. O’Leary. *Deblurring Images*. Society for Industrial and Applied Mathematics, 2006. DOI: 10.1137/1.9780898718874.
- [34] J. Hald and J. J. Christensen. “Technical Review: Beamforming, No. 1”. *Brüel & Kjaer* (2004).
- [35] M. Aldeman et al. “Effects of Array Scaling and Advanced Beamforming on the Angular Resolution of Microphone Array Systems”. *Proceedings of the 6th Berlin Beamforming Conference*. 2016.

Paper C

Submitted for publication.

Acoustic level corrections for a Kevlar-walled wind tunnel

Oliver Lylloff^{*1}, Andreas Fischer¹, Christian Bak¹, and Efren Fernandez Grande²

¹DTU Wind Energy
Technical University of Denmark (DTU)
Frederiksborgvej 399
DK-4000 Roskilde, Denmark.
²DTU Electrical Engineering
Technical University of Denmark (DTU)
Ørsteds Plads
DK-2800 Kongens Lyngby, Denmark.

November 14, 2020

Abstract

Accurately estimating noise spectra of airfoils in a wind tunnel depends on the degree of knowledge on the sound propagation path between airfoil and acoustic measurement equipment. In Kevlar-walled wind tunnels, where the flow is contained by walls of tensioned Kevlar, the propagation path traverses a turbulent boundary layer and tensioned Kevlar fabric before reaching the microphones, which affects the measured sound pressure level. In addition, corrections for flow convection and refraction are required to reliably use a phased microphone array for estimating the noise spectra. In this paper, an analytical correction scheme is derived for the refraction of sound when propagating through two shear layers, based on a ray tracing method introduced by Amiet. With this correction, a microphone array is used to obtain the noise spectra of a reference source with known sound power level across a wind tunnel test section and two Kevlar walls. The Kevlar insertion loss and amplitude attenuation, associated with the turbulent boundary layer, are determined experimentally. The Kevlar loss is found to increase with frequency, and the turbulent boundary layer loss is found to scale linearly with flow velocity. A comparison with previous studies at other facilities are conducted and discussed.

1 Introduction

The majority of aeroacoustic wind tunnels have either an open jet test section or a closed test section [1]. In the closed test section, where the flow is contained with rigid walls, microphones

^{*}Corresponding Author: OLLYL@DTU.DK

are typically mounted in the tunnel walls, where they are exposed to strong pressure fluctuations due to boundary layer turbulence. The open jet test section, allows for microphones to be placed outside the flow, however, the open jet exhibit a different aerodynamic behavior. In both cases, the sound propagation path must pass either a free shear layer (open jet) or turbulent boundary layer (closed test section) [1]. Kevlar fabric has been studied over the last two decades as a compromise between the two types of setup [2]. The so-called hybrid wind tunnel was first introduced in [3, 4], which showed promise of combining the benefits of the open jet and closed test sections, while circumventing their respective drawbacks. In the hybrid wind tunnel, hard test section walls are replaced by tensioned Kevlar cloth, that allows sound to be transmitted to microphones situated outside the flow, while containing a steady flow inside the test section. Recently, several research facilities have adopted the hybrid test section by either placing Kevlar panels in front of the acoustic equipment in their open jet configuration or by constructing Kevlar side walls [5, 6, 7, 8, 9].

One standing issue with the hybrid test section, however, is the lack of a method to estimate reliably the acoustic losses due to propagation through the shear layer, the Kevlar sheet and the turbulent boundary layer that develops on top of the Kevlar sheet. In [3], a loudspeaker and a microphone array, placed on opposite sides of a Kevlar walled test section, are used to estimate the Kevlar insertion loss (IL) and turbulent boundary layer loss. The Kevlar IL results show large fluctuations and a curve fit is found. The turbulent boundary layer loss is obtained via source integration of beamforming maps at 5 different flow speeds, an a quadratic velocity scaling is found. A different method comes from development of an acoustic non-intrusive laser pulse source [10, 11, 12] that has led to studies on Kevlar losses [13, 6, 14]. These studies used a laser to generate an acoustic pulse source in the center of their wind tunnel test sections. In [13], transfer functions of amplitude and phase are determined per microphone basis to account for possible phase changes due to the impedance of Kevlar. The results indicate, that the phase changes are smooth as function of frequency, which means, that a beamforming approach, that makes use of the phase delay between microphones, can still be used.

This study proposes a non-intrusive method, inspired by the approach proposed in [3] (and similarly in [8, 9]), by placing a reference source outside the test section. Making use of a commercially available extension to the source, the volume velocity and hence sound power level of the source can be determined [15, 16]. Using the reference level of the loudspeaker, a microphone array placed opposite of the test section is used to estimate the source power by Delay-and-Sum (DAS) beamforming [17] with source integration [18]. The beamforming maps are corrected for shear layer effects in terms of travelling time between source and receiver and amplitude of the transmitted pressure. The corrections are derived by using a ray tracing method as proposed by Amiet [19] for a single shear layer extended to two shear layers. The discrepancy between the reference and the measured pressure level is due to the Kevlar IL (at zero flow) and losses due to decorrelation during the transmission through the turbulent boundary layer (TBL), TBL loss. In this point, the proposed method of this study differs from previous and similar approaches. In [3], for instance, a shear layer correction accounting for a single wall is used. The authors remark, that the error is expected to be small [3]. The risk of this, is that shear layer effects are mixed together with Kevlar IL and TBL loss, potentially applying the same correction twice, both empirically and analytically. In this study, the shear layer effects

are isolated in the correction scheme, derived from Amiet, and the Kevlar IL and TBL loss can be estimated empirically.

The paper is structured as follows. In Section 2 the derivation of a phase and amplitude correction for two shear layers is given and the experimental method and setup is described. The results are presented in Section 3 and discussed in Section 4. The paper is concluded in Section 5.

2 Methods

In this section, a correction scheme is described that corrects the transmission time and amplitude of the sound pressure for the effects of refraction on two shear layers. It is assumed, that the effect of shear layer refraction can be separated from Kevlar IL and decorrelation through the turbulent boundary layers, TBL loss. The effects of Kevlar IL and TBL loss will be determined experimentally. In the second part of this section the experimental setup is presented.

2.1 Correction for two shear layers

Due to the presence of flow in the test section, the sound field is altered during the propagation from source to receiver. A ray tracing procedure according to the method proposed by Amiet [19] is implemented to correct for shear layer refraction and convection of the sound in the test section. The ray path of a sound wave from the source position S to the microphone position M is sketched in Figure 1 (in blue). It is assumed that the shear layers are infinitely thin and are located in the plane of the Kevlar sheet. The shear layer correction needs to be 3 dimensional, since it is applied for each grid point in the source plane to each microphone of the microphone array. Due to the flow in the tunnel a spherical sound wave gets distorted. It is advantageous to consider the point S' when deriving the correction model. S' is the apparent center of the spherical wave that travels with the speed of sound c_0 . The ray path, from S' to M, of this spherical wave is shown in Figure 1 (in red). Snell's law for shear layer refraction has been derived in 2 dimensions by Ribner [20] and was extended to 3 dimensions in [21]. The development of a correction for two shear layers is initiated from [21, Eq. 10.2.8] and is valid for a spherical sound wave emitted from S'. It reads

$$\sin \beta = \frac{\sin \alpha}{1 - M_\infty \sin \alpha \cos \psi} \quad (1)$$

$$\psi_i = \psi_t = \psi \quad (2)$$

where $\alpha = \pi/2 - \phi_t$ and $\beta = \pi/2 - \phi_i$ to recover the original notation in [21]. It describes the refraction on the second shear layer in point 2 in Figure 1. By further investigation of Snell's law, it can be shown, that the angle of incident sound wave in point 1 is equal to the angle of the transmitted sound wave α in point 2. Using Eq. (1) and (2), the geometrical relations follows

$$\Delta x_1 = \Delta z_1 \frac{ab}{\sqrt{1 - a^2}} \quad (3)$$

The variables a and b are unknown. In order to obtain these variables, the following system of equations is solved numerically,

$$\begin{aligned}\Delta x_1 + \Delta x_{20} + \Delta x_{21} + \Delta x_3 - \Delta x_m &= 0 \\ b - \frac{\Delta x_1 - \Delta x_m}{\sqrt{(\Delta x_1 - \Delta x_m)^2 + \Delta y_m^2}} &= 0\end{aligned}\quad (7)$$

in the domain $0 < a < 0.8$ and $-1 < b < 1$. This first part of the correction addresses the propagation time. When formulating the steering vectors in DAS beamforming, it is assumed that the sound waves take the direct path from the source to the microphone. Hence, a propagation time correction is defined as the ratio of the actual travel time along the path depicted in figure 1 and the travel time of a sound wave along the direct path in a homogeneous medium without flow. Considering the source point S' , the fictive propagation speed of the sound wave is equal to the propagation speed in a free field and the time correction simply becomes the ratio of the ray path length from S' to M and the direct path from S to M . The correction factor reads

$$c_t = \frac{r}{r_m} \quad (8)$$

where

$$r = r_1 + r_2 + r_3 \quad (9)$$

with

$$\begin{aligned}r_1 &= \Delta z_1 \frac{1}{\sqrt{1-a^2}} \\ r_2 &= \Delta z_2 \frac{1 - M_\infty ab}{\xi} \\ r_3 &= \Delta z_3 \frac{1}{\sqrt{1-a^2}}.\end{aligned}\quad (10)$$

and $r_m = \sqrt{\Delta x_m^2 + \Delta y_m^2 + \Delta z_m^2}$.

Further, a correction of the amplitude is necessary. The correction is defined such that it relates the amplitude of the pressure that would be measured at the microphone position if there was no flow to the amplitude that is measured with flow. This is a different approach compared to the classical Amiet correction, as the present correction intends to "switch off the flow in the tunnel" while the Amiet correction "extends the flow to the array position".

The amplitude correction scheme reads

$$\left| \frac{\hat{p}_{m0}}{\hat{p}_m} \right|^2 = \left| \frac{\hat{p}_{m0}}{\hat{p}_{i1}} \right|^2 \left| \frac{\hat{p}_{i1}}{\hat{p}_{t1}} \right|^2 \left| \frac{\hat{p}_{t1}}{\hat{p}_{i2}} \right|^2 \left| \frac{\hat{p}_{i2}}{\hat{p}_{t2}} \right|^2 \left| \frac{\hat{p}_{t2}}{\hat{p}_m} \right|^2. \quad (11)$$

\hat{p}_{m0} is the pressure that would be measured in the absence of flow in the tunnel and \hat{p}_m is the actually measured pressure. \hat{p}_{i1} is the pressure incident at point 1' and \hat{p}_{t1} the pressure transmitted into the tunnel at point 1'. \hat{p}_{i2} is the pressure incident at point 2 and \hat{p}_{t1} the pressure transmitted out of the tunnel. The first term of the correction scheme accounts for the geometric

spreading of a spherical sound wave in free field by the distance S to 1 compared to the distance S to M. It reads

$$\left| \frac{\hat{p}_{m0}}{\hat{p}_{i1}} \right|^2 = \frac{r_1^2}{r_m^2}. \quad (12)$$

The angle of incidence from S to 1 is different than the angle of incidence from S to M. Directivity effects are neglected in Eq. (12). Hence, it strictly holds only for a monopole point source.

The terms $\left| \frac{\hat{p}_{i1}}{\hat{p}_{t1}} \right|^2$ and $\left| \frac{\hat{p}_{i2}}{\hat{p}_{t2}} \right|^2$ relate to the transmission through the shear layer. The transmission coefficient T , which defines the ratio of the transmitted to the incident pressure, was first derived by Ribner in 2D [20] and by Glegg et al. in 3D [21]. Starting from [21, Eq. 10.2.14], the following expression results after some manipulation:

$$\left| \frac{\hat{p}_{i1,2}}{\hat{p}_{t1,2}} \right|^2 = \frac{1}{T_{1,2}^2}, \quad T_{1,2} = \frac{2}{1 + Z_{1,2}} \quad (13)$$

with

$$Z_1 = \frac{\xi}{\sqrt{1 - a^2}} \frac{1}{(1 - M_\infty ab)^2}, \quad Z_2 = \frac{1}{Z_1}. \quad (14)$$

The remaining terms $\left| \frac{\hat{p}_{t1}}{\hat{p}_{i2}} \right|^2$ and $\left| \frac{\hat{p}_{t2}}{\hat{p}_m} \right|^2$ relate to geometrical spreading and distortion through refraction of the sound wave,

$$\left| \frac{\hat{p}_{t1}}{\hat{p}_{i2}} \right|^2 \left| \frac{\hat{p}_{t2}}{\hat{p}_m} \right|^2 = \frac{dS_2}{dS_1} \frac{dS_3}{dS_2} = \frac{dS_3}{dS_1}. \quad (15)$$

dS_j is the differential surface area of the sound wave at point j . The differential surface area can be computed as

$$dS_j = |t_{\alpha,j} \times t_{\psi,j}| d\alpha d\psi. \quad (16)$$

The tangent vectors are defined as

$$t_{\alpha,j} = \begin{bmatrix} \frac{\partial x_j(\alpha, \psi)}{\partial \alpha} \\ \frac{\partial y_j(\alpha, \psi)}{\partial \alpha} \\ \frac{\partial z_j(\alpha, \psi)}{\partial \alpha} \end{bmatrix} \quad (17)$$

and

$$t_{\psi,j} = \begin{bmatrix} \frac{\partial x_j(\alpha, \psi)}{\partial \psi} \\ \frac{\partial y_j(\alpha, \psi)}{\partial \psi} \\ \frac{\partial z_j(\alpha, \psi)}{\partial \psi} \end{bmatrix}. \quad (18)$$

The parametric coordinates of Point 1 are

$$\begin{aligned} x_1 &= r_1 \sin \alpha \cos \psi \\ y_1 &= r_1 \sin \alpha \sin \psi \\ z_1 &= r_1 \cos \alpha. \end{aligned}$$

and parametric coordinates of Point M are

$$\begin{aligned}x_3 &= (r_1 + r_3) \sin \alpha \cos \psi + r_2 \sin \beta \cos \psi + r_2 M_\infty \\y_3 &= (r_1 + r_3) \sin \alpha \sin \psi + r_2 \sin \beta \sin \psi \\z_3 &= (r_1 + r_3) \cos \alpha + r_2 \cos \beta.\end{aligned}$$

After some calculation, the following expression arise

$$\frac{dS_3}{dS_1} = \frac{RK}{r_1^2} \quad (19)$$

with

$$K = \sqrt{a^2 \left[D \frac{\sqrt{1-a^2}}{\xi} (1-b^2) + A \left(b - \frac{D}{R} \right) \right]^2 + a^2 (1-b^2) \left[A - D \frac{\sqrt{1-a^2}}{\xi} b \right]^2 + (1-a^2) (R - Db)^2} \quad (20)$$

where the introduced variables are

$$\begin{aligned}R &= r_1 + r_3 + \frac{r_2}{d^2} \\A &= r_1 + r_3 + \frac{\sqrt{1-a^2}}{\xi} \frac{r_2}{d^2} \\D &= \frac{r_2}{d^2} M_\infty a,\end{aligned}$$

where d and ξ was defined in Eq. (4). These equations constitute the amplitude correction scheme. An illustration of the sound propagation path through two shear layers is shown in Fig. 2, and correction examples are shown in Fig. 3.

2.2 Experimental setup

This study was conducted in the newly-commissioned Poul la Cour Tunnel (PLCT), situated at the Wind Energy Department of the Technical University of Denmark. PLCT is an anechoic closed-loop wind tunnel dedicated to wind energy research. The flow is driven by a 2.4 MW fan and a maximum speed of 105 m/s can be achieved. The test section has a cross section of 2×3 m and is 9 m long. The walls of the test section can be exchanged between aerodynamic hard walls and aeroacoustic Kevlar walls. The Kevlar walls are 6 m long and cover the part of the test section which begins 1 m downstream of the contraction. The test section is surrounded by an anechoic chamber which has a lower frequency limit of 100 Hz (setup shown in Fig. 4). The Kevlar fabric is a custom weave with characteristics given in Table 1. The density of this Kevlar type is slightly higher than what was reported in previous studies with densities in the range 58 g/m²-61 g/m² [3, 13, 6]. The open-area-ratio (OAR) was estimated experimentally to 2%. The estimation of losses due to Kevlar and turbulent boundary layer noise was conducted in the test section of PLCT.

A reference source loudspeaker (B&K Omnisource Type 4295) with volume velocity extension hose (B&K Type 4299), was placed outside the test section facing into it, at a distance of

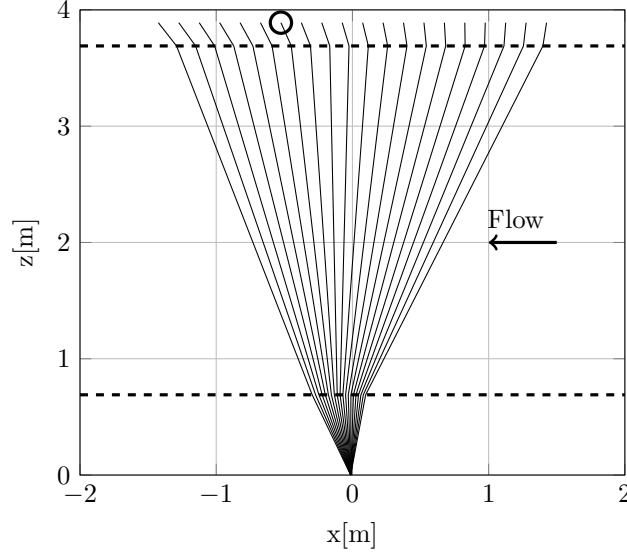


Figure 2: Sound rays propagation paths from source plane (at top) to a microphone (at origo). Loudspeaker placement of current method is shown with a circle and Kevlar walls in dashed. Flow speed is $U_0 = 70$ m/s.

Table 1: Custom Style Kevlar 120

Setting warp	15.0 Thr/cm
Setting weft	15.0 Thr/cm
Fabric	Kevlar 49 T965 (215 dtex)
Weight	ca. 68 g/m ²
OAR	0.02

20 cm from the Kevlar wall and 0.8 m above the tunnel floor. The loudspeaker was connected to an amplifier and noise generator (B&K Type 2734). On the opposite side of the test section, an 84-microphone array (with 1/4 inch microphones B&K Type 4985) is placed facing into the test section, at a distance of 0.69 m to the Kevlar. The measurement campaign consisted of 16 measurements of each 20 s; 8 background noise measurements with the loudspeaker switched off, and 8 measurements with white noise driving the loudspeaker in frequency range of 50 Hz-5000 Hz. The output level was set to the highest possible without audible distortion. The flow speeds were the same for the two series: $U_0 = 0.0, 8.5, 18.5, 28.5, 38.5, 48.5, 59.0, 69.3$ m/s. Each measurement was further processed into cross-spectral matrices (CSM) using Welch's method [22], a Hanning window of 16384 samples was used with 50% overlap, which results in a frequency resolution of 4 Hz. The data was further compressed by summation into 1/12th octave bands. The Delay-and-sum (DAS) [17] beamforming techniques was applied, using steering vectors that account for the time and amplitude correction derived in Sec. 2.1. The sound pressure level of the loudspeaker, at the center of the microphone array, was determined from integrated spectra of beamforming maps using an integration region of 1×1 m and compensating for the

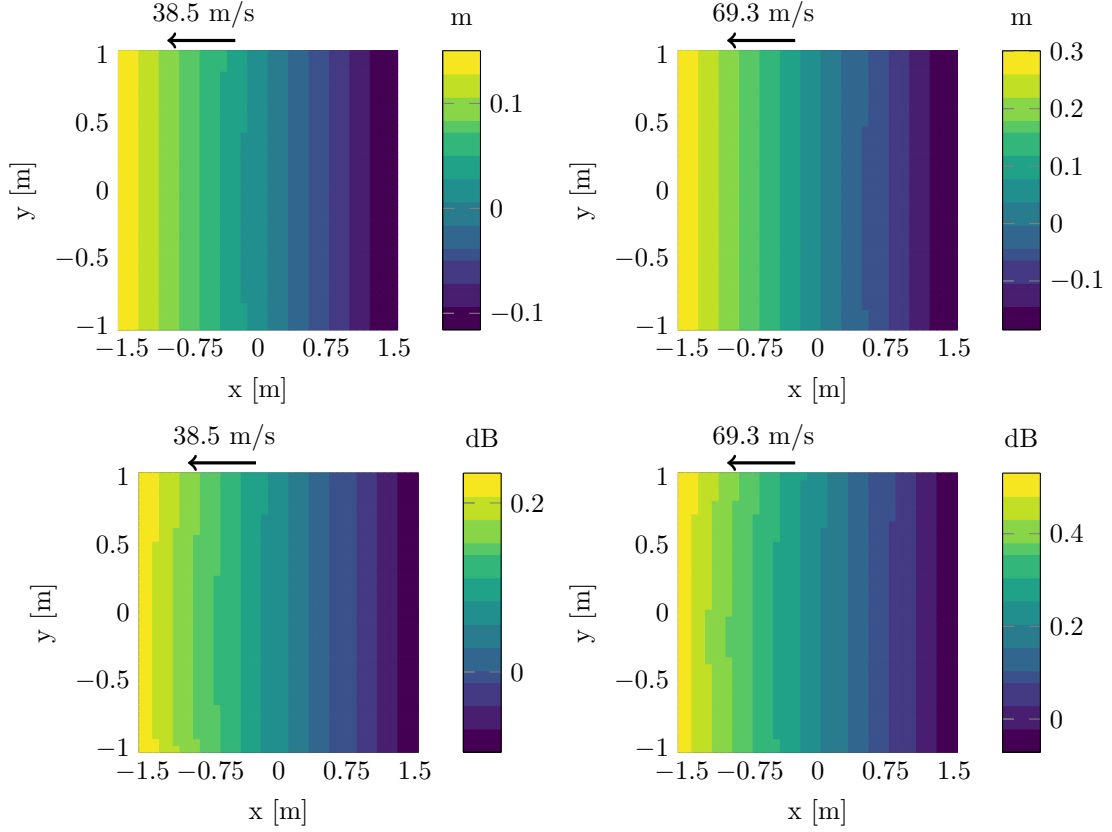


Figure 3: Refraction corrections for propagation path relative to free-field propagation (top) and amplitude correction (bottom) for two shear layers.

array response (point-spread function) by the method described in [18].

The zero-flow case ($U_0 = 0$ m/s) was used to determine the loss due to Kevlar IL as the level difference between the loudspeaker sound power level and the integrated spectra obtained with the microphone array. The reference level of the loudspeaker was determined from the volume velocity [15, 16] and propagated to the center of the microphone array using a free-field assumption. The lower frequency limit of the proposed method is approximately 500 Hz due to the array aperture size and bias due to floor and ceiling interference. The higher frequency limit is approximately 6 kHz, limited by the frequency range of the noise generator and higher order modes in the attached extension hose.

The TBL loss was determined at each flow speed ($U_0 > 0$ m/s), and a traditional background noise subtraction was applied by direct matrix subtraction of the background noise CSMs (measurement series with loudspeaker switched off) from the CSMs of the loudspeaker measurement series. The TBL loss, at a given flow speed, was estimated by the difference between the DAS integrated spectra at $U_0 = 0$ m/s and at the given flow speed.

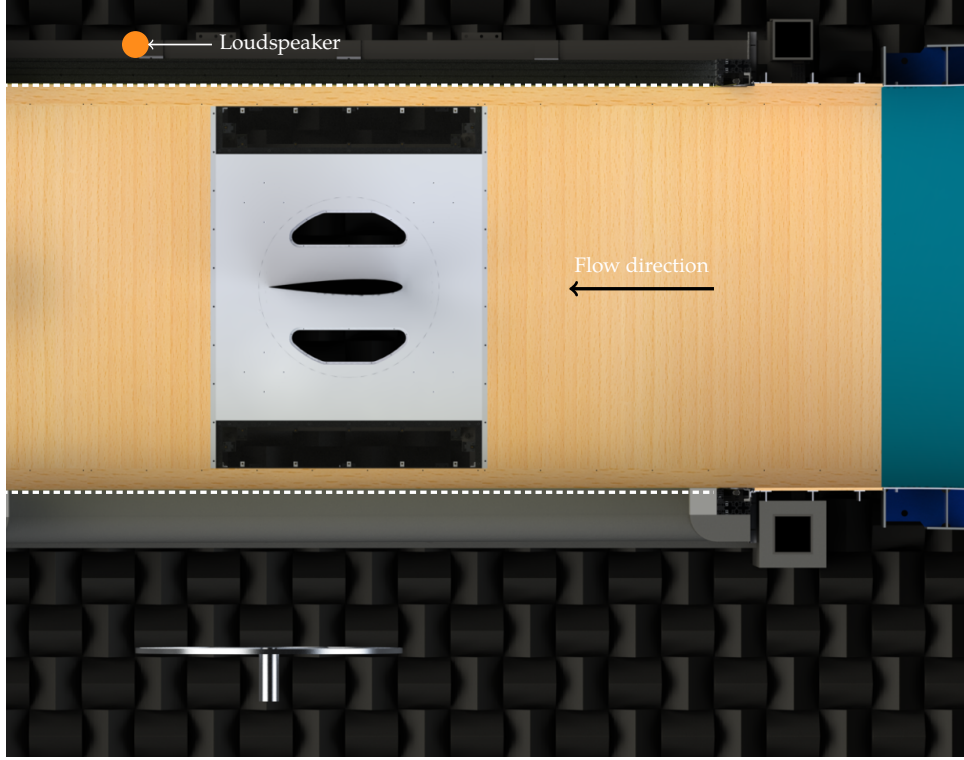


Figure 4: Experimental setup in wind tunnel test section. Loudspeaker placement is shown with a dot, Kevlar walls in dashed, microphone array in the bottom, and flow direction is right to left. The test section was empty during the measurement campaign.

3 Results

3.1 Kevlar loss

The Kevlar IL (no flow case) is shown in Fig. 5 (bottom plot) as narrowband data. A constant increase in Kevlar IL is seen from 500 Hz to 2000 Hz, with the exception of a peak around 600 Hz. This peak is not a characteristic of the Kevlar, but due to an interference pattern clearly visible in Fig. 5 below 1000 Hz. Additionally, the spatial resolution of beamforming can be estimated by the Rayleigh criterion, $R = z_0 \cdot c_0 / (D \cdot f)$, where z_0 is the measurement distance, c_0 the speed of sound, D the microphone array diameter (2 m), and f the frequency [23, 24]. This gives a resolution of 0.4 m at 1000 Hz. This means, that reflections from floor and ceiling, will be increasingly difficult to distinguish from the reference source towards lower frequencies. Figure. 6 shows four beamforming maps below 1000 Hz. Reflections from floor and ceiling are seen to gradually move into the integration region with decreasing frequency. A reliable lower frequency limit is approximately 1000 Hz, where the Kevlar IL is below 1 dB, increasing to 2 dB at 2000 Hz. This is in line with previous studies [3, 6, 13], although slightly higher. Above 2000 Hz, the Kevlar IL drops off and becomes negative above 4000 Hz. This is not expected to be

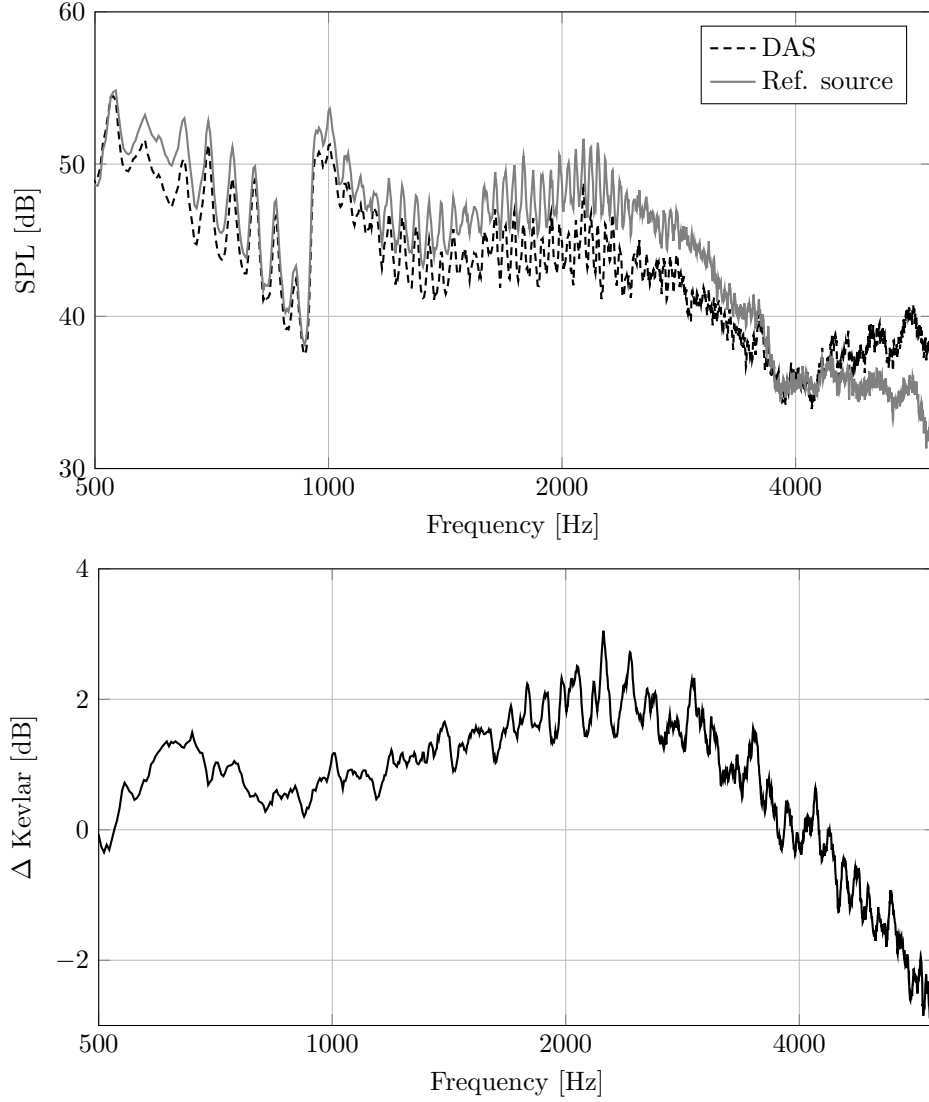


Figure 5: Top: Sound pressure level (SPL) of integrated delay-and-sum (DAS) beamforming map, at zero flow, at the center of the microphone array, compared to reference level from volume velocity source (Ref. source). Bottom: Kevlar IL (ΔKevlar) of one wall.

a physical characteristic of Kevlar. The lack of agreement is due to the volume velocity source. As it is mentioned in [16], the first higher order modes in the extension hose can propagate above 5 kHz, however, the placement of the microphones in the extension hose allows for this mode to be undetected, and first at 10.5 kHz is the first mode measured. The microphone array, however, will detect the higher order modes above 5 kHz and cause a discrepancy between the reference level and DAS integrated spectra, resulting in a negative Kevlar IL. Since a decrease in Kevlar IL is seen already in the range 2000 Hz-4000 Hz, this behavior is presumably due to

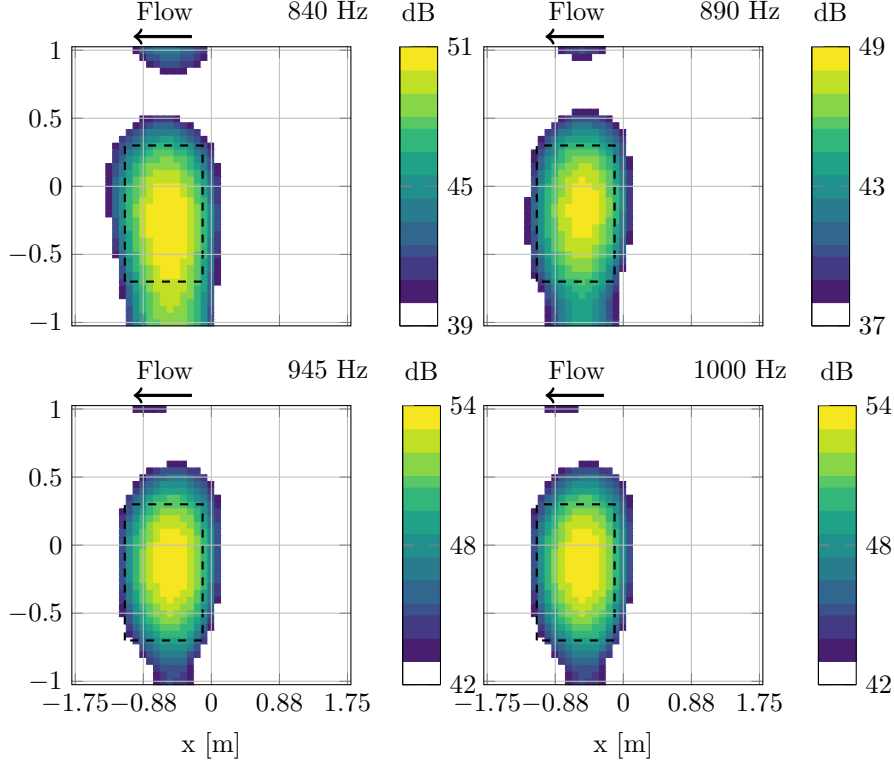


Figure 6: Beamforming maps at frequencies just below the expected lower frequency limit 1000 Hz. Reflections from floor and ceiling are increasing in size and gradually moving into the source integration region (shown in dashed).

structural resonances in the tensioned Kevlar fabric, in agreement with previous studies [2, 3, 25, 6, 26], where a fluctuating behavior of the Kevlar IL was found.

3.2 Turbulent boundary layer loss

The TBL loss was estimated from source integration of DAS beamforming maps, similar to the approach described above. In Fig. 7 beamforming maps at 2660 Hz are shown with source integration regions at five flow speeds. A comparison between the source maps with and without the correction from Sec. 2.1 is also shown. The source location is recovered precisely with the correction. Comparing the top right plot and middle and bottom plots, that is, without and with the correction, respectively, it is seen, that the amplitude correction gives a slight increase in the peak value. Thus, without the amplitude correction, the TBL loss would be overestimated by the following analysis. A signal-to-noise ratio higher than 6 dB was used to select measurement data for computing the TBL loss. This is shown in Fig. 8. Since, the lower frequency range is approximately 1000 Hz as discussed above, the TBL decrease below 1000 Hz is not reliable and doesn't capture the physical process truthfully. However, in the range 1000 Hz-4000 Hz, the TBL is fairly constant at each flow speed, this was also observed in [3]. A curve fit is found based on

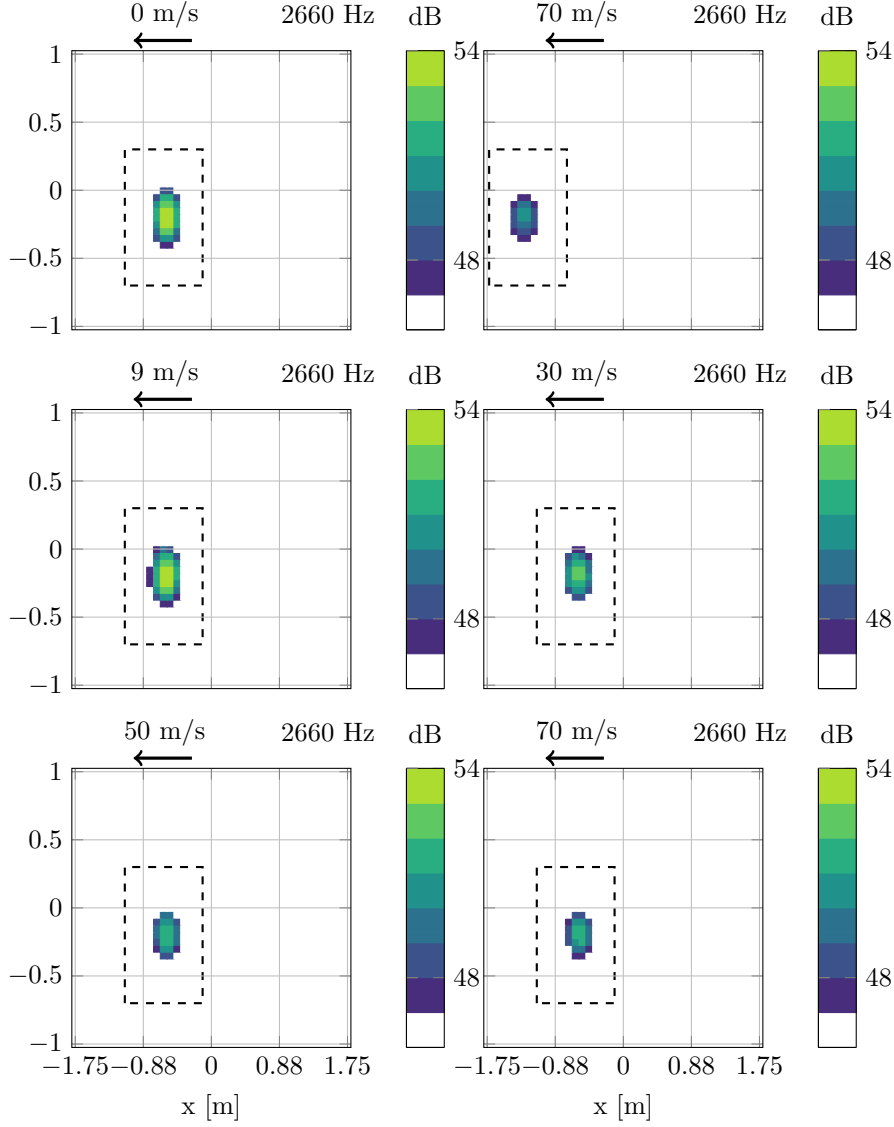


Figure 7: Beamforming maps at $f = 2660$ Hz. No flow case (top left), maximum flow speed (70 m/s) without correction (top right), and the remaining with correction at four flow speeds. Integration regions are shown in dashed and dynamic range is 8 dB.

the linear velocity scaling seen above 1000 Hz in Fig. 8. In order to make a smooth transition to data point below 1000 Hz, a quadratic function in frequency was applied. This is justified by the following assumption: as the wavelength of sound become larger than the boundary layer thickness, the attenuation of sound decreases. Measurements of the boundary layer thickness on the Kevlar wall was not available, but from measurements in a hard wall configuration, the boundary layer thickness is expected to be of the order of magnitude 0.1 m, corresponding to

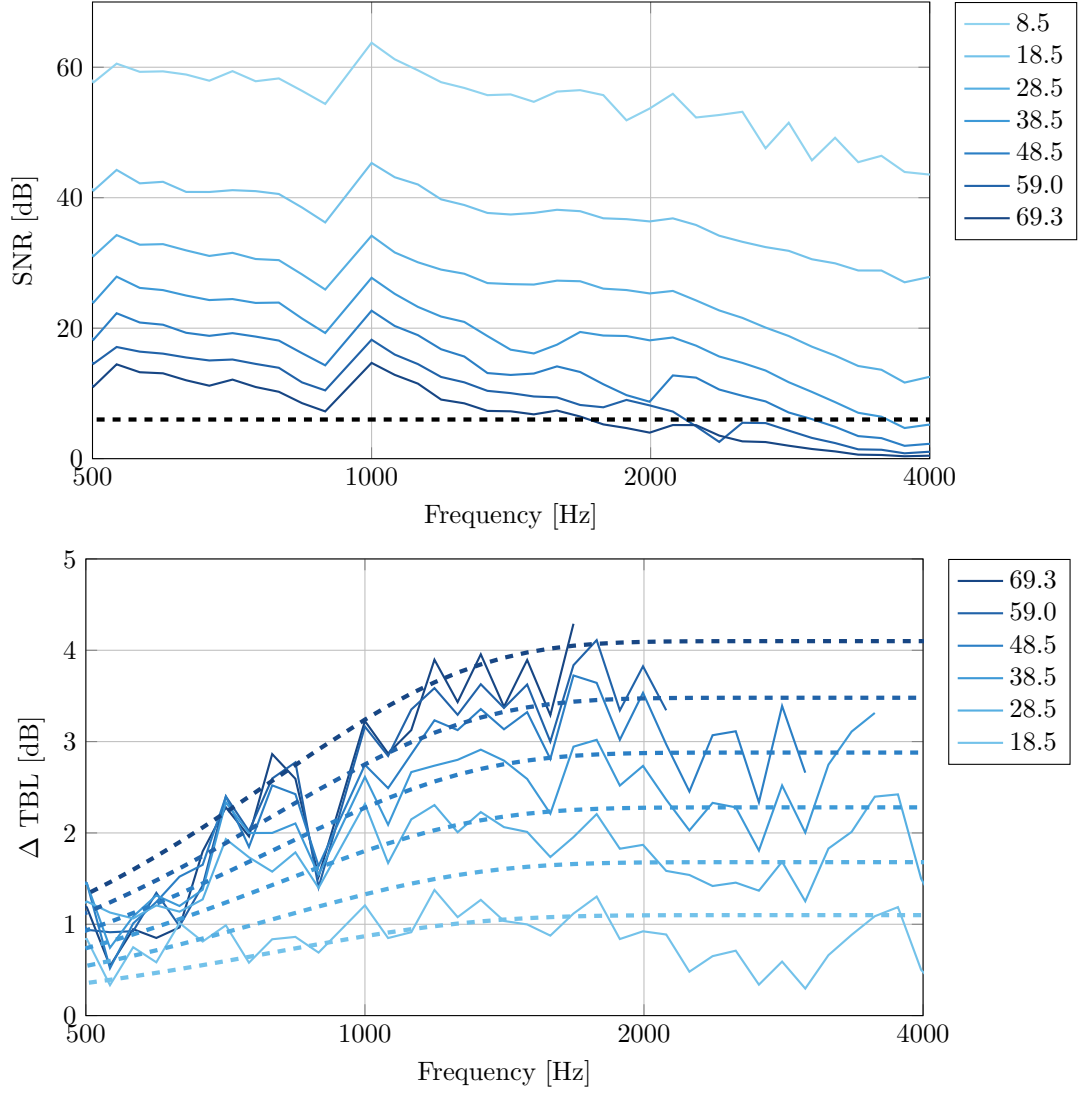


Figure 8: Top: Signal-to-noise ratios (SNR) of integrated spectra for all flow speeds, data above SNR 6 dB is shown in bottom plot as turbulent boundary layer (TBL) loss (ΔTBL), over two shear layers. Curve fit functions are shown in dashed.

a frequency of 3430 Hz. Thus, at 1000 Hz, the wavelength is expected to be three times longer than the boundary layer thickness. The curve fit function shown in Fig. 8 is

$$\alpha_1 \cdot \left(1 - e^{-(\beta \cdot f)^2}\right) \cdot Ma, \quad (21)$$

where $\beta = 0.00125$ and $\alpha_1 = 20$ for two boundary layers (shown in Fig. 8) and $\alpha_1 = 10$ for a single boundary layer, assuming that the boundary layer losses are identical on the two Kevlar walls. This model is slightly different from what was found in [3, 26]. In these references they

used a quadratic model,

$$\left(1 - e^{-(\beta \cdot f)}\right) \cdot (\alpha_1 \cdot Ma + \alpha_2 \cdot Ma^2), \quad (22)$$

with parameters $\alpha_1 = 5.4316$, $\alpha_2 = 88.95$, and $\beta = 0.001057$ [3]. In comparison, [26] used the same model and found $\alpha_1 = 14.51$, $\alpha_2 = -0.23$, and $\beta = 0.001057$. A comparison of models is given in Fig. 9 for two flow speeds. It should be mentioned, that the reported maximum flow speed in the study by Mayer et al. is $U_0 = 30$ m/s [26]. The differences between the present and previous studies are discussed in the following.

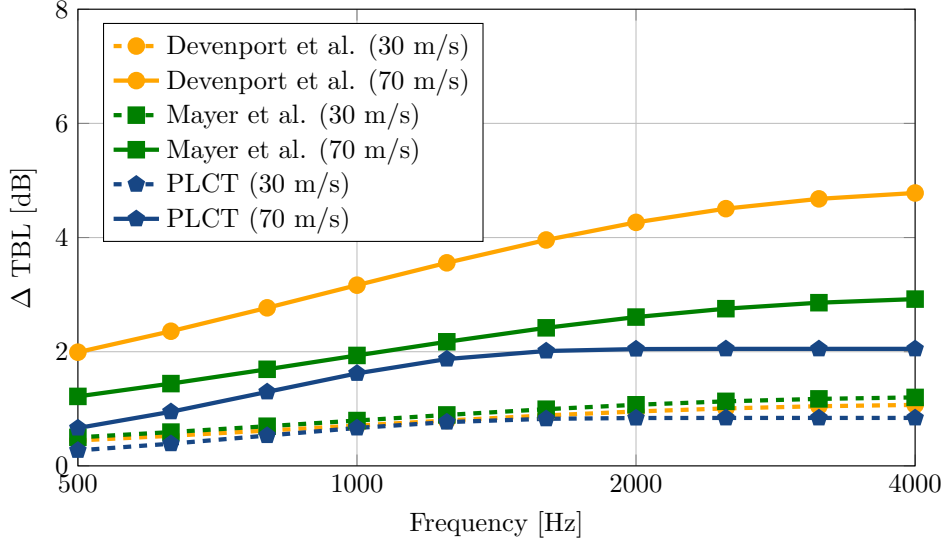


Figure 9: Comparison of TBL loss (Δ TBL) models of this study (PLCT) and two other facilities, computed at $U_0 = 30$ m/s and $U_0 = 70$ m/s.

4 Discussion

The proposed method is closely related to previous studies [3, 26]. For the Kevlar IL, they both used individual microphone spectra to obtain estimates of the insertion loss between a reference setup without Kevlar and setup with Kevlar. They observed an oscillatory behavior and found a curve fit that was quadratic in frequency. The Kevlar IL in their studies was less than 1 dB at 10 kHz, which is much lower than the Kevlar IL found in this study. Comparing to the alternative methodology, the acoustic pulse source that was used in [13, 6], Pascioni et al. found a Kevlar insertion loss as a smoothly increasing function of frequency, and about 1 dB at 6 kHz [13]. The results were also compared to an analytical model, finding good agreement. Bahr et al. found similar Kevlar losses compared to [13], about 1 dB below 10 kHz, but they did observe a fluctuation in frequency, similar to the above mentioned studies that used a regular loudspeaker [6]. The authors remark, that the fluctuating behavior could be related to structural vibrations of the Kevlar. With four studies and two different methodologies reporting a Kevlar IL below

1 dB up to at least 6 kHz, it is remarkable that this study finds a significantly higher Kevlar IL (based on the trend in the frequency range 1000 Hz-2000 Hz, shown in Fig. 5, the Kevlar IL would be about 4 dB at 5 kHz if extrapolating quadratically). The density of the Kevlar fabric is presumably a contributing factor to this difference. The three studies [3, 13, 6] were conducted in three different wind tunnels and used similar type of Kevlar fabric (Kevlar 49, type 120), tensioned at approximately 1500 N/m, with densities in the range 58 g/m² to 61 g/m². In this study, the density of the Kevlar fabric was 68 g/m². In addition, the open area ratio of the fabric is also believed to be a contributing factor, but since the OAR is not reported in the mentioned studies, a comparison is not possible.

The turbulent boundary layer noise was determined by subtracting a known reference, so these results are not affected by the issue described above. The frequency range of 1000 Hz to 4000 Hz was chosen to be a reliable range for determining the TBL loss. Despite the highest flow speed cases was gradually filtered away by lack of sufficient SNR, a constant TBL loss was observed as function of flow speed. This is in line with the results obtained in [3], with their results shown in the frequency range 3000 Hz to 7000 Hz. The TBL loss found in this study is somewhat lower and only a linear scaling in flow speed is observed, and not quadratic as it is the case in [3]. The correction for refraction over two shear layers, which was derived and used in this study, was seen to increase the amplitude compared to a situation without correction (Fig. 7). Similarly, it is expected to produce slightly higher levels compared to a correction accounting for only one shear layer, which was used in [3]. This is one aspect that could contribute to the discrepancy between TBL loss found in [3] and this study, and demonstrated by the model comparison in Fig. 9. With regards to the laser-pulse methodology, Pascioni et al. found a TBL loss of less than 1 dB at the highest flow speed (60 m/s) [13]. Similarly, at the same flow speed, Bahr et al. found a TBL loss to be less than 2 dB at frequencies below 10 kHz. Additionally, no velocity scaling was observed, but the authors remarks that this could be due to their methodology, since they took a free shear layer condition (measurement without Kevlar wall) as reference [6].

5 Conclusion

This study investigated Kevlar insertion loss and turbulent boundary layer loss in a hybrid anechoic wind tunnel. The estimation of losses was conducted using a loudspeaker with attached volume velocity tube to ensure a known reference level. Using a microphone array and beamforming technique, the level measured across two Kevlar walls was compared to the reference level. The Kevlar insertion loss could be estimated reliably in the frequency range 1000 Hz to 2500 Hz, and was found to be about 2 dB at 2000 Hz. This result was compared to studies at other wind tunnel facilities, finding good agreement in the frequency dependency but a slightly higher insertion loss, which could be attributed to a higher density of the fabric in the present study.

The turbulent boundary layer loss was estimated via source integration of beamforming maps, that had been corrected for flow convection and refraction over two shear layers, which was derived in this study. The turbulent boundary layer loss was seen to scale linearly with Mach number and a simple curve fit was found and compared to previous studies. x In conclu-

sion, this study proposed a non-intrusive method for estimating level losses in a Kevlar-walled wind tunnel. An analytical shear layer correction for two shear layers was derived. The Kevlar insertion loss and turbulent boundary layer loss was determined from beamforming maps using a volume velocity source as reference. The results were compared to previous studies and differences in methodology and Kevlar fabric were discussed. This study has contributed to the ongoing investigation of acoustic losses in the Kevlar-walled wind tunnel. Future work on the effects of structural vibrations, Kevlar tension and open-area ratio, still need to be addressed to better understand the physical processes observed in the experimental results.

References

- [1] C. S. Allen et al. *Aeroacoustic Measurements*. Ed. by T. J. Mueller. Berlin, Heidelberg: Springer Berlin Heidelberg, Jan. 2002. DOI: 10.1007/978-3-662-05058-3.
- [2] S. Jaeger, W. Horne, and C. Allen. "Effect of surface treatment on array microphone self-noise". In: *6th Aeroacoustics Conference and Exhibit*. Reston, Virginia: American Institute of Aeronautics and Astronautics, June 2000. DOI: 10.2514/6.2000-1937.
- [3] W. J. Devenport et al. "The Kevlar-walled anechoic wind tunnel". In: *Journal of Sound and Vibration* 332.17 (2013), pp. 3971–3991. DOI: 10.1016/j.jsv.2013.02.043.
- [4] T. Ito et al. "Aerodynamic/aeroacoustic testing in anechoic closed test sections of Low-speed wind tunnels". In: *16th AIAA/CEAS Aeroacoustics Conference (31st AIAA Aeroacoustics Conference)*. American Institute of Aeronautics and Astronautics Inc., Jan. 2010, pp. 2010–3750. DOI: 10.2514/6.2010-3750.
- [5] T. Geyer, E. Sarradj, and G. Herold. "Flow noise generation of cylinders with soft porous cover". In: *21st AIAA/CEAS Aeroacoustics Conference* June (2015), pp. 1–17. DOI: 10.2514/6.2015-3147.
- [6] C. J. Bahr, F. V. Hutcheson, and D. J. Stead. "Assessment of unsteady propagation characteristics and corrections in aeroacoustic wind tunnels using an acoustic pulse". In: *2018 AIAA/CEAS Aeroacoustics Conference*. Reston, Virginia: American Institute of Aeronautics and Astronautics, June 2018, pp. 1–22. DOI: 10.2514/6.2018-3118.
- [7] K. A. Pascioni and L. N. Cattafesta. "An aeroacoustic study of a leading-edge slat: Beam-forming and far field estimation using near field quantities". In: *Journal of Sound and Vibration* 429 (2018), pp. 224–244. DOI: 10.1016/j.jsv.2018.05.029.
- [8] L. Li et al. "Aeroacoustic measurement of 30P30N high-lift configuration in the test section with Kevlar cloth and perforated plate". In: *Aerospace Science and Technology* 70 (2017), pp. 590–599. DOI: 10.1016/j.ast.2017.08.039.
- [9] Y. Mayer, B. Zang, and M. Azarpeyvand. "Design of a Kevlar-Walled Test Section with Dynamic Turntable and Aeroacoustic Investigation of an Oscillating Airfoil". In: *25th AIAA/CEAS Aeroacoustics Conference*. May. Reston, Virginia: American Institute of Aeronautics and Astronautics, May 2019. DOI: 10.2514/6.2019-2464.
- [10] F. Boden and J. Delfs. "Development of a LASER-based sound source". In: *Institute of Noise Control Engineering of the USA - 35th International Congress and Exposition on Noise Control Engineering, INTER-NOISE 2006*. Vol. 7. Institute of Noise Control Engineering of the USA, 2006, pp. 4944–4953.
- [11] C. J. Bahr et al. "A plasma-based non-intrusive point source for acoustic beamforming applications". In: *Journal of Sound and Vibration* 344 (2015), pp. 59–80. DOI: 10.1016/j.jsv.2015.01.023.
- [12] K.-S. Rossignol, J. Delfs, and F. Boden. "On the Relevance of Convection Effects for a Laser-Generated Sound Source". eng. In: *21st AIAA/CEAS Aeroacoustics Conference*. Reston, Virginia: American Institute of Aeronautics and Astronautics, June 2015. DOI: 10.2514/6.2015-3146.

- [13] K. Pascioni, A. Colangelo, and L. Cattafesta. "Acoustic corrections for a kevlar wall wind tunnel using a pulsed-laser point source". In: *24th International Congress on Sound and Vibration, ICSV 2017* (2017), pp. 1–8.
- [14] M. Szoke et al. "Characterization of Hybrid Wind Tunnel Environments Using Laser-Induced Acoustic Sources". In: *AIAA Scitech 2020 Forum*. January. Reston, Virginia: American Institute of Aeronautics and Astronautics, Jan. 2020, pp. 1–14. DOI: 10.2514/6.2020-1253.
- [15] N. Moller, J. Hald, and S. Gade. "The use of volume velocity source in transfer measurements". In: *SAE Technical Papers V* (2004), pp. 1–8. DOI: 10.4271/2004-01-3232.
- [16] Y. Luan and F. Jacobsen. "A method of measuring the Green's function in an enclosure". In: *The Journal of the Acoustical Society of America* 123.6 (2008), pp. 4044–4046. DOI: 10.1121/1.2917804.
- [17] D. H. D. H. Johnson and D. E. Dudgeon. *Array signal processing: concepts and techniques*. PTR Prentice Hall, 1993, pp. 1–533.
- [18] P. Sijtsma. *Phased Array Beamforming Applied to Wind Tunnel and Fly-Over Tests*. Tech. rep. December. Amsterdam, The Netherlands: National Aerospace Laboratory (NLR), 2010.
- [19] R. K. Amiet. "Refraction of sound by a shear layer". In: *Journal of Sound Vibration* 58.4 (Jan. 1978), pp. 467–482.
- [20] H. S. Ribner. "Reflection, Transmission, and Amplification of Sound by a Moving Medium". In: *The Journal of the Acoustical Society of America* 29.4 (Apr. 1957), pp. 435–441. DOI: 10.1121/1.1908918.
- [21] S. Glegg and W. Devenport. *Aeroacoustics of low mach number flows: Fundamentals, analysis, and measurement*. Academic Press, 2017, pp. 1–537.
- [22] P. D. Welch. "The Use of Fast Fourier Transform for the Estimation of Power Spectra: A Method Based on Time Averaging Over Short, Modified Periodograms". In: *IEEE Transactions on Audio and Electroacoustics* 15.2 (Jan. 1967), pp. 70–73. DOI: 10.1109/TAU.1967.1161901.
- [23] L. Rayleigh. "Investigations in optics, with special reference to the spectroscope". In: *The London, Edinburgh, and Dublin Philosophical Magazine and Journal of Science* 8.51 (1879), pp. 477–486. DOI: 10.1080/14786447908639715.
- [24] J. Hald and J. J. Christensen. *Technical Review: Beamforming*. Brüel & Kjær, Apr. 2004.
- [25] L. Li et al. "Aeroacoustic measurement of 30P30N high-lift configuration in the test section with Kevlar cloth and perforated plate". In: *Aerospace Science and Technology* 70 (Nov. 2017), pp. 590–599.
- [26] Y. Mayer, B. Zang, and M. Azarpeyvand. "Design of a Kevlar-Walled Test Section with Dynamic Turntable and Aeroacoustic Investigation of an Oscillating Airfoil". In: *25th AIAA/CEAS Aeroacoustics Conference*. May. Reston, Virginia: American Institute of Aeronautics and Astronautics, May 2019. DOI: 10.2514/6.2019-2464.

Bibliography

- [1] C. V. Hernández, T. Telsnig, and A. V. Pradas. *JRC Wind Energy Status Report: 2016 Edition*. Tech. rep. European Commission, 2017. DOI: 10.2760/85725.
- [2] T. F. Brooks, D. Pope, and M. A. Marcolini. "Airfoil self-noise and prediction". In: *Nasa Reference Publication* 1218 (1989).
- [3] L. L. Beranek, S. Labate, and U. Ingard. "Noise Control for NACA Supersonic Wind Tunnel". In: *Journal of the Acoustical Society of America* 27.1 (Jan. 1955), pp. 85–98.
- [4] G. F. McCanless and J. R. Boone. "Noise reduction in transonic wind tunnels". In: *Journal of the Acoustical Society of America* 56.5 (Nov. 1974), pp. 1501–1510. DOI: 10.1121/1.1903471.
- [5] L. A. Schutzenhofer and P. W. Howard. "Suppression of background noise in a transonic wind-tunnel test section". eng. In: *AIAA Journal* 13.11 (Nov. 1975), pp. 1467–1471. DOI: 10.2514/3.7016.
- [6] F. R. Grosche, H. Stiewitt, and B. Binder. "Acoustic Wind-Tunnel Measurements with a Highly Directional Microphone". In: *AIAA Journal* 15.11 (Nov. 1977), pp. 1590–1596. DOI: 10.2514/3.60826.
- [7] R. K. Amiet. "Noise due to turbulent flow past a trailing edge". In: *Journal of Sound and Vibration* 47.3 (Jan. 1976), pp. 387–393. DOI: 10.1016/0022-460X(76)90948-2.
- [8] R. K. Amiet. "Refraction of sound by a shear layer". In: *Journal of Sound and Vibration* 58.4 (1978), pp. 467–482. DOI: 10.1016/0022-460X(78)90353-X.
- [9] M. Howe. "A review of the theory of trailing edge noise". In: *Journal of Sound and Vibration* 61.3 (Dec. 1978), pp. 437–465. DOI: 10.1016/0022-460X(78)90391-7.
- [10] P. Soderman and L. Hoglund. "Wind-tunnel fan noise reduction including effects of turning vanes on noise propagation". In: American Institute of Aeronautics and Astronautics (AIAA), Mar. 1979. DOI: 10.2514/6.1979-642.

- [11] H. H. Brouwer. "Anechoic Wind Tunnels". In: *The VKI Lecture Series "Aeroacoustics and Active Noise Control"*, 15-18 September 1997. Oct. 1997.
- [12] E. Duell et al. "Recent advances in large-scale aeroacoustic wind tunnels". In: *8th Aiaa/ceas Aeroacoustics Conference and Exhibit*. Jan. 2002.
- [13] E. G. Duell et al. "Progress in Aeroacoustic and Climatic Wind Tunnels for Automotive Wind Noise and Acoustic Testing". In: *SAE International Journal of Passenger Cars - Mechanical Systems* 6.1 (Apr. 2013), pp. 2013–01. DOI: 10.4271/2013-01-1352.
- [14] J. Mathew. "Design, Fabrication, and Characterization of an Anechoic Wind Tunnel Facility". PhD thesis. University of Florida, 2006.
- [15] J. P. Gomes, A. Bergmann, and H. Holthusen. "Aeroacoustic wind tunnel design". In: *CEAS Aeronautical Journal* 10.1 (Mar. 2019), pp. 231–249. DOI: 10.1007/s13272-019-00372-7.
- [16] W. Devenport et al. "Design and Operation of Hybrid Aeroacoustic Wind Tunnels". In: *Design and Operation of Aeroacoustic Wind Tunnel Tests for Group and Air Transport*. Jan. 2017. DOI: 10.14339/STO-EN-AVT-287.
- [17] S. Glegg and W. Devenport. *Aeroacoustics of low mach number flows: Fundamentals, analysis, and measurement*. Academic Press, 2017, pp. 1–537.
- [18] O. M. Phillips. "The intensity of Aeolian tones". In: *Journal of Fluid Mechanics* 1.06 (Dec. 1956), pp. 607–624. DOI: 10.1017/S0022112056000408.
- [19] H. Fujita et al. "The aeolian tone characteristics of a circular cylinder in high reynolds number flow". In: *5th AIAA/CEAS Aeroacoustics Conference and Exhibit*. American Institute of Aeronautics and Astronautics Inc, AIAA, 1999, pp. 305–310. DOI: 10.2514/6.1999-1849.
- [20] R. Merino-Martínez et al. "Aeroacoustic design and characterization of the 3D-printed, open-jet, anechoic wind tunnel of Delft University of Technology". In: *Applied Acoustics* 170 (2020). DOI: 10.1016/j.apacoust.2020.107504.
- [21] E. Sarradj et al. "Acoustic and aerodynamic design and characterization of a small-scale aeroacoustic wind tunnel". In: *Applied Acoustics* 70.8 (Aug. 2009), pp. 1073–1080. DOI: 10.1016/j.apacoust.2009.02.009.
- [22] U. Michel. "History of acoustic beamforming". In: *Proceedings of the Berlin Beamforming Conference*. Nov. 2006, pp. 1–17.
- [23] P. Chiariotti, M. Martarelli, and P. Castellini. "Acoustic beamforming for noise source localization – Reviews, methodology and applications". In: *Mechanical Systems and Signal Processing* 120 (Apr. 2019), pp. 422–448. DOI: 10.1016/j.ymssp.2018.09.019.

- [24] R. Merino-Martínez et al. "A review of acoustic imaging methods using phased microphone arrays: Part of the "Aircraft Noise Generation and Assessment" Special Issue". In: *CEAS Aeronautical Journal* 10.1 (Jan. 2019), pp. 197–230. DOI: 10.1007/s13272-019-00383-4.
- [25] D. H. Johnson and D. E. Dudgeon. *Array signal processing: concepts and techniques*. Englewood Cliffs: PTR Prentice Hall, 1993, p. 533.
- [26] H. L. Van Trees. *Optimum Array Processing*. Vol. 4. New York, USA: John Wiley & Sons, Inc., Mar. 2002, pp. 1–471. DOI: 10.1002/0471221104.
- [27] F. Jacobsen and P. M. Juhl. *Fundamentals of General Linear Acoustics*. Wiley, 2013, pp. 1–300.
- [28] J. Hald and J. J. Christensen. *Technical Review: Beamforming*. Brüel & Kjær, Apr. 2004.
- [29] E. Sarradj. "Three-dimensional acoustic source mapping with different beamforming steering vector formulations". In: *Advances in Acoustics and Vibration* 2012.4 (Jan. 2012), pp. 1–12. DOI: 10.1155/2012/292695.
- [30] L. Rayleigh. "Investigations in optics, with special reference to the spectroscopy". In: *The London, Edinburgh, and Dublin Philosophical Magazine and Journal of Science* 8.51 (1879), pp. 477–486. DOI: 10.1080/14786447908639715.
- [31] P. Sijtsma. *Phased Array Beamforming Applied to Wind Tunnel And Fly-Over Tests*. Tech. rep. NLR-TP-2010-549, National Aerospace Laboratory (NLR), Oct. 2010. DOI: 10.4271/2010-36-0514.
- [32] M. Mosher. "Phased arrays for aeroacoustic testing: Theoretical development". In: *2nd AIAA/CEAS Aeroacoustics Conference*. American Institute of Aeronautics and Astronautics Inc, AIAA, 1996. DOI: 10.2514/6.1996-1713.
- [33] T. Brooks and W. Humphreys Jr. "Effect of directional array size on the measurement of airframe noise components". In: *5th AIAA/CEAS Aeroacoustics Conference and Exhibit*. 99. Reston, Virginia: American Institute of Aeronautics and Astronautics, May 1999. DOI: 10.2514/6.1999-1958.
- [34] C. S. Allen et al. *Aeroacoustic Measurements*. Ed. by T. J. Mueller. Springer Science & Business Media, Jan. 2002. DOI: 10.1007/978-3-662-05058-3.
- [35] J. Hald. "Removal of incoherent noise from an averaged cross-spectral matrix". In: *The Journal of the Acoustical Society of America* 142.2 (Aug. 2017), pp. 846–854. DOI: 10.1121/1.4997923.
- [36] A. Dinselmeyer et al. "A probabilistic approach for cross-spectral matrix denoising: Benchmarking with some recent methods". In: *The Journal of the Acoustical Society of America* 147.5 (May 2020), pp. 3108–3123. DOI: 10.1121/10.0001098.

- [37] C. J. Bahr and W. C. Horne. "Subspace-based background subtraction applied to aeroacoustic wind tunnel testing". In: *International Journal of Aeroacoustics* 16.4-5 (2017), pp. 299–325. DOI: 10.1177/1475472X17718885.
- [38] J. Hadamard. *Lectures on Cauchy's Problem in Linear Partial Differential Equations*. Yale University Press, New Haven, 1923.
- [39] Q. Leclère et al. "A unified formalism for acoustic imaging based on microphone array measurements". In: *International Journal of Aeroacoustics* 16.4-5 (July 2017), pp. 431–456. DOI: 10.1177/1475472X17718883.
- [40] P. T. Soderman and S. C. Noble. "Directional microphone array for acoustic studies of wind tunnel models". In: *Journal of Aircraft* 12.3 (1975), pp. 168–173. DOI: 10.2514/3.59813.
- [41] J. Billingsley and R. Kinns. "The acoustic telescope". In: *Journal of Sound and Vibration* 48.4 (1976), pp. 485–510. DOI: 10.1016/0022-460X(76)90552-6.
- [42] T. F. Brooks, M. A. Marcolini, and D. S. Pope. "A directional array approach for the measurement of rotor noise source distributions with controlled spatial resolution". In: *Journal of Sound and Vibration* 112.1 (1987), pp. 192–197. DOI: 10.1016/S0022-460X(87)80105-0.
- [43] J. R. Underbrink and R. P. Dougherty. "Array design for non-intrusive measurement of noise sources". In: *Proceedings - National Conference on Noise Control Engineering*. Vol. 2. Inst of Noise Control Engineering, 1996, pp. 757–762.
- [44] R. A. Gramann and J. W. Mocio. "Aeroacoustic measurements in wind tunnels using adaptive beamforming methods". In: *The Journal of the Acoustical Society of America* 97.6 (June 1995), pp. 3694–3701. DOI: 10.1121/1.412386.
- [45] R. Dougherty and R. Stoker. "Sidelobe suppression for phased array aeroacoustic measurements". In: *4th AIAA/CEAS Aeroacoustics Conference*. Vol. 2242. Reston, Virginia: American Institute of Aeronautics and Astronautics, June 1998, pp. 235–245. DOI: 10.2514/6.1998-2242.
- [46] J. A. Hogbom. "Aperture synthesis with a non-regular distribution of interferometer baselines". In: *Astronomy and Astrophysics Supplement Series* 15.3 (Jan. 1974), pp. 417–426.
- [47] P. Sijtsma. "CLEAN based on spatial source coherence". In: *International journal of aeroacoustics* 6.4 (2007), pp. 357–374.
- [48] G. H. Golub and C. F. Van Loan. *Matrix Computations*. 4th Editio. The Johns Hopkins University Press, Jan. 2016, pp. 1–756.

- [49] T. F. Brooks and W. M. Humphreys. "A deconvolution approach for the mapping of acoustic sources (DAMAS) determined from phased microphone arrays". In: *Journal of Sound and Vibration* 294.4 (July 2006), pp. 856–879. DOI: 10.1016/j.jsv.2005.12.046.
- [50] T. F. Brooks and W. M. Humphreys. "Extension of DAMAS phased array processing for spatial coherence determination (DAMAS-C)". In: *12th AIAA/CEAS Aeroacoustics Conference (27th AIAA Aeroacoustics Conference)*. Vol. 5. May 2006, pp. 3337–3354. DOI: 10.2514/6.2006-2654.
- [51] R. P. Dougherty. "Extensions of DAMAS and benefits and limitations of deconvolution in beamforming". In: *11th AIAA/CEAS Aeroacoustics Conference*. Vol. 3. June 2005, pp. 2036–2048. DOI: 10.2514/6.2005-2961.
- [52] K. Ehrenfried and L. Koop. "Comparison of iterative deconvolution algorithms for the mapping of acoustic sources". In: *AIAA Journal* 45.7 (Jan. 2007), pp. 1584–1595. DOI: 10.2514/1.26320.
- [53] C. S. Lawson and R. J. Hanson. *Solving least squares problems*. Prentice-Hall, 1974.
- [54] O. Lylloff et al. "Improving the efficiency of deconvolution algorithms for sound source localization". In: *The Journal of the Acoustical Society of America* 138.1 (2015), pp. 172–180. DOI: 10.1121/1.4922516.
- [55] T. Yardibi et al. "A covariance fitting approach for correlated acoustic source mapping". In: *The Journal of the Acoustical Society of America* 127.5 (Jan. 2010), pp. 2920–2931. DOI: 10.1121/1.3365260.
- [56] D. Blacodon and G. Elias. "Level Estimation of Extended Acoustic Sources Using a Parametric Method". eng. In: *Journal of Aircraft* 41.6 (Nov. 2004), pp. 1360–1369. DOI: 10.2514/1.3053.
- [57] C. J. Bahr et al. "A comparison of microphone phased array methods applied to the study of airframe noise in wind tunnel testing". In: *23rd AIAA/CEAS Aeroacoustics Conference, 2017*. Reston, Virginia: American Institute of Aeronautics and Astronautics, June 2017, pp. 1–19. DOI: 10.2514/6.2017-3718.
- [58] E. Sarradj et al. "A microphone array method benchmarking exercise using synthesized input data". In: *23rd AIAA/CEAS Aeroacoustics Conference, 2017*. Reston, Virginia: American Institute of Aeronautics and Astronautics, June 2017. DOI: 10.2514/6.2017-3719.
- [59] T. Yardibi et al. "Comparison of Microphone Array Processing Techniques for Aeroacoustic Measurements". In: *International Journal of Aeroacoustics* 9.6 (Jan. 2010), pp. 733–761. DOI: 10.1260/1475-472x.9.6.733.
- [60] G. Herold and E. Sarradj. "Performance analysis of microphone array methods". In: *Journal of Sound and Vibration* 401 (Aug. 2017), pp. 152–168. DOI: 10.1016/j.jsv.2017.04.030.

- [61] S. Kröber. "Comparability of Microphone Array Measurements in Open and Closed Wind Tunnels". PhD thesis. Technical University of Berlin, 2013.
- [62] S. Oerlemans. "Detection of aeroacoustic sound sources on aircraft and wind turbines". PhD thesis. Thesis University of Twente, Enschede, 2009, pp. 1–173.
- [63] L. Koop and K. Ehrenfried. "Microphone-array processing for wind-tunnel measurements with strong background noise". In: *14th AIAA/CEAS Aeroacoustics Conference (29th AIAA Aeroacoustics Conference)* (Jan. 2008), pp. 2008–2907. DOI: 10.2514/6.2008-2907.
- [64] S. Jaeger, W. Horne, and C. Allen. "Effect of surface treatment on array microphone self-noise". In: *6th Aeroacoustics Conference and Exhibit*. Reston, Virigina: American Institute of Aeronautics and Astronautics, June 2000. DOI: 10.2514/6.2000-1937.
- [65] R. P. Dougherty. "Turbulent Decorrelation of aeroacoustic phased arrays: Lessons from atmospheric science and astronomy". In: *9th AIAA/CEAS Aeroacoustics Conference and Exhibit* (Jan. 2003). DOI: 10.2514/6.2003-3200.
- [66] L. Koop, K. Ehrenfried, and S. Kroeber. "Investigation of the Systematic Phase Mismatch in Microphone-Array Analysis". In: *11th AIAA/CEAS Aeroacoustics Conference*. Vol. 3. Reston, Virigina: American Institute of Aeronautics and Astronautics, May 2005, pp. 2049–2066. DOI: 10.2514/6.2005-2962.
- [67] D. Ernst, C. Spehr, and T. Berkefeld. "Decorrelation of acoustic wave propagation through the shear layer in open jet wind tunnel". In: *21st AIAA/CEAS Aeroacoustics Conference* (2015). DOI: 10.2514/6.2015-2976.
- [68] L. S. Pires, R. P. Dougherty, and S. N. Gerges. "Predicting Turbulent Decorrelation in Acoustic Phased Array in a Turbulent Medium". In: *50th AIAA Aerospace Sciences Meeting including the New Horizons Forum and Aerospace Exposition*. Vol. 2015-April. 3. Reston, Virigina: American Institute of Aeronautics and Astronautics, June 2015, pp. 15–77. DOI: 10.4271/2014-36-0765.
- [69] B. S. Smith et al. "Development and testing of a novel acoustic wind tunnel concept". In: *11th AIAA/CEAS Aeroacoustics Conference*. Vol. 5. 2005, pp. 3153–3173. DOI: 10.2514/6.2005-3053.
- [70] W. J. Devenport et al. "The Kevlar-walled anechoic wind tunnel". In: *Journal of Sound and Vibration* 332.17 (2013), pp. 3971–3991. DOI: 10.1016/j.jsv.2013.02.043.

- [71] T. Ito et al. "Aerodynamic/aeroacoustic testing in anechoic closed test sections of Low-speed wind tunnels". In: *16th AIAA/CEAS Aeroacoustics Conference (31st AIAA Aeroacoustics Conference)*. American Institute of Aeronautics and Astronautics Inc., Jan. 2010, pp. 2010–3750. doi: 10.2514/6.2010-3750.
- [72] K. A. Pascioni and L. N. Cattafesta. "An aeroacoustic study of a leading-edge slat: Beamforming and far field estimation using near field quantities". In: *Journal of Sound and Vibration* 429 (2018), pp. 224–244. doi: 10.1016/j.jsv.2018.05.029.
- [73] L. Li et al. "Aeroacoustic measurement of 30P30N high-lift configuration in the test section with Kevlar cloth and perforated plate". In: *Aerospace Science and Technology* 70 (Nov. 2017), pp. 590–599.
- [74] C. J. Bahr, F. V. Hutcheson, and D. J. Stead. "Assessment of unsteady propagation characteristics and corrections in aeroacoustic wind tunnels using an acoustic pulse". In: *2018 AIAA/CEAS Aeroacoustics Conference*. Reston, Virginia: American Institute of Aeronautics and Astronautics, June 2018, pp. 1–22. doi: 10.2514/6.2018-3118.
- [75] Y. D. Mayer, B. Zang, and M. Azarpeyvand. "Design of a kevlar-walled test section with dynamic turntable and aeroacoustic investigation of an oscillating airfoil". In: *25th AIAA/CEAS Aeroacoustics Conference, 2019 May* (2019). doi: 10.2514/6.2019-2464.
- [76] T. Geyer, E. Sarradj, and G. Herold. "Flow noise generation of cylinders with soft porous cover". In: *21st AIAA/CEAS Aeroacoustics Conference* June (2015), pp. 1–17. doi: 10.2514/6.2015-3147.
- [77] K. A. Brown. "Understanding and exploiting wind tunnels with porous flexible walls for aerodynamic measurement". PhD thesis. Virginia Tech, 2016.
- [78] M. C. Remillieux et al. "Calibration and demonstration of the new Virginia Tech anechoic wind tunnel". In: *14th AIAA/CEAS Aeroacoustics Conference (29th AIAA Aeroacoustics Conference)* February 2014 (2008). doi: 10.2514/6.2008-2911.
- [79] F. Boden and J. Delfs. *Development of a LASER-based sound source*. eng. 2006.
- [80] C. Bahr et al. "Shear layer time-delay correction using a non-intrusive acoustic point source". In: *International Journal of Aeroacoustics* 10.5-6 (Jan. 2011), pp. 497–530. doi: 10.1260/1475-472X.10.5-6.497.
- [81] K. S. Rossignol, J. Delfs, and F. Boden. *On the relevance of convection effects for a laser-generated sound source*. 2015. doi: 10.2514/6.2015-3146.
- [82] K. Pascioni, A. Colangelo, and L. Cattafesta. "Acoustic corrections for a kevlar wall wind tunnel using a pulsed-laser point source". In: *24th International Congress on Sound and Vibration, ICSV 2017* (2017), pp. 1–8.

- [83] M. Szóke et al. "Characterization of hybrid wind tunnel environments using laser-induced acoustic sources". In: *AIAA Scitech 2020 Forum*. Reston, Virginia: American Institute of Aeronautics and Astronautics, Jan. 2020, pp. 1–14. DOI: 10.2514/6.2020-1253.
- [84] *Acoustics – Determination of sound power levels and sound energy levels of noise sources using sound pressure – Precision methods for anechoic rooms and hemi-anechoic rooms*. Tech. rep. Geneva, CH: International Organization for Standardization, 2012.
- [85] H. Kuttruff. *Room Acoustics, Fifth Edition*. CRC Press, Apr. 2014, pp. 1–374. DOI: 10.1201/9781482266450.
- [86] O. Lylloff. *AeroAcoustics.jl, a Julia package for Aeroacoustic measurements*. 2020.
- [87] J. Bezanson et al. "Julia: A fresh approach to numerical computing". In: *SIAM Review* 59.1 (2017), pp. 65–98. DOI: 10.1137/141000671.
- [88] E. Sarradj and G. Herold. "A Python framework for microphone array data processing". In: *Applied Acoustics* 116 (Jan. 2017), pp. 50–58. DOI: 10.1016/j.apacoust.2016.09.015.
- [89] P. D. Welch. "The Use of Fast Fourier Transform for the Estimation of Power Spectra: A Method Based on Time Averaging Over Short, Modified Periodograms". In: *IEEE Transactions on Audio and Electroacoustics* 15.2 (Jan. 1967), pp. 70–73. DOI: 10.1109/TAU.1967.1161901.
- [90] A. Fischer, F. Bertagnolio, and H. A. Madsen. "Improvement of TNO type trailing edge noise models". In: *European Journal of Mechanics, B/Fluids* 61 (Jan. 2017), pp. 255–262. DOI: 10.1016/j.euromechflu.2016.09.005.
- [91] R. Parchen. *Progress report DRAW: a prediction scheme for trailing edge noise based on detail boundary layer characteristics*. Tech. rep. The Netherlands: TNO Rept. HAG-RPT-980023, TNO Institute of Applied Physics, 1998.
- [92] N. N. Sørensen. "General Purpose Flow Solver Applied to Flow over Hills". PhD thesis. Risø National Laboratory, Roskilde, Denmark, 1995, pp. 1–158.
- [93] T. von Karman. "Progress in the Statistical Theory of Turbulence". In: *Proceedings of the National Academy of Sciences* 34.11 (Nov. 1948), pp. 530–539. DOI: 10.1073/pnas.34.11.530.
- [94] R. H. Kraichnan. "Pressure Fluctuations in Turbulent Flow over a Flat Plate". In: *The Journal of the Acoustical Society of America* 28.3 (May 1956), pp. 378–390. DOI: 10.1121/1.1908336.